DOI: 10.1002/ ((please add manuscript number))
Article type: Review

Advanced Electrocatalysis for Energy and Environmental Sustainability via Water and Nitrogen Reactions

Yi Li[+], Huanhuan Wang[+], Cameron Priest, Siwei Li, Ping Xu, and Gang Wu**

Y. Li, H. Wang, C. Priest, Prof. G. Wu
Department of Chemical and Biological Engineering, University at Buffalo, The State University of New York, Buffalo, NY 14260, USA
E-mail: gangwu@buffalo.edu

S. Li, Prof. P. Xu
Department MIIT Key Laboratory of Critical Materials Technology for New Energy Conversion and Storage, School of Chemistry and Chemical Engineering, Harbin Institute of Technology, Harbin, Heilongjiang 150001, China
E-mail: pxu@hit.edu.cn

[+] These authors contributed equally to this work.

Keywords: electrocatalysis, energy conversion, clean energy, water reactions, nitrogen reactions

With the development of renewable energy technologies, clean and efficient energy storage and conversion via sustainable water and nitrogen reactions have attracted substantial attention to eventually address the current energy and environmental issues caused by the overwhelming use of fossil fuels. These electrochemical reactions are crucial for desirable clean energy technologies, including advanced water electrolyzers, hydrogen fuel cells, and ammonia electrosynthesis and utilization. However, their sluggish reaction kinetics often leads to inefficient energy conversion and catalyst instability. Innovative electrocatalysis, *i.e.*, catalysis at the interface between the electrode and electrolyte to facilitate charge transfer and mass transport, plays a vital role in boosting energy conversion efficiency and providing sufficient performance and durability for

these energy technologies. Herein, we provide a comprehensive review cohesively on recent progress, achievements, and remaining challenges for these critical electrocatalysis processes related to water (*i.e.*, oxygen evolution reaction-OER, and oxygen reduction reaction-ORR) and nitrogen (*i.e.*, nitrogen reduction reaction-NRR for ammonia synthesis and ammonia oxidation reaction-AOR for energy utilization). We discuss these electrocatalysis processes together with critical catalysts, electrolytes, and interfaces between the two within 3D porous electrodes. One primary emphasis is to highlight the performance of these energy technologies at the device level for OER-related proton exchange membrane (PEM) electrolyzers, ORR-related PEM fuel cells, NRR-driven ammonia electrosynthesis from water and nitrogen, and AOR-related direct ammonia fuel cells.

1. Introduction

Today, the dominant use of fossil fuels is increasing global concerns on climate change and energy sustainability. Intensive scientific research concentrates on clean energy technologies, including water electrolyzers,[1] fuel cells,[2-3] ammonia (NH_3) electrosynthesis, and carbon-free fuel technologies.[4-5] As illuminated in Figure 1, these clean energy technologies mostly rely on electrochemical reactions associated with earth-abundant H_2O, O_2, and N_2, creating sustainable and environmentally friendly water and nitrogen energy cycles. However, these critical reactions, including the oxygen evolution reaction (OER),[6-9] oxygen reduction reaction (ORR),[10-14] nitrogen reduction reaction (NRR),[15-17] and ammonia oxidation reaction (AOR),[18-20] are often kinetically sluggish and operated in oxidative/reductive potential windows, which cause

significant overpotential and catalyst stability issues. Therefore, electrochemically active and stable catalysts lie at the heart of these energy technologies [21-22], playing a primary role in utilizing renewable energy and more effectively implementing electricity in future transportation.

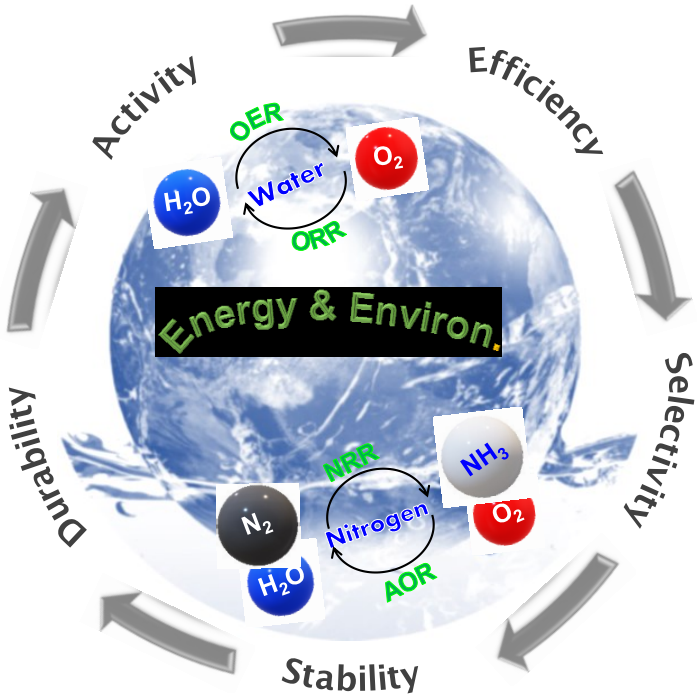

Figure 1. Sustainable energy and environment based on clean and earth-abundant H_2O, O_2, and N_2 for a variety of clean energy technologies.

Producing electricity from renewable sources such as solar, wind, and water has become economically competitive, thanks to years of cost reduction and advances in critical technologies. Using renewable electricity to power the water and NH_3 electrosynthesis electrolyzers can produce the carbon-neutral fuels of hydrogen and ammonia. In turn, they can utilize in proton-exchange membrane fuel cells (PEMFCs) and direct ammonia fuel cells (DAFCs) for electricity regeneration

for a variety of applications. Research and development of electrocatalysts for these water and nitrogen reactions have made significant progress in improving energy efficiency, activity, selectivity, and stability. The advancement of electrochemical technologies for clean energy conversion via sustainable water and nitrogen cycles also represents one avenue towards long-term (*e.g.*, seasonal) storage and the utilization of renewable energy.

Electrocatalysis, a process of increasing the rate of electrochemical reactions by using catalysts to lower activation energies via the modulating binding energies of reactants, intermediates, and products with active sites, plays a vital role in improving the performance of electrochemical energy devices.[23] In addition to being electrically conductive, similar to traditional heterogeneous catalysts, the ideal electrocatalyst must be inexpensive, stable, more active for the desirable reaction relative to possible side reactions, and possess optimal porosity for efficient mass transport. The perspective of this review is to provide an overall insight into the most vital electrocatalysis for electrochemical energy conversion within the sustainable and environmentally friendly water and nitrogen cycles, which constitute essential building blocks for the future energy landscape. For the water cycle, the transformation of renewable electricity into chemical energy in the form of covalent bonds of H_2 and O_2 via water electrolyzers largely depends on the OER at the anode.[24-26] The ORR is crucial for the subsequent electricity generation and H_2O production via PEMFCs.[10, 27-28] For the nitrogen cycle, NRR and AOR catalytic processes relate to the breaking and forming of N≡N bonds,[29] respectively, ideal for electrochemical ammonia (NH_3) synthesis from N_2 and DAFCs via utilizing NH_3 as a carbon-free fuel.[15, 30] The

electrochemical community has recognized the complexity, challenges, advantages, and benefits of these cohesive, clean energy-environment cycles. The current field of energy-related electrocatalysis devotes to studying the OER, ORR, NRR, and AOR catalysts. Nevertheless, most studies focus on single or binary reactions, lacking an inherent connection as well as a comprehensive understanding of these water and nitrogen-related reactions.[5, 10, 29] Therefore, we are primarily motivated to combine all of these reactions in one review to highlight the importance of advanced electrocatalysis for clean energy technologies relying on these water and nitrogen reactions.

The rational design of catalysts with optimal structures, morphologies, and chemical compositions has led to encouraging strides in improving electrocatalytic activity, stability, and selectivity. However, the more challenging technical barrier is how to incorporate catalysts into electrochemical devices under realistic reaction environments properly. Isolated studies on electrocatalysis without considering actual working environments in applied energy devices are insufficient for practical applications. Therefore, in this review, firstly, we summarize the current understanding of the design and synthesis of both platinum-group-metal (PGM) and PGM-free catalysts for the OER, ORR, NRR, and AOR as mentioned above. Secondly, we put particular emphasis on the advances in membrane electrode assembly (MEA) technologies with favorable interfaces for mass and charge transfer in practical devices, including PEM electrolyzers, PEMFCs, electrochemical NH_3 synthesis, and DAFCs, respectively. Finally, we outline the perspectives and potential research directions for the assessment of remaining issues in terms of performance and

durability for these clean and sustainable energy devices.

2. The OER for PEM Electrolyzers

Utilizing renewable energy to split water into H_2 and O_2 and subsequently recombining them into fuel cells for electricity generation along with water formation is the desirable water cycle for energy applications.[31] Water-splitting technologies for H_2 production are clean and sustainable but are still far from being economically competitive against traditional fossil fuel-related process.[32-34] The most significant contributor to the low efficiency of H_2 production from water splitting is the slow kinetics of the OER process. Slow kinetics imposes a considerable overpotential, which is similar to its reversible reaction, *i.e*., the ORR at the cathode of fuel cells.[35-36] Currently, producing H_2 *via* water electrolysis is mainly based on aqueous alkaline electrolytes and PEM electrolyzers. Relative to alkaline systems, PEM electrolyzers have distinct advantages such as a more compact structure, capability to operate at much higher current density (up to 2.2 A cm^{-2}),[37] load flexibility, gas purity, and a fast-dynamic response.[38-39] **Table 1** summarizes critical system standards of industry PEM electrolyzers to understand the current status better. Alkaline media could provide a more significant opportunity to use PGM-free OER anode,[40-44] but still face many grand challenges such as the relatively slow HER and the lack of high-performance anion exchange membrane (AEM) electrolytes/ionomer.[6, 8, 24, 45-49] Here, we only focus on the more economically feasible acidic PEM electrolyzers. Compared to the HER easily conducted at a higher proton concentration (*i.e*., in a lower pH value), developing efficient and stable OER catalysts for use in acidic electrolyzers is of paramount importance.[38, 50]

Table 1 The system standards of PEM water electrolyzers.[a]

Characteristics	PEM Electrolyzers	Units	Notes
Current density	1.5–2.2	A cm^{-2}	
Cell voltage	2.70–3.96	W cm^{-2}	Reference voltage: 1.8 V
Electrical efficiency	50.3–55.8	kWh kg^{-1}-H_2	Electrolysis system only.
System efficiency	45–71	%	
System lifespan	10–30	years	
Total uninstalled capital cost	460–1053	\$ kW^{-1}	

[a]Data source: 2017 National Renewable Energy Laboratory (NREL) analysis,[51], and 2020 DOE Hydrogen and Fuel Cells Program.[52]

2.1 Understanding of OER Mechanisms

Relative to the HER, the OER is a much slower process during water splitting. Although the well-known Pt catalyst is the best performing for the HER and ORR, Pt is not an ideal catalyst for the OER in either acidic nor alkaline electrolytes due to the formation of the insert molecules PtO and $Pt(OH)_3$ during the OER in acids.[53] Alternatively, scientists have identified Ir, Ru, and their oxides as the most active catalysts for the OER, which studied them both experimentally and theoretically.[54-55] The mechanism of OER in acidic electrolytes comprises a four-step electron transfer procedure with multiple intermediates, as illustrated below.[56]

$$2H_2O \rightarrow 4H^+ + O_2 + 4e^-,\ E^0 = 1.23\ V \quad (1)$$

$$2H_2O \rightarrow *OH + H_2O + H^+ + e^- \quad (2)$$

$$*OH + H_2O \rightarrow *O + H_2O + H^+ + e^- \quad (3)$$

$$*O + H_2O \rightarrow *OOH + H^+ + e^- \quad (4)$$

$$*OOH \rightarrow O_2 + H^+ + e^-. \quad (5)$$

The calculated total free energy variation of OER is 4.92 eV,[57] which can be allocated equally

among the four steps, corresponding various adsorbates *OH, *O, *OOH, and O_2. If this is true, the equilibrium potential drives the OER. Nevertheless, constant adsorption free energy discrepancy between *OH and *OOH is estimated to be 3.2 eV for all oxides studied.[35] The placement of *O (in Eq. 4) between *OH (in Eq. 3) and *OOH (in Eq. 5) in the mechanism enables possible reduction of free energy. However, the minimum value of overpotential is still estimated to be 0.2-0.4 V, which suggests sluggish kinetics of the OER.[56]

2.2 OER Catalysts in Acidic Electrolytes

In recent years, the development of acidic OER catalysts for PEM electrolyzers specifically relies on PGMs such as Ru, Ir, and their oxides (*e.g.*, IrO_x and RuO_x).[58] Given the rapid deactivation of RuO_x catalysts, Ir or IrO_x are the most desirable. Unfortunately, the low abundance and high cost of Ir greatly limits the large-scale application of PEM electrolyzers. Searching for earth-abundant PGM-free OER catalysts has only made minor progress due to the grand stability challenges in acids.[43, 59] Some formulations have been studied including MnO_x,[60] Ti-MnO_2,[61] $Ni_xMn_{1-x}Sb_{1.6-1.8}O_y$,[62-63] NiFeP,[64] Ba[Co-POM],[65] and FeN_4/NF/EG,[66] but these still suffer from large overpotentials and poor stability. Some typical PGM and PGM-free OER catalysts studied recently for acidic electrolytes are summarized in Table 2. In this section, we highlight the most promising OER catalysts for PEM electrolyzer applications.

Table 2. Parameters for the different PGM and PGM-free OER catalysts in acidic electrolytes.

Catalysts	Overpotential (mV)	Tafel slope (mV dec^{-1})	Loading (mg cm^{-2})	Electrolyte	Ref.
[a]$IrO_x/SrIrO_3$	270	_	_	0.5 M H_2SO_4	[58]
[a]IrO_x-Ir	250	43.7	0.133	0.5 M H_2SO_4	[67]
[a]Li-IrO_x	270	39.0	0.125	0.5 M H_2SO_4	[43]
[b]$Ir_{0.7}Ru_{0.3}O_x$ (EC)	269	39.7	0.0600	0.05 M H_2SO_4	[68]
[a]Ru_1-Pt_3Cu	220	_	0.0163	0.1 M $HClO_4$	[69]
[a]Ru@IrO_x	282	69.1	0.0510	0.05 M H_2SO_4	[70]
[a]FeN_x/NF/EG	294	129	5.70	0.5 M H_2SO_4	[66]
[a]Co_3O_4/FTO	570	80	_	0.5 M H_2SO_4	[63]
[a]Ba[Co-POM]	361	97	_	1.0 M H_2SO_4	[65]
[a]NiFeP	540	_	0.102	0.05 M H_2SO_4	[64]
[a]$Ni_{0.5}Mn_{0.5}Sb_{1.7}O_y$	672	60	_	1.0 M H_2SO_4	[62]

[a] and [b]: obtained the current density at 10 and 5 mA cm^{-2} (based on geometric area) correction, respectively.

2.2.1 Ir/Ru-based PGM OER Catalysts

The accurate determination of actual active sites during the OER is very challenging because phase transformation in surface layers often occurs in a potential oxidative range, which represents a grand challenge of the fundamental understanding of OER active sites. Therefore, experimental studies need to combine with theoretical density functional theory (DFT) calculations. A typical example in exploring active OER catalysts was demonstrated by Jaramillo and his coworkers, who reported an iridium oxide/strontium iridium oxide ($IrO_x/SrIrO_3$) catalyst prepared by leaching Sr from surface layers of $SrIrO_3$ film.[58] This catalyst requires an overpotential η of ~270 mV to generate 10 mA cm$^{-2}_{oxide}$, which is stable for 30 h during continuous testing in an acidic electrolyte, outperforming rutile IrO_2 and RuO_2 nanoparticle catalysts (Figure 2a). DFT calculations (Figure

2b) predicted that the possible structures (*i.e.*, IrO_3 or anatase IrO_2) are kinetically active and epitaxially stabilized by the interface with $SrIrO_3$. The $IrO_x/SrIrO_3$ catalyst represents one of the best-performing OER catalysts in acids. Its exceptional stability, coupled with high intrinsic activity, would be very promising for PEM electrolyzers. However, it is challenging to prepare a large-scale $IrO_x/SrIrO_3$ film using the pulsed laser deposition for PEM electrolyzer applications. Thus, the development of cost-effective synthesis methods to develop OER catalysts with low Ir content is highly desirable. Introduction of transition metals (*e.g.*, Ni and Li) to Ir usually results in an encouraging boost in catalytic activities, because the modification of electronic/geometric structures can optimize bonding energies between OER intermediates and active sites. Strasser and his coworkers reported a core-shell $IrNiO_x@IrO_x$ catalyst (Figure 2c), which showed enhanced water-splitting performance and stability in acidic electrolytes relative to individual IrO_x catalysts.[59] The unique core ($IrNiO_x$)-shell (IrO_x) architecture contributes to the catalyst's enhanced intrinsic activity and reduces the Ir loading, while the corrosion-resistant oxide support is beneficial for catalyst durability improvements. Annealing temperatures during the synthesis are crucial for modifying OER activity (Figure 2d) as a desired IrNi metallic alloy phase is maintained only at $T \leq 300$ºC, temperatures that lead optimal chemisorption and reactivity of intermediates at the surface. In contrast to an annealing temperature of $T \leq 300$ºC, which benefits the overall synthesis, phase segregation into a NiO and an Ir-rich nanophase occur at $T = 400$ and 500ºC, respectively, and results in significant reductions in OER activities. Additionally, annealing at higher temperatures yields a smaller fraction of accessible $Ir^{3+/4+}$ active sites in the catalysts,

thereby lowering catalytic activity. Consequently, an optimal $IrNiO_x/IrO_x$ catalyst shows 2.5 times higher mass activity than the traditional IrO_x at an overpotential (η) of 280 mV (Figure 2e). Besides, introducing Li into IrO_x to prepare an amorphous Li-IrO_x catalyst shows a reduction of OER η of 270 mV at a current density of 10 mA cm^{-2} for ten hours of operation in acidic media, outperforming rutile IrO_2 (Figure 2f, g).[43] When compared to the periodically interconnected "rigid" [IrO_6] octahedrons in crystalline IrO_2, the iridium in the amorphous Li-IrO_x has disordered [IrO_6] octahedrons (Figure 2h). The oxidation of the amorphous catalyst during the OER leads to a shrinkage of the Ir−O bond, which is electrophilic and enhances both the hydroxyl oxidation kinetics and O=O bond formation to facilitate the turnover of water oxidation eventually.

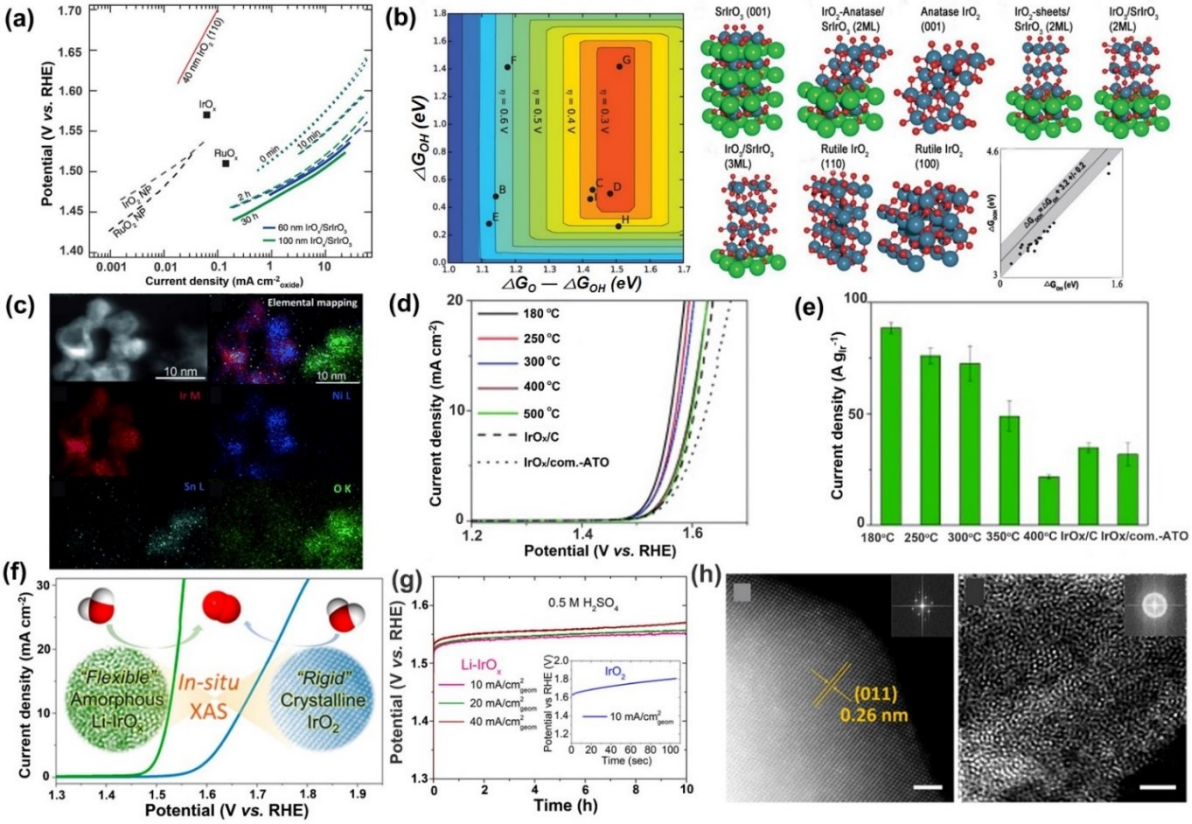

Figure 2. (a) Tafel plots comparing the specific activity of $IrO_x/SrIrO_3$ with OER catalysts in an acidic electrolyte, and (b) theoretical overpotential (η) volcano plot with *O and *OH binding energies as descriptors, (i-viii) visual representation of IrO_x and $SrIrO_3$ surfaces used for the DFT calculations, corresponding to the labeled points (B-I indicates i-viii, respectively) (Sr, green; Ir, blue; O, red), (ix) *OH and *OOH binding energies (black circles) overlaid on the universal scaling relationship (gray line with shaded uncertainty). Reproduced with permission.[58] Copyright 2016, AAAS. (c) HAADF-STEM image of the $IrNiO_x$/Meso-ATO-180 core-shell NP catalyst synthesized from PA-$IrNi_{3.3}$/Meso-ATO-180, and the corresponding elemental mapping of Ir, Ni, Sn, and O, respectively, (d) electrocatalytic OER activities of $IrNiO_x$/Meso-ATO-*T*, IrOx/C, and commercial IrOx/com.-ATO measured using LSV, and (e) Ir-mass-based activity at η=280 mV overpotential of these different electrocatalysts. Reproduced with permission.[59] Copyright 2015, Wiley-VCH. (f) OER activity comparison between "rigid" crystalline IrO_2 and flexible amorphous Li-IrO_x, (g) chronoamperometry test of amorphous Li-IrO_x at 10, 20, and 40 mA cm^{-2}_{geom}, inset shows that of rutile IrO_x at 10 mA cm^{-2}_{geom}, and (h) structural characterization of rutile IrO_2 and amorphous Li-IrO_x, HAADF-STEM images of rutile IrO_2 and amorphous Li-IrO_x, scale bar: 2 nm, inset shows the corresponding Fourier transform. Reproduced with permission.[43] Copyright 2019, American Chemical Society.

Although the rapid degradation of Ru catalysts in a low-pH electrolyte is a great challenge, their intrinsic catalytic activity and higher relative abundance in the earth are still attracting

substantial research interest for OER electrocatalysis.[69, 71] The flexible redox state of Ru is the root cause of the high activity of Ru. [57] Its wide modulation spacing readily responds to the alterations in its valence state that are stimulated by the frequent adsorption/desorption of oxygenated species.[72] The moderate oxygen bonding on Ru, along with low oxygen bulk diffusivity, also contributes to its high reactivity for the OER. Nevertheless, the severe degradation of Ru-based catalysts is a primary bottleneck that restrains them from wider applications. The degradation mechanism is due to the transient dissolution arising from structural disturbance. The over-oxidation of Ru to Ru-O_x moieties during the generation of (H)O ligands demands oxidative environment under electrode potentials, where the active oxygen-coordinated Ru moieties likely detach from supports.[69]

Embedding single Ru atoms into a Pt-rich coordination environment (Figure 3a) has demonstrated the improvement in the dissolution resistance of Ru by suppressing local over-oxidation of Ru surface atoms.[69] The resulting Ru_1-Pt_3Cu catalyst delivers an overpotential of 220 mV at 10 mA cm^{-2} for the OER in acids (Figure 3b) and with ten times the longevity over commercial RuO_2. The enhanced activity and dissolution resistance are rationalized by DFT calculations on various Pt_xCu_{4-x}(111) (x=0, 1, 2, 3, and 4) surfaces (Figure 3c). The electronic structure and redox behavior of single atomic Ru anchored at the corner or step sites of the Pt-rich shell can be modified effectively due to the compressive strain of the Pt_{skin} shell. This unique structure leads to an optimized binding of oxygen intermediates, showing enhanced resistance to over-oxidation and Ru dissolution. Also, alloying and compositing strategies help integrate Ru and

Ir species to overcome their limitations. A heterostructured Ru@IrO_x catalyst with unique physicochemical properties has demonstrated improved activity and stability simultaneously when compared to individual RuO_2 and IrO_2[70] (Figure 3d). This synergy is possible due to a charge redistribution existing between a highly strained Ru core and a partially oxidized Ir shell across the metal-metal oxide heterojunction (Figure 3e). The synergistic electronic and structural interactions may be associated with the enhanced catalytic activity and stability due to the increased valence of the Ir shell and the decreased valence of the Ru core (Figure 3f). Further researches are dedicating to addressing remaining serious issues, including (i) elucidating surface species in-situ produced and active for the OER, (ii) identifying the effective depth of catalytic surface layers, (iii) discerning metal dissolution, and (iv) clarifying doping effect to reduce PGM loading and enhanced performance.

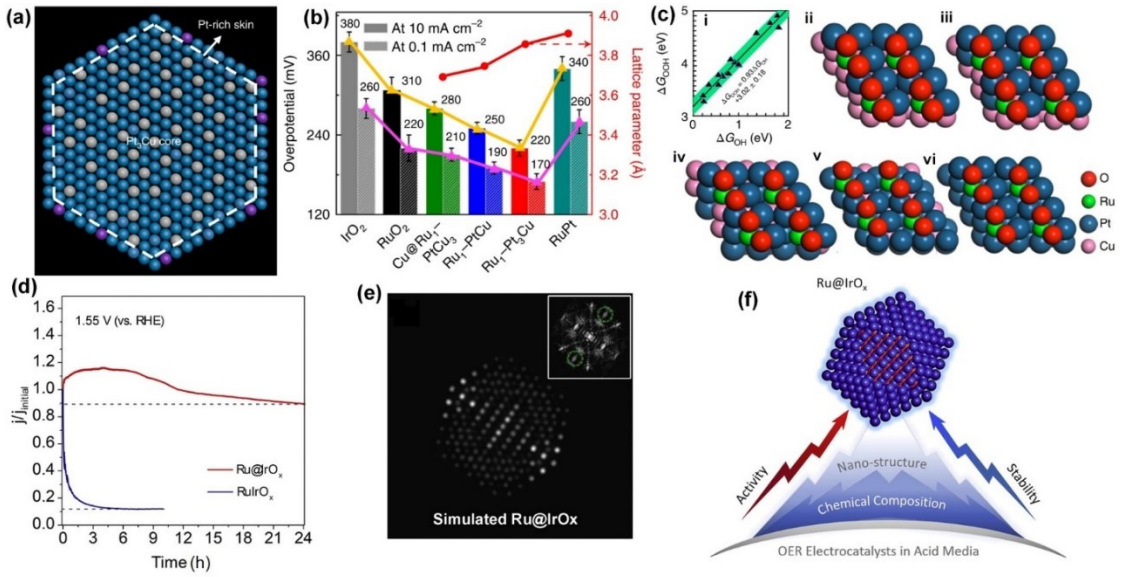

Figure 3. (a) Schematic atom model of Ru_1-Pt_3Cu, (b) overpotential to 0.1 mA cm^{-2} and 10 mA cm^{-2} for the catalysts (left axis) and lattice parameter dependence on the composition of Pt/Cu (right axis, red line), and (c) overpotential and electronic structure on Ru_1-Pt_xCu_{4-x}(111) with pre-adsorbed oxygen: (i) the linear scaling relation between the free energies ΔG of OOH and OH on the alloy surfaces considered, and (ii-vi) optimized structures of Cu (111) (ii), $PtCu_3$

(111) (iii), PtCu (111) (iv), Pt_3Cu (111) (v), and Pt (111) (vi) with surface-embedded Ru_1 atoms and 0.50 ML pre-adsorbed oxygen. Reproduced with permission.[69] Copyright 2019, Springer Nature. (d) Current-time chronoamperometric response of Ru@IrO_x and $RuIrO_x$ electrocatalysts at 1.55 V, (e) simulated HR-STEM image of a Ru_{147}@Ir_{414} icosahedral model structure along with its [112] axis (model adopted and modified from Wang et al.[73]), and (f) scheme of a core-shell Ru@IrO_x heterostructured nanocrystal in acid media. Reproduced with permission.[70] Copyright 2019, Cell Press.

2.2.2 PGM-free OER Catalysts for PEM electrolyzers

Although PGM such as Ir and IrO_2 are commercial OER catalysts in PEM electrolyzers for efficient hydrogen production, high PGM loadings (2-4 mg_{PGM}/cm^2) are required, which is not sustainable and limits their large-scale use. Although the development of PGM-free OER catalysts in acids is urgent, the severe stability issue of most nonprecious metal compounds in acidic and oxidative environments makes it more challenging. Efforts to develop earth-abundant PGM-free catalysts focus on promising Co, Ni, and Fe, likely due to their *d* orbitals with lower crystal-field activation energies.[24] However, most of the current reports on this topic only present initial activity, rather than long-term stability. The following are typical examples of Co, Ni, and Fe-based materials for OER catalysts and provide insight into possible PGM-free active sites. Blasco-Ahicart and co-workers prepared Co-containing polyoxometalates (Co-POMs) with a unique molecular structure through a simple metathesis method (Figure 4a).[65] Modification of Co-POMs by Cs^+ and Ba^{2+} to form water-insoluble salts led to enhanced OER activity in acid media. The Ba[Co-POM] catalyst shows promising catalytic activity towards the OER at pH<1, outperforming IrO_2 catalysts (Figure 4b). Encouraging performance of the Ba[Co-POM] catalyst is due to the polyanionic nature in POMs, which makes it easy to selectively incorporate desired ancillary

counter-cations near their active sites, without affecting their structure or chemistry. Generally, metal-based oxides usually are stable in alkaline electrolytes, but not in acids.[44] One such exception, a Ni-Mn antimonate catalyst ($Ni_{0.5}Mn_{0.5}Sb_{1.7}O_y$, Figure 4c, d), exhibits favorable OER activity with an initial η of ~672 mV at 10 mA cm^{-2} in 1.0 M H_2SO_4 along with enhanced stability for a 168-hour operation (Figure 4d),[62] showing no noticeable degradation of surface layers with a depth of 300 nm (Figure 4c). The improved stability is due to the formation of a crystalline $NiSb_2O_6$ rutile-type phase, which is a more stable Ni-containing antimonate phase for the inhibition of the dissolution of Ni. Following strategies are useful to improve $Ni_xMn_{1-x}Sb_2O_6$ catalysts further, including (i) the identification of the active sites of the catalyst and increasing the density of catalytically active sites, (ii) the improvement of the conductivity of the catalyst, (iii) the incorporation of more Mn without dissolution, and (iv) the combination of theoretical studies with experimental results to understand the catalytic mechanism. The FeN_4 sites embedded into the carbon matrix have been widely investigated in terms of their well-known ORR activity in acidic electrolyte.[74] Recently, Hou and his coworkers incorporated FeN_4 sites into carbon nanofibers supported by electrochemically exfoliated graphene (FeN_4/NF/EG, Figure 4e).[66] The hybrid catalyst exhibited promising catalytic activity for the OER in acid with a low η of ~294 mV at 10 mA cm^{-2}, and the value is lower than that of Ir/C catalysts (320 mV). DFT calculations further elucidated that the FeN_4 moieties are active sites for the OER, capable of reducing potential barriers. The addition of poisoning KSCN in the acidic solution resulted in dramatically decreased activity, thus verifying the theoretically predicted FeN_4 active sites (Figure 4f).[66] Although the

fundamental understanding on OER active sites in acids is insightful, long-term stability of FeN_4 sites embedded into the carbon matrix is still a deep concern for the acidic OER due to the serious carbon corrosion. Therefore, carbon-free formulations are more desirable for the OER. In alkaline media, Ni and Fe sites have demonstrated a synergistic effect with optimal adsorption and desorption energies for the OER. Therefore, these two metals were selected to constitute amorphous NiFeP materials (Figure 4g), in which the element P with appropriate electronegativity is used to stabilize the Ni and Fe atoms in acids.[64] The bulk amorphous NiFeP catalysts exhibited reasonable OER activity with a η of 540 mV at 10 mA cm^{-2} and showed negligible degradation for 30 h of continuous operation in 0.05 M H_2SO_4 (Figure 4h). The electrochemical impedance spectroscopy (EIS) measurement further indicated a fast charge transfer on NiFeP catalyst during the OER (Figure 4i). This work highlighted the importance of amorphous NiFeP materials in terms of their activity and stability for the OER in challenging acidic media.

Overall, PGM-free catalysts exhibited limited activity and stability, and their overall performance is disappointing, especially the stability issues under long-term operation. Also, due to the lack of *in-situ* characterization techniques to monitor the catalyst surface changes during the OER, the nature and structures of real active sites remain elusive. Further theoretical understanding is crucial for elucidating active sites and reaction mechanisms. Development of high-performance OER catalysts with sufficient activity and stability in acids is very challenging, but still possible through the design of innovative hybrid nanocomposites, such as coating or embedding OER active sites onto highly conductive and acid-resistant substrates.

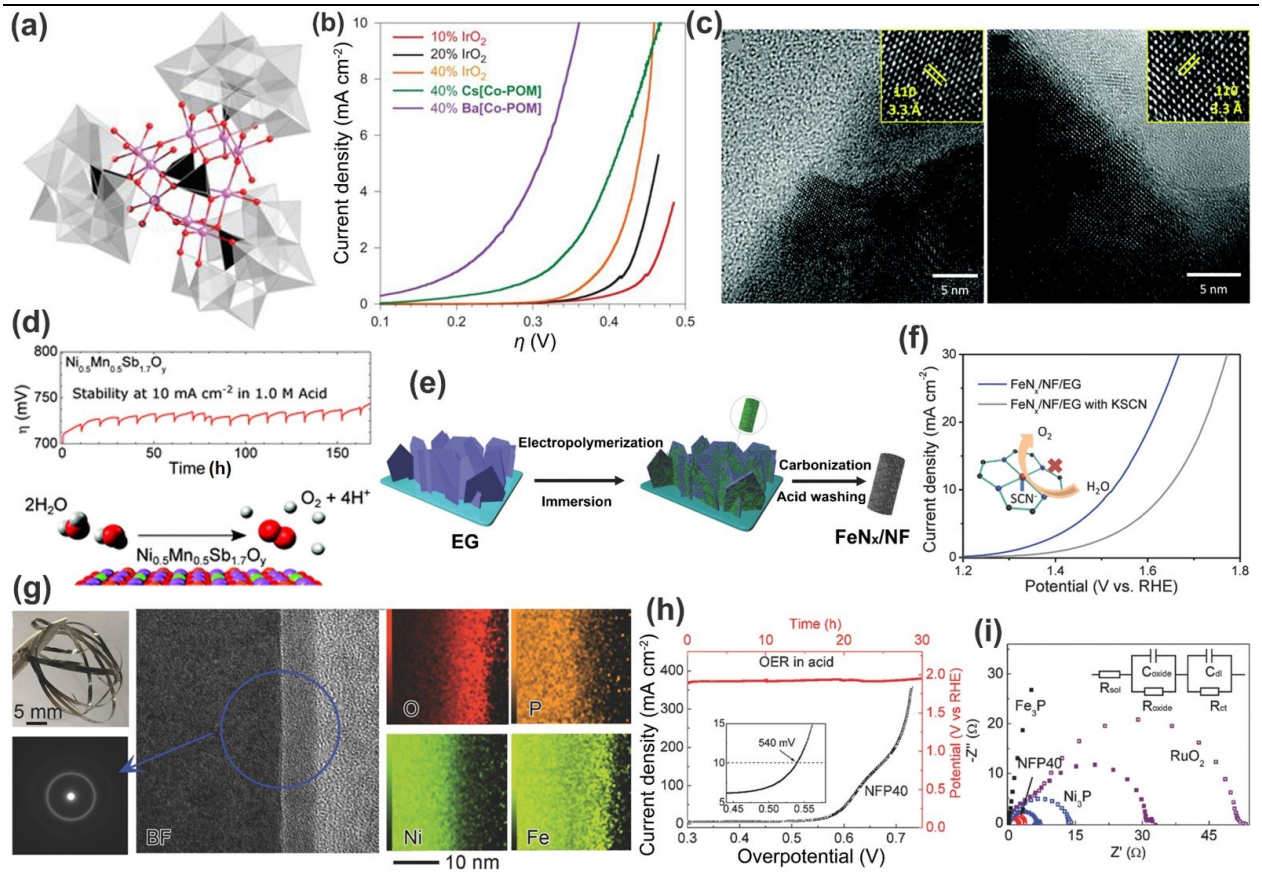

Figure 4. (a) Molecular structure of the $[Co_9(H_2O)_6(OH)_3(HPO_4)_2(PW_9O_{34})_3]^{16-}$ cluster, and (b) comparative electrochemical behavior of catalyst/CP electrodes in 1.0 M H_2SO_4 solution, highlighting the superior activity of Co-POM modified electrodes for OER. Reproduced with permission.[65] Copyright 2017, Springer Nature. (c) Structural characterization of $Ni_{0.5}Mn_{0.5}Sb_{1.7}O_y$ catalyst before (left) and after (right) chronopotentiometry for 144 h at 10 mA cm^{-2} of geometric area, and (d) its stability test at 10 mA cm^{-2} in 1.0 M H_2SO_4(aq) along with the schematic of water oxidation on the catalyst surface. Reproduced with permission.[62] Copyright 2017, the Royal Society of Chemistry. (e) Schematic illustration of the synthetic procedure, red points, and green materials represent Fe particles and polyaniline, respectively, and (f) poison experiment of FeN_x/NF/EG without and with KSCN solution under OER condition in 0.5 M H_2SO_4, inset is an illustration of Fe center impeded by the SCN^- ions. Reproduced with permission.[66] Copyright 2018, Wiley-VCH. (g) Optical photograph of $Ni_{40}Fe_{40}P_{20}$ (NFP40), and HRTEM image, electron diffraction pattern, and EDS profiles for the cross-section of a sliced NFP40 sample, and (e) LSV curve and stability of NFP40 in 0.05 M H_2SO_4, as well as (i) Nyquist plots of NFP40, the inset of panel (i) shows the equivalent circuit model for EIS data fitting. Reproduced with permission.[64] Copyright 2017, Wiley-VCH.

2.3 MEA Studies for PEM Electrolyzers

Beyond the rotating disk electrode (RDE) testing, implementing promising OER catalysts as the

anode in a PEM electrolyzer is critical in evaluating the device's performance.[75] Generally, H_2O oxidizes at the anode to generate O_2 and H^+, while protons selectively transfer across the PEM to the cathode side and combine with electrons supplied from power sources to form H_2 (Figure 5a). Due to high anodic potentials in acids, most studied PGM-free materials are vulnerable to corrosion and cannot be practically utilized for OER anodes yet in PEM electrolyzers. Therefore, recently reported MEAs for PEM electrolyzers are limited to Ir- and Ru-based materials.[54] However, the state-of-the-art IrO_2 and RuO_2 catalysts are also susceptible to serious dissolution issues during long-term operation, requiring further optimization of composition and structure/morphology.[37] Additionally, to improve PGM utilization, nanosized Ir and Ru catalysts should be effective in enhancing mass activities.[67] Compared to commercial Ir-blacks, an IrO_x-Ir composite catalyst demonstrated significantly improved MEA performance in PEM electrolyzers (Figure 5b). When the nanostructured IrO_2 was incorporated and dispersed in amorphous alumina (IrAlG), the nanocomposite anode generated a current density of 1.78 A cm^{-2} at 1.8 V (Figure 5c), comparable to $IrRuO_x$ (1.8 A cm^{-2}) in PEM electrolyzers.[76] This work shows that reducing Ir content while maintaining OER activity can be achieved, and especially indicates the high utilization of active Ir species. Increased surface area and optimal microstructures also improve MEA performance as evidenced by an IrAlG catalyst with a relatively high BET surface area of 131 m^2 g^{-1}.

In addition to Ir, RuO_2 is more active for the OER in acids. However, it is susceptible to severe corrosion because it tends to form unstable RuO_4.[37] The stability of RuO_2 can be enhanced

significantly after admixture with IrO_2 in an anode, because the electrons available on IrO_2 sites can be shared simultaneously with RuO_2 sites, thus preventing Ru from being oxidized to RuO_4.[68] Therefore, investigations on bimetallic Ir- and Ru- oxides could combine the high intrinsic activity of RuO_x and the high stability of IrO_x [67-68]. Recently, a binary IrRu oxide catalyst is synthesized by using electrochemically leaching Ru from metallic Ir-Ru alloys. The optimal $Ir_{0.7}Ru_{0.3}O_x$ significantly increased the cell efficiency during 400 h of electrolyzer stack operation (Figure 5d and 5e).[68] The improved OER activity of $Ir_{0.7}Ru_{0.3}O_x$ (EC) is due to that the surface O^{I-} species and surface-formed hydroxyls are active for the OER. Accordingly, dealloying strategies could enhance the OER catalytic activity of IrO_x-based materials immensely. Nevertheless, the method is challenging to scale up, and it is challenging to fabricate porous catalyst layers to deposit on the membrane and then transfer into devices.

A new concept of ultra-porous Ir-based hollow microspheres ($Ir_{0.7}Ru_{0.3}O_2$) proposed by Faustini and co-workers is to the development of a network of anisotropic Ir-based NPs.[77] The superiority of this porous material lies in its ease of integration into an MEA for PEM electrolyzers. The achieved MEA performance (1.0 A cm^{-2} at 1.656 V) using the $Ir_{0.7}Ru_{0.3}O_2$ OER anode (1.8 mg cm^{-2}) is in the upper range for catalysts with similar compositions reported in the literature (Figure 5f). Also, an aged-MEA characterization further verified its stability during the long-term test. This work provides an insightful concept that considers the MEA issue when designing new OER catalysts. Overall, improving efficiency and reducing the cost of PEM electrolyzers are significant challenges, which limit their large-scale implementation for hydrogen production.

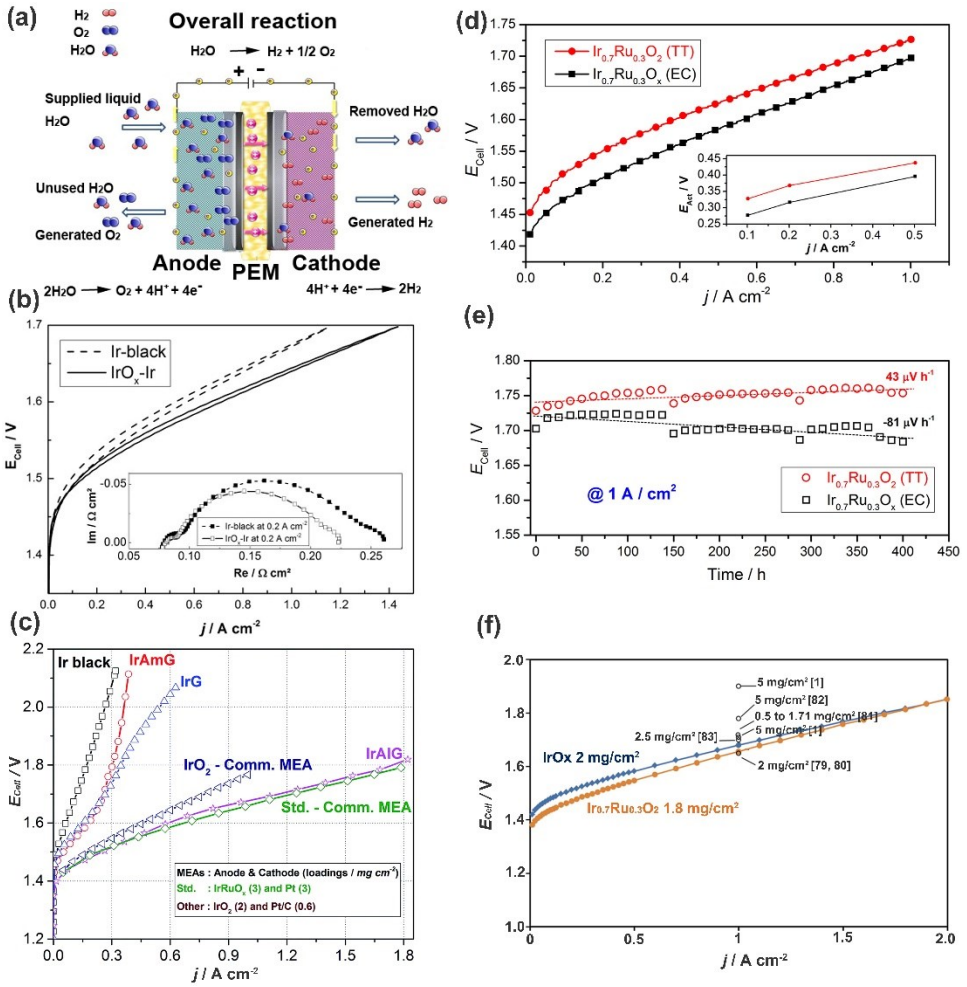

Figure 5. (a) Schematic view of components, working principles of PEM Electrolyzer. Reproduced with permission.[78] Copyright 2011, Elsevier. (b) Polarization curves of a 25 cm^2 PEM electrolysis cell at a scan rate of 5 mV s^{-1} at 80 ºC, Nafion 212, the inset shows the EIS at 0.2 A cm^{-2}. Reproduced with permission.[67] Copyright 2016, Wiley-VCH. (c) Polarization curves of PEM electrolysis with different anodic catalysts. Reproduced with permission.[76] Copyright 2017, The Royal Society of Chemistry. (d) 25 cm^2 PEM electrolyzer tests in a 2-cell stack, Nafion 212, and (e) 400 h durability test under a constant current density of 1 A cm^{-2}; inset panel in d shows the overpotentials only representing the charge transfer for EC and thermal treated (TT) catalysts. Reproduced with permission.[68] Copyright 2017, Elsevier. (f) Polarization curves obtained at 80 ºC, Nafion 115, and some comparison results with reported works.[1, 79-83] Reproduced with permission.[77] Copyright 2019, Wiley-VCH.

2.4 Challenge and Perspective of Sustainable Seawater Electrolysis

A less-discussed issue of PEM water electrolyzer technologies is the availability of highly purified

freshwater feeds. Freshwater is likely a scarce resource in many water-stressed countries and cannot be used reliably in PEM electrolyzers.[84-85] However, seawater presents an unlimited source of water for electrochemical hydrogen production, and the direct generation of hydrogen from seawater is proven to be feasible, though very challenging.[84, 86-88]

The key challenges in seawater electrolysis lie at the competition between anodic chlorine chemistry and the OER. In other words, the selectivity of the OER at the anode is low due to the competing chloride oxidation reaction (ClER).[86, 89] Chloride electrooxidation is complicated, and various reactions occur depending on temperature, potentials applied, and specifically the pH values.[90] At low pH solutions, the ClER ($2Cl^- \rightarrow Cl_2 + 2e^-$, E^0 = 1.36 V *vs.* SHE, pH = 0) is dominant, while hypochlorite forms under high pH environments ($Cl^- + 2OH^- \rightarrow ClO^- + H_2O + 2e^-$, E^0 = 0.89 V *vs.* SHE, pH = 14).[84] Compared to the sluggish $4e^-$ transfer reaction of OER, the ClER involves only $2e^-$. While thermodynamics favor the OER, the kinetics of the ClER is faster. Therefore, maximizing the difference of their thermodynamic potentials of both reactions would yield a wider potential window for selective OER. In principle, relative to acidic electrolytes, alkaline conditions are more desirable for seawater electrolysis with a potential difference ($\triangle E = E_{Cl^-}{}^0 - E_{OER}$) up to 480 mV.[87] Nevertheless, the larger overpotential for the OER *vs*. the ClER requires innovative designs of OER selective catalysts. Experimental explorations of selective OER catalysts towards saline water splitting have focused on Ru- and Co-based systems. Ru-based catalysts have shown selectivity for both the OER and the ClER. To date, only a few studies reported an improved selectivity towards OER.[87, 89] With the addition of Zn into the RuO_2 crystal

structure, the selectivity of the OER was enhanced at positive potentials in a chloride-containing acidic medium.[91] This enhancement occurs because the presence of Zn in rutile RuO_2 lattice breaks the perfect sequence of Ru atoms along the [001] direction and leads to the re-arrangement of the neighboring metal atoms in the [111] direction, possibly creating more oxygen vacancies on the surface near Zn ions. In this way, the chlorine-evolution process was affected by the re-arrangements in the rutile lattice, thus resulting in enhanced oxygen evolution when compared with that of nanocrystalline RuO_2.

An additional approach involves coating Cl^- blocking layers next to the OER catalyst, which can prevent the diffusion of Cl^- ions from the electrolyte to the surface of the OER catalyst.[88, 90, 92-93] A protective MnO_x coating seems an effective method to mitigate the ClER.[94] Koper *et al.* electrodeposited a thin film (~5–20 nm) of MnO_x on glassy carbon-supported hydrous iridium oxide (IrO_x/GC) in aqueous chloride-containing acid solutions (pH: ~0.9).[94] The MnO_x deposit proved to be catalytically inactive, and instead, it acted as a diffusion barrier that prevents Cl^- from reacting on the IrO_x catalyst underneath, improving the OER selectivity. At the same time, it can still facilitate the transport of water, protons, and O_2 between IrO_x and the electrolyte, which is necessary for OER activity. Alternatively, Ravichandran *et al.* have demonstrated that the application of a cation-selective layer (Nafion) can electrostatically repel Cl^- from the electrode surface, thus enhancing the OER.[92-93]

Unlike the grand challenge related to highly active and selective OER catalysts for the anode, the chemistry and catalyst material at the HER cathode seems more explicit.[87, 95] However,

seawater, which contains interfering ions and near-neutral pH values, also causes a low catalytic activity for the HER at the cathode. The stability of the cathode in the presence of chloride and oxidation products (*e.g.*, Cl_2) is a concern because possible Cl_2 would cross over from the anode to the cathode.[87] Innovative catalyst designs are required. For example, Ti mesh supported PtMo[96], and PtRuMo[95] alloys have exhibited high activity in seawater with <10% loss of their original current after operating for 172 h. The enhanced corrosion resistance of these reported alloys is ascribed to the competitive dissolution reaction between the guest M (*e.g.*, Mo, and Ru) species to Pt with Cl_2 in seawater.[96] Additionally, the introduced Mo, which has inherent corrosion resistance, is another reason these alloys show excellent stability for seawater splitting.[95] Also, the presence of non-innocent ions and bacteria/microbes in seawater often cause poisoning at the electrodes/catalysts, thus limiting the long-term stability of anodes.[84] These problems may further extend to membranes/ionomer in electrolyzers. Currently, the membrane used for the seawater electrolyzer in acidic electrolytes is Nafion. As a type of cation transporter, Nafion membranes are vulnerable to foreign ions, especially cationic impurities (e.g., Na+, Mg^{2+}, and Ca^{2+}) in seawater, which can be trapped and concentrated, resulting in a reduction in proton conductivity. Therefore, the development of advanced membranes with enhanced impurity tolerance and long-term stability is imperative for seawater electrolysis.

3. ORR Catalysts for PEM Fuel Cells

The ORR is one of the critical processes in many advanced electrochemical energy conversion technologies,[97] such as PEMFCs[98] and metal-air batteries.[7, 99-100] Particularly, the PEMFCs, which are zero-emission, high energy-conversion efficiency, high energy density, and fast refueling, are the most promising clean power source for transportation.[101-102] The proof of concept with scientific understanding can be traced back in 1842 by William Robert Grove, who used H_2 and O_2 on two platinum electrodes, respectively, immersed in a container of sulfuric acid for electricity generation. He named this primitive fuel cell a "gas battery."[103] Modern thin-film catalyst layers for PEMFCs were developed by Los Alamos scientists back in the 1990s,[104] and most of today's work focuses on developing better materials and efficient designs. Generally, due to difficulties in O=O bond activation/cleavage,[105] catalysts are the key to expedite the kinetically sluggish ORR at the cathode of a PEMFC.[29, 106-107] As one of the most high profile topics in electrocatalysis, the ORR has been studied extensively in the last few decades, and several excellent reviews are readily available in the literature.[10, 74, 101, 103, 108-112] Here, we outline future research directions based on new theoretical understandings and experimental advances, targeted explicitly for practical PEMFCs for transportation applications. Some vital parameters of the 2020 US. Table 3 summarize DOE technical targets related to PEMFCs for transportation applications.

Table 3. Technical targets of PEM fuel cells for transportation applications.[a]

Characteristics	PEM fuel cells	Units	Notes
PGM catalyst mass activity	0.44	A mg^{-1} PGM @ 0.9 $V_{iR\text{-}free}$	
PGM-free catalyst activity	>0.044	A cm^{-2} @ 0.9 V $V_{iR\text{-}free}$	Equivalent to PGM catalyst mass activity of 0.44 A mg_{PGM} at 0.1 mg_{PGM} cm^{-2}.
Performance @ 0.8 V	0.3	A cm^{-2}	Measured using polarization curve protocol.
Performance @ rated power (150 kMa_{abs})	1.0	W cm^{-2}	Measured using polarization curve protocol.
Start-up/shutdown durability	5000	cycle	< 5% decrease in voltage at 1.2 A cm^{-2}.
Durability with cycling	5000	hours	< 10% drop in rated power.
Cost	14	\$ kW^{-1}_{net}	High volume production (500,00080-kW_{net} system per year).

[a]Data source: 2020 DOE Hydrogen and Fuel Cells Program.[113]

3.1 Understanding of ORR Mechanism in Acidic Media

Pt-based materials,[109, 114] PGM-free catalysts (often with the metal-nitrogen-carbon: M-N-C formulations),[74, 115] and N-doped carbon (NC)[116] are studied as the standard benchmarks in theoretical work to uncover the mechanisms of ORR process. Depending on the active sites, ORR follows either a four-electron pathway to generate H_2O or a two-electron pathway to generate H_2O_2.[117] For the two-electron pathway, instead of O=O bond breaking, only the *OOH is produced as a reaction intermediate during the reduction process, as shown in the following equations:[109]

$$O_2 + 2(H^+ + e^-) \rightarrow H_2O_2,\ E^0 = 0.70\ V \quad (6)$$

$$O_2 + 2(H^+ + e^-) \rightarrow *OOH + (H^+ + e^-) \rightarrow H_2O_2. \quad (7)$$

In contrast, a complete reduction of O_2 to H_2O (a four-electron pathway) involves four elemental

steps. Both mechanisms are possible depending on the oxygen coverage at the catalyst surface. A high oxygen coverage leads to O–O cleavage posterior to *OOH formation (associative mechanisms). In contrast, low oxygen coverage causes O–O cleavage anterior to *OH formation (dissociation mechanisms). The associative pathway includes *OOH, *O, and *OH intermediates, whereas the dissociative one only involves *O and *OH).[109]

$$O_2 + 4(H^+ + e^-) \rightarrow 2H_2O,\ E^0 = 1.23\ V \quad (8)$$

$$O_2 + 4(H^+ + e^-) \rightarrow *OOH + 3(H^+ + e^-) \rightarrow *O + 2(H^+ + e^-)$$
$$\rightarrow *OH + 1(H^+ + e^-) \rightarrow 2H_2O \quad (9)$$

Despite major efforts to determine the rate-determining step during the ORR, conclusive understanding remains elusive since reaction pathways greatly depend on the catalysts and environmental parameters such as electrolytes, temperatures, and electrode potentials. Nevertheless, the kinetics of the ORR in most cases is limited by the following elemental steps: (1) the first electron transfer to adsorbed O_2 molecules, (2) the O=O bond breaking, (3) the hydration of O_2, and (4) the desorption of the intermediates.

3.2 Development of PGM and PGM-free ORR Catalysts

Pt-based nanomaterials are recognized as the most efficient ORR catalysts in practical low-temperature PEMFCs to date.[112, 117-119] Nevertheless, the high cost and scarcity of Pt are key obstacles for their widespread utilization. Catalyst layers in the PEMFC system represent over 40% of the total cost.[120] According to the US DOE, PEMFC costs should be dramatically reduced to an ultimate cost target of $30/kW to become economically viable.[121] Therefore, the development

of low-PGM or PGM-free catalysts with enhanced or comparable electrocatalytic activity and stability to their PGM counterparts is in high demand. Among studied PtM (M: Fe, Co, Ni, Cr, Cu, or Pb) alloy catalysts, the highly ordered intermetallic $L1_2$ Pt_3M_1 or $L1_0$ Pt_1M_1 exhibited significantly enhanced activity and stability in both aqueous acidic electrolytes and solid-state electrolyte-based MEAs.[112] Many PGM-free catalysts are also extensively explored, including M-N-C (M=Fe, Co, Mn, etc.),[64, 74, 122-124] heteroatom-doped carbon,[123, 125-127] oxides, chalcogenides, and oxynitrides.[44, 121] In particular, atomically dispersed and nitrogen coordinated MN_4 site-rich M-N-C catalysts exhibit promising ORR activity and stability in a low-pH environment as well as encouraging PEMFC performance.[98, 115, 122, 128] Traditional M-N-C catalysts developed in early stages of PGM-free catalyst research, such as the representative polyaniline (PANI)-derived Fe catalysts supported on Ketjenblack,[12] showed encouraging ORR activity. They significantly reduced the gap between PGM-free catalysts and the standard Pt/C catalyst. However, multiple carbon phases and metal species found in this catalyst make it difficult to understand its active components better.[129-130] Recently, exclusively atomically dispersed single metal MN_4 site catalysts with homogeneous carbon morphologies were developed by using metal-organic-framework (MOF) precursors, especially ZIF-8, with well-defined chemistry and structures.[131-133] These successes, therefore, lead to an increased density of active sites and strengthened M-N-C bonds with significant improvements in performance.[127, 132, 134-135] Combined with advanced physical characterization, DFT calculations predicted that the MN_4 sites are active and four-electron selective towards the ORR.[120, 125, 136] The representative PGM-based

and PGM-free ORR catalysts (Table 4) for PEMFCs are highlighted in terms of their synthesis, catalytic properties, and MEA performance in PEMFCs.

Table 4. Parameters for the different PGM and PGM-free ORR catalysts in acidic electrolytes.

Catalysts	$E_{1/2}$ (V *vs.* RHE)	Stability	H_2-air Fuel cell (j @ 0.6[a] or 0.8[b] or 0.9[c] V, A cm^{-2})	Ref.
Pt/PGC	0.88	–31 mV (30k cycles, 0.60-1.0 V)	1.03[a]	[137]
Pt_3Co@Co-NC	0.96	_	1.30[a]	[138]
Pt/40Co-NC-900	0.92	–12 mV (30k cycles, 0.60-1.0 V)	0.27[b]	[139]
$L1_0$-CoPt/Pt	0.97	–7 mV (30k cycles, 0.60-1.0 V)	0.56[c]	[140]
(CM + PANI)-Fe-C	0.80	_	0.09[b]	[115]
1.5Fe-ZIF	0.88	–30 mV (40k cycles, 0.60-1.0 V)	0.075[b]	[141]
ZIF-NC-0.5Fe-700	0.84	–31 mV (30k cycles, 0.60-1.0 V)	0.91[a]	[142]
20Co-NC-1100	0.80	–30 mV (10k cycles, 0.60-1.0 V)	_	[122]
Co-N-C@F127	0.84	–40 mV (30k cycles, 0.60-1.0 V)	_	[143]
Mn-NC-second	0.80	–17 mV (30k cycles, 0.60-1.0 V)	0.35[a]	[144]

3.2.1 PGM Catalysts for the ORR

Generally, PtM catalysts are studied based on two basic principles: Pt nanostructures with particle size effects and facet dependence and alloying with transition metals such as Ni, Fe, or Co.[118, 120, 145] Particle size effects partially originate from the structure sensitivity of single crystal facets.[110] Reducing the particle size is effective in promoting the ORR performance of Pt nanoparticles (NPs) due to a variety of reasons.[101, 110, 117, 137, 146] Downsizing the NPs can result in larger surface areas

exposed to electrocatalytic reactions. Also, small NPs tend to hold dense low-coordinated species (*e.g.*, edges, steps, and kinks), which are more capable of obtaining high electrocatalytic activity due to their high surface free energy.[120] The ORR is also a structure-sensitive reaction as apparent from extensive investigations on different Pt facets, particularly in different electrolytes with weak or strong adsorption capability.[110, 120, 147] In a weakly adsorbing electrolyte (*e.g.*, 0.1 M $HClO_4$), the specific activity (SA) follows an order of Pt(100) << Pt(110) ≈ Pt(111), due to the electronic effects or binding strength of intermediates. In a strongly adsorbing electrolyte (*e.g.*, 0.5 M H_2SO_4), the ORR activity increases in the order of Pt(111) < Pt(100) because strong adsorption of anions greatly deactivates the Pt(111) surface. The Pt cubic and octahedral nanocage enclosed by (100) and (111) facets (Figure 6a) presented enhanced ORR activities compared to commercial Pt/C (Figure 6b).[148]

A wide variety of PtM alloys have been studied extensively to reduce Pt content and enhance intrinsic activity/stability, including PtNi, PtCo, PtFe, PtV, PtTi, PtCr, PtAg, PtAl, and PtW).[102, 117] Because alloying can effectively modulate the atomic and electronic structures of Pt.[149] The short-range electronic charge-transfer effects (ligand effects) and long-range geometric lattice strain (geometric effects) are the main factors that modify chemisorption characteristics for adsorbed oxygen species at a PtM surface.[29, 120, 150-151] The Pt *d*-band center can shift due to electronic and geometric modifications, which adjust surface adsorbate bond strengths related to reactants, intermediates, and products.[105, 117, 140] A volcano-type relationship exists between specific activities of Pt_3M (M = Ni, Co, Fe, Ti, and V) with the *d*-band center (Figure 6c) indicative

of reaction rates. The optimal oxygen-intermediate adsorption associated with the respective removal of surface oxides, electron, and proton transfer should be not too weak and too strong.[151-152] Pt_3Co, Pt_3Ni, and Pt_3Fe alloys located at the top of the volcano are the most effective alloy materials. As a result, adsorption strength becomes optimal for the ORR by tuning the components, shapes, and sizes of PtM alloys.[153] Also, interactions between Pt nanoparticles and carbon supports could lead to synergistic effects that would enhance catalytic activity.[154-158] For example, Pt-Co core-shell NPs deposited onto carbon matrix containing Co-N_4-C and Co@ graphene active sites (Figure 6d) leads to highly efficient ORR performance, and recorded mass activity of 12.36 A mg_{Pt}^{-1} at 0.9 V was measured with an optimal catalyst (Figure 6e).[138] Compared to traditional fcc-Pt alloys, the fully ordered PtM intermetallic NPs have exhibited improved activity and stability for the ORR, which was demonstrated clearly by Sun and his coworkers. The hard-magnet core/shell $L1_0$-CoPt/Pt NPs with 2-3 atomic layers of strained Pt shell (Figure 6f) yield a much higher specific activity (~38 times) and mass activity (~19 times) when compared to a commercial Pt/C (Figure 6g).[142] The $L1_0$-CoPt/Pt NPs catalyst is exceptionally robust, and the electrochemical active surface area (ECSA) is not lost after 30, 000 accelerated durability test (ADT) cycles in an MEA under practical operation conditions (0.6 to 0.95 V).[142] The underlying mechanism of the exceptional CoPt/Pt catalyst stems from the ligand effect of Co and the strain of the Pt skin layers, which are capable of weakening the binding of ORR intermediates and subsequently enhancing intrinsic activity. Further doping a third transition metal into PtM bimetallic alloys could lead to further catalytic activity and durability enhancements. In theory, Pt_3Ni catalysts have the highest

intrinsic activity but suffer from poor stability due to the possibility of phase separation. The ternary Pt_3NiM octahedra-based alloys on carbon supports contain V, Cr, Mn, Fe, Co, Mo, W, and Re as the third metals.[150] DFT calculations (Figure 6h) indicate that, among others, Mo prefers subsurface positions near the particle edges in a vacuum and surface vertex/edge sites in oxidizing conditions, which promotes the activity and stability of the Pt_3Ni catalyst. As a result, the Mo-Pt_3Ni/C exhibited the best ORR activity (Figure 6i), which are 81- and 73-fold enhancements of specific and mass activities, respectively, when compared to the commercial Pt/C.[150] Relative to traditional spherical Pt particles, one-dimensional (1D) anisotropic structures expose reactive high-index facets, plenty of edges, corners, and step-edge atoms, therefore showing significantly enhanced catalytic activity towards the ORR. [136] The experimental observation was further supported by DFT calculations.[136, 159] For example, jagged Pt nanowires enable ultrahigh mass and specific activity, a feature attributed to their under-coordinated surface atoms, high mechanical strain, large ECSA, and unusual rhombic structures on the surface.[136, 159] The binding energy of intermediates, especially, is reduced due to optimal mechanical strain, a feature that is again supported by DFT calculations.

However, the high ORR activity of PtM catalysts measured in aqueous acidic electrolytes often fails to translate into high-performance MEAs with solid-state Nafion ionomer electrolyte. The primary challenges are associated with the utilization of Pt active sites (*i.e.*, ECSA determined by CO striping), proton conductivity (Nafion film coverage and thickness), mass transfer (*i.e.*, tortuosity and porosity), water flooding caused by extremely hydrophilic surface, and possible

metal contamination (*i.e.*, dissolution of M from PtM) of membranes and ionomers within the 3D cathode. Ink preparation with optimal solvents and ionomers, along with electrode fabrication, is crucial for achieving high MEA performance. Among studied PtM catalysts, several PtM catalysts have successfully demonstrated the moderate activity and stability of MEAs, which exceeds DOE activity (0.44 A mg^{-1}_{PGM} at 0.9 $V_{IR\text{-}free}$) and stability targets (<30%, 30,000 cycles from 0.60 to 0.95 V). However, the remaining challenge is further reducing the Pt loading at the cathode (< 0.1 mg cm^{-2}) while maintaining sufficient power density and performance durability.

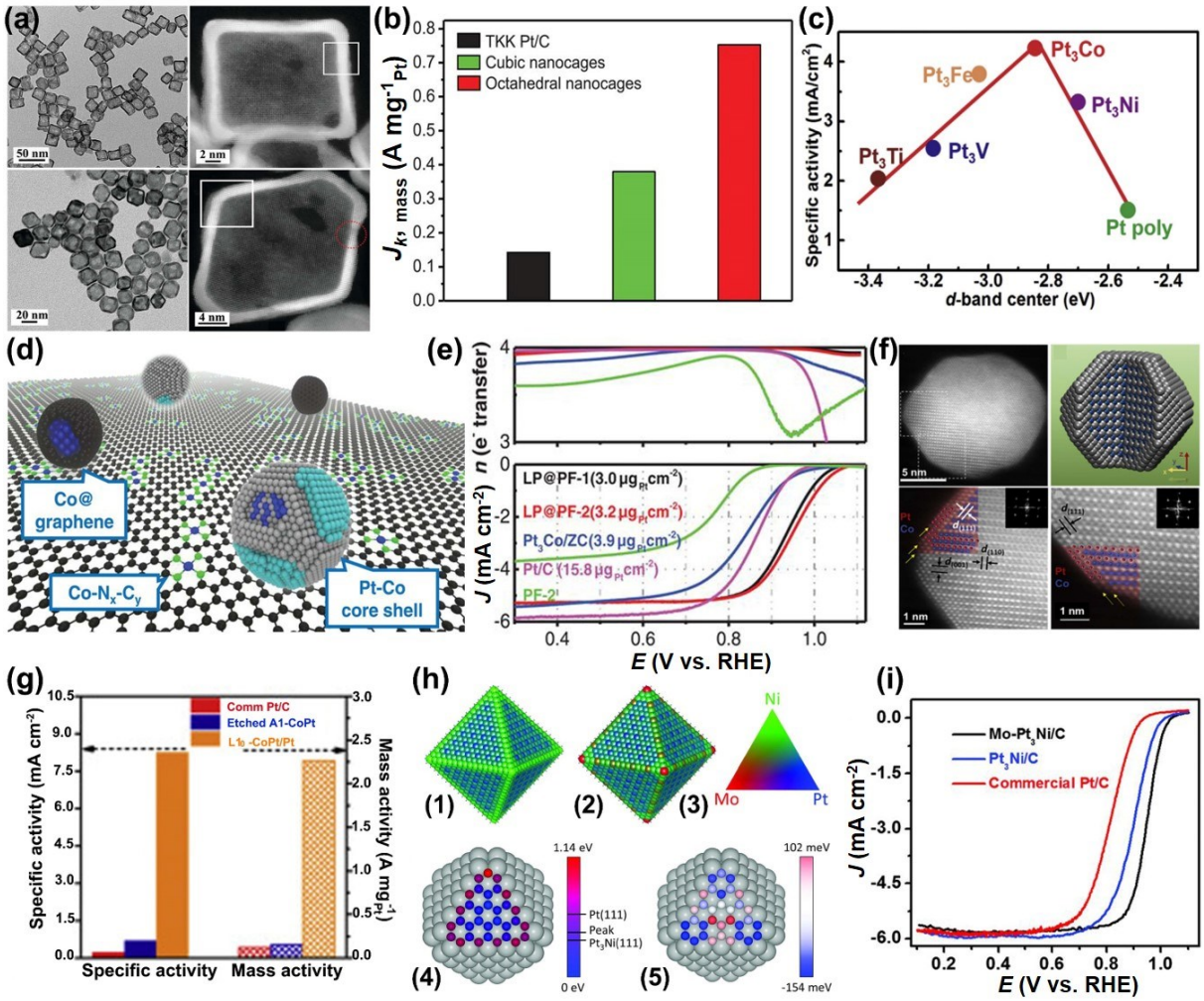

Figure 6. (a) Transmission electron microscopy (TEM) and high-angle annular dark-field (HAADF)-scanning transmission electron microscopy (STEM) images of Pt cubic (top) and octahedral nanocages (bottom), and (b) their corresponding ORR MA comparison. Reproduced with permission.[148] Copyright 2015, AAAS. (c) Volcano-like relationships between the catalytic properties and electronic structure of Pt_3M alloys. Reproduced with permission.[151] Copyright 2007, Springer Nature. (d) Schematics of an ultralow concentration Pt alloy supported over PGM-free materials (LP@PF) showing coexistence of Pt-Co NPs, Co@ graphene, and Co-N_4-C PGM-free active sites, and (e) the corresponding RRDE polarization and electron transfer number curves. Reproduced with permission.[138] Copyright 2018, AAAS. (f) $L1_0$-CoPt/Pt core/shell structure with an atomically thin Pt shell, and (g) the specific and MA comparison with commercial Pt/C and etched A1-CoPt. Reproduced with permission.[140] Copyright 2019, Cell Press. (h) The average site occupancies of the second layer of (1) the $Ni_{1175}Pt_{3398}$ nanocrystal and (2) the $Mo_{73}Ni_{1143}Pt_{3357}$ nanocrystal, suggested by (3) color map. (4) Binding energies for an oxygen atom on (111) of the $Mo_6Ni_{41}Pt_{178}$, relative to the lowest binding energy. Gray spheres represent Pt atoms, and colored ones indicate oxygen sites. Binding energy on the fcc site of Pt(111) surface and Pt_3Ni(111) surface and the peak of Sabatier volcano are labeled for comparison. (5) The change in binding energies when a $Ni_{47}Pt_{178}$ nanocrystal is transformed into a $Mo_6Ni_{41}Pt_{178}$ nanocrystal. (i) ORR performance of the Mo-Pt_3Ni/C, Pt_3Ni/C, and commercial Pt/C. Reproduced with permission.[150] Copyright 2015, AAAS.

3.2.2 PGM-Free ORR Catalysts

Significant dependence on Pt would limit the large-scale application of PEMFCs for transportation and other applications. Henceforth, the exploration of low-cost and earth-abundant substitutes to Pt-based ORR catalysts, especially in challenging acidic media, is scientifically and technologically significant.[160] Therefore, the development of active PGM-free catalysts is the grand challenge for ORR electrocatalysis.[36, 112] As mentioned above, the M-N-C-based atomically dispersed single metal catalysts represent the best-performing PGM-free catalysts in acids for PEMFCs so far.[160-163] Of these, a wide variety of studied M-N-C catalysts includes Fe-N-C,[64, 115, 162, 164] Co-N-C,[10, 122, 143, 165-166] Cu-N-C,[147, 167] Ni-N-C,[168-170] and Mn-N-C.[146, 171] Among studied transition metals, Fe and Co are standout choices for high ORR activity.[98, 115] At the same time, Mn-N-C catalysts show promising stability due to the minimal Fenton reactions between Mn and H_2O_2, making them ideal for membranes and ionomers in MEAs. Recent reviews provided a

comprehensive summary of these M-N-C catalysts.[10, 29, 74, 112, 172-173] Here, we briefly highlight the possible active sites, reaction mechanisms, notable achievements, and remaining challenges associated with M-N-C catalysts.

DFT calculations play a significant role in elucidating the nature and structure of active sites in the M-N-C catalysts as well as possible reaction pathways for the ORR. Based on binding energy calculations for possible ORR intermediates including O_2, *OOH, *O, *OH, *HOOH, and H_2O, FeN_4, CoN_4, and MnN_4, with a four-fold coordination number, are believed to be the most likely active sites in M-N-C catalysts (Figure 7).[115] Theoretical calculations predicted that FeN_4 sites are the most active among studied metal centers, capable of breaking O=O bonds and proceeding along the desirable four-electron ORR pathway. However, the bonding between FeN_4 sites and intermediates is often too strong,[43, 142] which limits intrinsic activity.

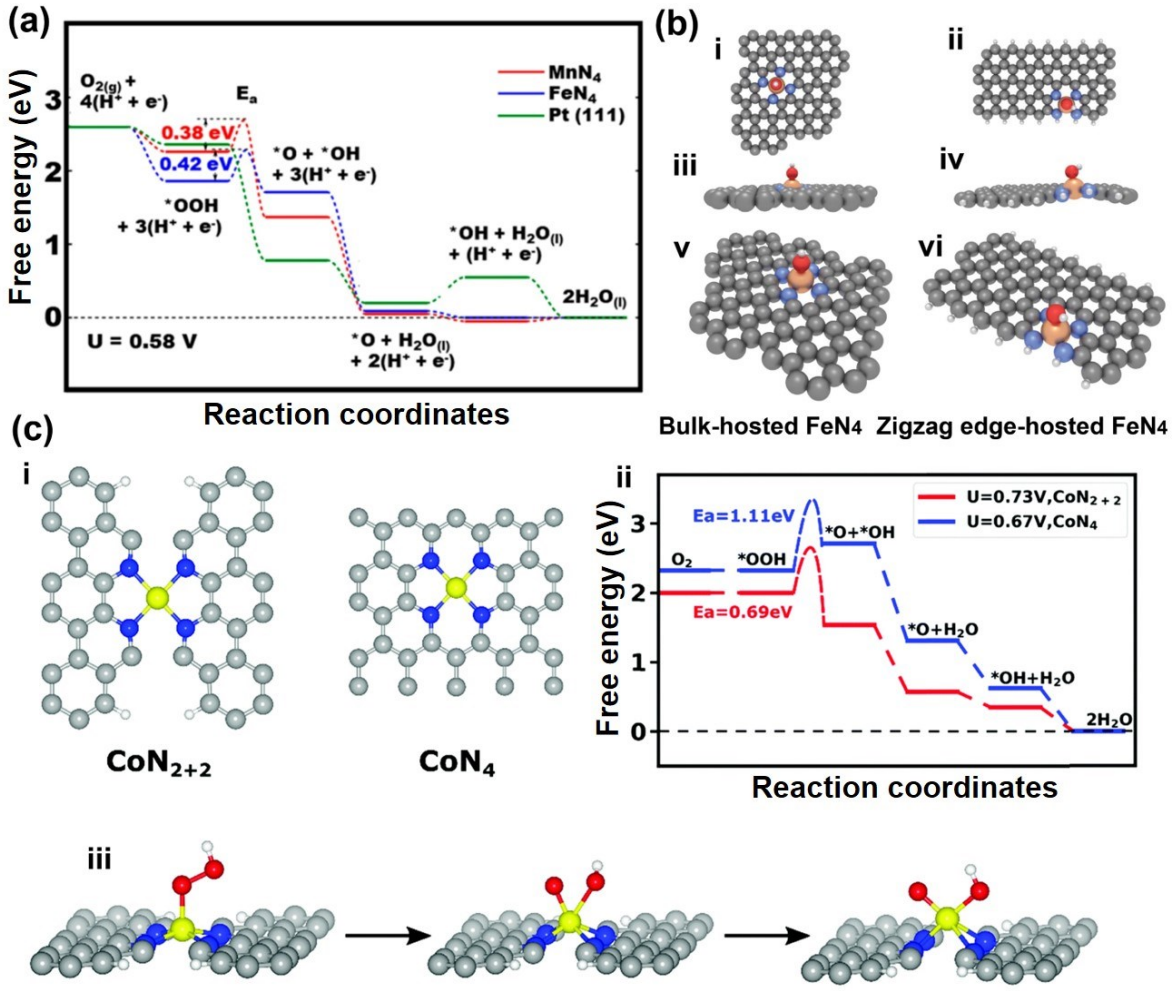

Figure 7. (a) Free energy diagrams for the four-electron oxygen reduction pathway on Pt(111), MnN_4, and FeN_4 sites under a limiting electrode potential of U = 0.58 V. Reproduced with permission.[171] Copyright 2019, Elsevier. (b) Model structures used in theoretical studies with spontaneously formed OH ligand. Reproduced with permission.[115] Copyright 2017, AAAS. (c) Atomic structure comparison between CoN_{2+2} and CoN_4 sites of Co-N-C catalyst (i), calculated free energy evolution diagram for $4e^-$ ORR pathway (ii), and (iii) atomistic structure of the initial state (left), transition state (middle), and final state (right) for OOH dissociation reaction on the CoN_{2+2} site. Reproduced with permission.[143] Copyright 2018, the Royal Society of Chemistry.

Aberration-corrected STEM can directly visualize the predicted active site of FeN_4, as depicted in Figure 8a,[115] which shows single Fe atoms dispersed in a few layers of graphene. Using a chemical doping approach through the partial replacement of original Zn ions in ZIF-8 precursors with Fe ions, we achieved complete atomic dispersion of FeN_4 sites in Fe-N-C catalysts

(Figure 8b).[98] The full atomic distribution led to unusual ORR activity in 0.5 M H_2SO_4 electrolyte with a half-wave potential ($E_{1/2}$) of 0.88 ± 0.01 V *vs.* RHE (similar to commercial Pt/C with a disk loading of 60 μg_{Pt} cm^{-2}). The doped Fe content in the precursor also affects overall catalyst morphology and chemistry, including carbon particle size, porosity, N-doping level, and carbon microstructure, which are all key factors determining ORR activity and stability. Due to the lack of sufficient nitrogen dopants to stabilize single Fe sites, the excess Fe content often causes the formation of inactive clusters, large particle sizes, and highly graphitized carbon, three features that hinder ORR activity in acids. The primary obstacle challenge is introducing more nitrogen doping and carbon defects into carbon hosts to accommodate more atomic FeN_4 sites, which in turn requires new concepts and methods for catalyst synthesis.[173] Given identical FeN_4 configurations, the intrinsic activity of single atom M-N-C catalysts also depends on their local carbon structures. The coordinating N atoms at the edge behave differently to those in-plane ones to affect binding energies of metal sites with O_2 and intermediates as well as the reaction pathways due to the existence of dangling bonds.

Traditional co-pyrolysis of metal, nitrogen, and carbon sources led to limited catalyst activity because of poor control of both catalyst morphology and the local structures of active sites. We designed a carbon host model with defined structures and nitrogen doping by carbonizing ZIF-8 precursors at 1100ºC. Then we elucidated the formation mechanism of FeN_4 sites during the thermal activation (Figure 8c).[142] Because, in the model carbon host, the interaction between N dopants and Fe^{3+} is the only factor that changes during thermal activation. The inactive Fe-N

configurations formed at room temperature can thermally transfer into the active FeN_4 sites with optimal coordination numbers and bond length. Even a low temperature of 400ºC can generate relatively high activity ($E_{1/2}$ =0.79 V). The temperature at 700ºC results in further enhanced ORR activity($E_{1/2}$ =0.83 V), but a higher temperature of 1100ºC causes a decrease in the activity due to the loss of nitrogen dopants. Fe-oxide nanoparticles formed with a size typically less than 2 nm during the adsorption step at room temperature. However, they disappeared at a mild temperature of 400ºC, suggesting a thermally-driven transformation of Fe aggregates to atomic Fe sites in the carbon host with optimal pyridinic N dopants. The key knowledge generated is that traditional high-temperature treatments (>800ºC) are not essential for the formation of FeN_4 active sites. The structural strain of Fe-N bonds and charge distribution during thermal activation are the origins of the enhanced intrinsic activity and stability of FeN_4 sites. Molecular dynamics simulations and DFT calculations further confirm that FeO_x particles would lose Fe atoms, and then thermodynamically favorably form more stable FeN_4 sites. At lower temperature (*i.e.*, 400ºC), a single Fe atom would diffuse at the carbon surface until it is embedded into a vacancy defect with an N_4 moiety to form a stable FeN_4 site. At 700ºC, FeN_4 configurations have a lower symmetry around Fe atoms and shorter Fe–N bond lengths. The carbon layer embedded with FeN_4 sites undergoes off-plane ripples. Regarding the structural change of FeN_4 sites at a higher thermal activation temperature, we proposed an innovative concept of using a local contraction strain to simulate the effect of Fe–N bond length on ORR activity. The theoretical calculations predicted that the strained FeN_4 site up to -2% showed lower activation energy to break the O=O bond, which

is kinetically favorable for the ORR.

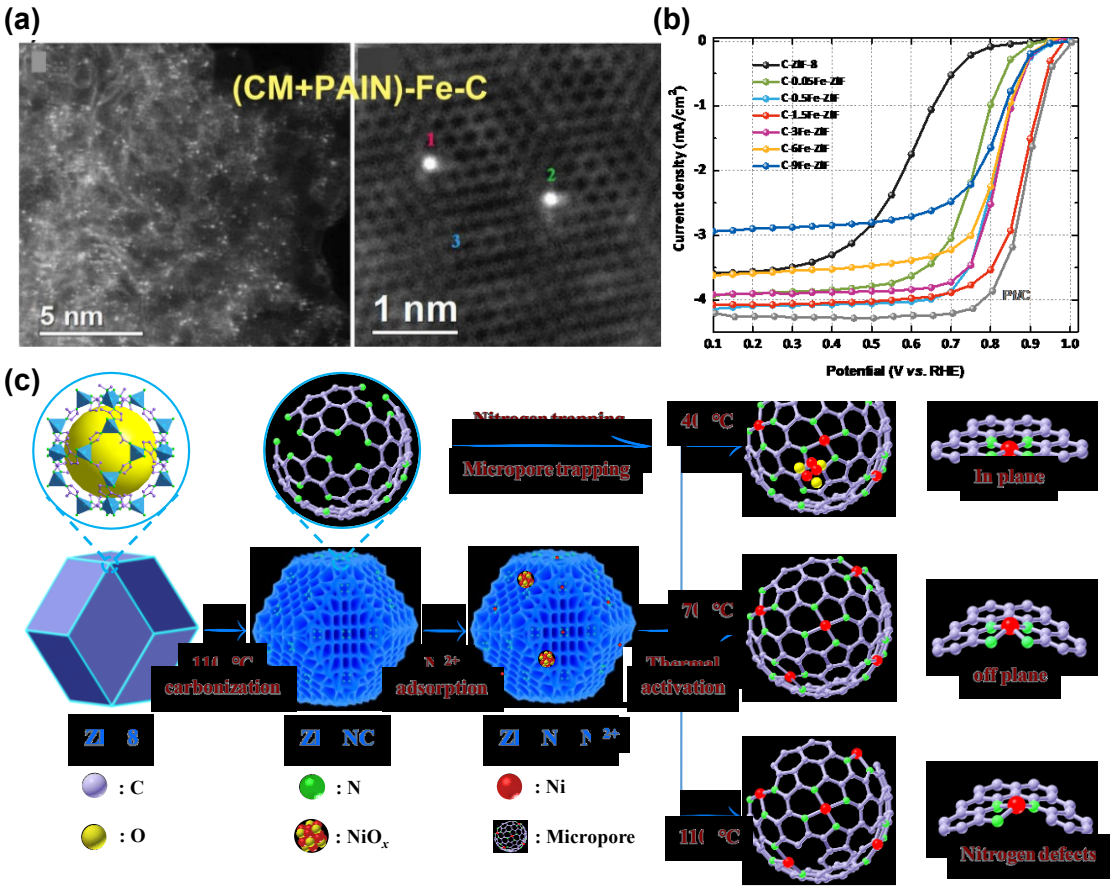

Figure 8. (a) Atomic-resolution HAADF-STEM image of the (CM+PAIN)-Fe-C catalyst. Reproduced with permission.[115] Copyright 2017, AAAS. (b) RDE ORR polarization plots for different Fe-ZIF catalysts as a function of the Fe content in the precursor (from 0 to 9 at%). Reproduced with permission.[141] Copyright 2019, the Royal Society of Chemistry. (c) Schematic of model systems established by adsorbing Fe into N-doped carbon. Reproduced with permission.[142] Copyright 2019, Wiley-VCH.

In addition to Fe-N-C catalysts, recent advances in Co-N-C[122, 142] and Mn-N-C[167] catalysts also attract increasing attention to PGM-free and Fe-free catalysts for PEMFCs. By using a surfactant-assisted MOF approach, a new type of atomically dispersed and nitrogen coordinated CoN_4 site-rich Co-N-C catalyst with a core-shell structure presents a significantly increased density of active sites (Figure 9a).[143] The new Co-N-C catalyst exhibited the highest ever recorded

ORR activity in acids with an $E_{1/2}$ of 0.84 *vs.* RHE, performance approaching that of most Fe-N-C catalysts (Figure 9b).[143] However, relative to Fe-N-C, Co-N-C catalysts still perform more poorly in kinetic ranges (>0.8 V) but exhibit more stable activity in acidic electrolytes. Both catalysts often undergo rapid initial activity losses. Nevertheless, Co-N-C catalysts are often remaining steadfast over time, while Fe-N-C catalysts gradually lose their activity. Both Co-N-C and Fe-N-C degradation mechanisms remain elusive and require deeper experimental and theoretical studies. The possible Fenton reactions between metals, especially Fe, and H_2O_2 (two-electron by-product during the ORR) would generate highly oxidative radical groups and, therefore, may cause severe degradation of organic ionomers, membranes, and catalysts. Among studied metals, Mn has negligible Fenton reaction behavior, but traditional Mn catalysts often show weak ORR activity in acids. Due to a recent breakthrough with atomically dispersed MnN_4 site catalysts,[43, 167] the development of MnN_4 site-rich Mn-N-C catalysts poses an incredible opportunity for the production of PGM-free catalysts that have little to no risk of Fenton reactions in cathodes.[10] Unlike Fe and Co, stronger binding between Mn and O prevents the formation of Mn-N bonds in active MnN_4 sites during the high-temperature synthesis. An innovative two-step doping and adsorption approach (Figure 9c) is useful to increase single Mn sites in Mn-N-C catalysts gradually. The catalyst delivered encouraging ORR activity with an $E_{1/2}$ of 0.80 *vs.* RHE and enhanced stability relative to Fe-N-C catalysts (Figure 9d).[146] Remarkable progress in enhancing M-N-C catalysts has been made in the last decade. However, PGM-free ORR catalysts are still plagued by their insufficient stability in acidic media, possibly as a result of metal

dissolution, carbon corrosion, and formation of oxidative H_2O_2 by-products,[123] which is discussed in next section.

Although MN_4 moieties in M-N-C catalysts are possible active sites, the actual site structure may include additional ligands such as OH or O. The adjacent carbon atoms next to MN_4 sites provide additional positions to facilitate the O=O bond breaking of the adsorbed OOH*. Besides, the redox of Fe^{2+}/Fe^{3+} involved in the ORR on the FeN_4, but the mechanistic understanding necessary to initiate the ORR on CoN_4 and MnN_4 sites is not yet clear. We must address the grand challenges associated with the low density of active sites, low intrinsic turnover frequency (TOF), and insufficient stability to make M-N-C catalysts viable for future applications. It is crucial to engineering the atomic dispersion of metals (Fe, Co, or Mn) and their coordination environments, N-doping and carbon defect, and carbon nano/microstructures and morphologies in catalysts.

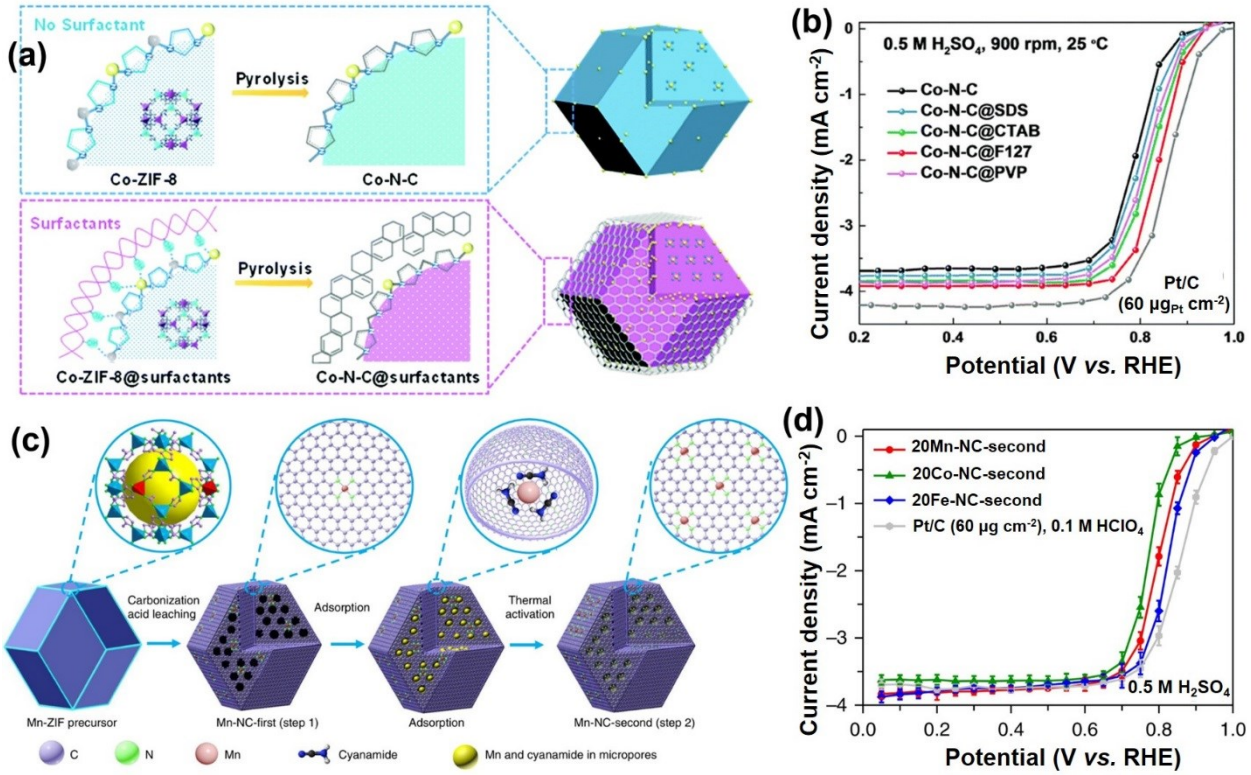

Figure 9. (a) Synthesis strategy of core–shell-structured Co–N–C@ surfactant catalysts with increased active site density, (b) their corresponding RRDE test. Reproduced with permission.[143] Copyright 2018, the Royal Society of Chemistry. (c) Schematic of atomically dispersed MnN_4 site catalyst synthesis, a two-step doping, and adsorption approach can gradually increase the density of the atomically dispersed and nitrogen-coordinated MnN_4 sites into the three-dimensional (3D) carbon particles, and (d) comparison of electrocatalytic activity of Fe-, Co- and Mn-N-C catalysts prepared from identical procedures. Reproduced with permission.[144] Copyright 2018, Springer Nature.

3.3 MEA Studies for ORR Catalysts

3.3.1 MEA Performance of PGM Cathodes

The design and fabrication of high-performance MEAs based on solid-state electrolytes, *i.e.*, Nafion, represent the other grand challenge in the field due to the lack of knowledge on interface control within 3D porous electrodes for efficient mass and charge transport. Most efforts on the development of ORR catalysts are limited to the RDE level. The activity of both PGM and PGM-

free catalysts determined by using RDE is often not consistent with real-world MEA performance.[118, 150, 174-175] The inefficient proton and O_2 transport within electrodes leads to extremely poor catalyst utilization. The generation of large quantities of H_2O products causes severe flooding in electrodes, hindering mass transport, and making some active sites inside micropores inaccessible. Thus, the significant discrepancy between RDE and MEA highlights the importance of involving MEA at the very beginning of catalyst material development.

In a typical PEMFC (Figure 10a), the ORR at the cathode occurs by consuming the protons and electrons to reduce O_2 molecules and produce water and heat. In general, cost, performance, and durability are the three primary criteria for PEMFC performance. The power density of MEA is critical performance merit.[108] Liu and her coworkers in 2018 reported a new PtCo cathode catalyst containing three different Co species: Pt-Co alloy, Co-N_x sites, and metallic crystallite encapsulated by onion-like graphitic layers (Co@graphene). Exceptional ORR activity and MEA performance are due to the possible synergy between those Co species and highly ordered Pt_3Co intermetallic particles. Specifically, at an extra-low Pt loading (0.035 mg_{Pt} cm^{-2}) in the cathode, the MEA generated a mass activity of 1.77 A mg_{Pt}^{-1}at 0.9 $V_{iR\text{-}free}$ (Figure 10b),[138] significantly exceeding the DOE 2025 target (0.44 A mg_{Pt}^{-1}).[138] Also, the MEA at 80ºC and 150 kPa air achieved a current density of 300 ± 10 mA cm^{-2} at 0.8 V, and a maximum power density of ~0.9 W cm^{-2}. Besides, the retained mass activity is 64% of its initial value after 30,000 voltage cycles, surpassing the catalyst durability goal of < 40% mass activity loss set by DOE.

PGM loadings in the cathode have a significant influence on the overall MEA performance,

which has been demonstrated by General Motors recently in a systematic study of PtCo cathodes at three Pt loadings (0.05, 0.10, and 0.20 mg_{Pt} cm^{-2} in Figure 10c).[174] With a reduction of Pt loadings to 0.1 $mg_{Pt}cm^{-2}$, the massive performance loss is observed at high-current density (>1 A cm^{-2}), due to insufficient ECSA of the catalyst and increased local O_2 resistance (R_{O2}^{Pt}). There are two significant methods to improve the performance of low-PGM electrodes: (1) to increase the ECSA of the PtM catalyst, and (2) to reduce the local O_2 transport. Generally, the improvement of catalyst dispersion or the use of a Pt monolayer catalyst can complete the first strategy. At the same time, optimizing the ionomer/Pt interfaces and the use of high-oxygen-permeable ionomers facilitate mass transport within 3D electrodes. GM scientists established a benchmark performance of MEA with an optimal cathode providing an ECSA of 45 m^2/g_{Pt}, and R_{O2}^{Pt}) value of 20−25 s cm^{-1} by using a PtCo/HSC alloy catalyst. A typical MEA with a cathode loading of 0.1 mg_{Pt} cm^{-2} generates current densities of 0.3 and 1.2 A cm^{-2} at 0.8 and 0.7 V, respectively, under conditions of 80°C, 100% RH, and 150 kPa_{abs} air.[174]

In addition to activity, durability (performance loss during voltage cycling) and stability (performance loss during potentiostatic/galvanostatic experiments) of PGM catalysts are highly challenging.[102] Because it has proven difficult to maintain desired crystal face as the particle size would decrease to < 10 nm and an inevitable change to the thermodynamically preferred “round” shape occurs on some shape-controlled catalysts. Therefore, shape-, fact-, and dimension controls may provide excellent opportunities to enhance the intrinsic and mass activity of PGM catalysts. Maintaining their unique structural and morphologic features under dynamic operation conditions

of FEVs is the critical challenge for PGM catalysts for transportation applications. Compared to other studied PtM catalysts, highly ordered intermetallic nanoparticles hold great promise to enhance catalyst stability in MEAs.[112, 119, 142] Also, optimal carbon supports with a balance between graphitization and porosity are crucial for improving catalyst stability through enhanced metal-support interactions and carbon corrosion resistance.[118, 137]

3.3.2 MEA Performance of PGM-free Cathodes

To significantly reduce the cost of MEAs, improving the performance of PGM-free cathodes would be highly desirable for future PEMFC technologies. In 2017, Zelenay and his coworkers carried out MEA tests based on the Fe-N-C-(CM+PAIN) catalyst. The H_2-air MEA performance reached maximum power densities of 0.39 and 0.42 W cm^{-2}, respectively, depending on the air flows (200 *vs.* 760 mL min^{-1}) used (Figure 10d).[115] Recently, Litster and his coworkers achieved a new MEA performance milestone by using the atomically dispersed Fe-N-C catalysts developed by Wu's group in Buffalo.[128] In particular, a current density of 0.028 A cm^{-2} at 0.9 $V_{IR\text{-}free}$ or of 44 mA cm^{-2} at 0.89 $V_{HFR\text{-}free}$ can be generated under conditions of H_2-O_2 at 80°C and 1.0 bar (Figure 10e).[176] Meanwhile, under practical conditions of H_2-air, 100%RH, 80°C, and 1.0 bar, the MEA also yielded a current density of 113 mA cm^{-2} at 0.8 V close to DOE 2020 target (150 mA cm^{-2}). Increasing the cell temperature to 94°C and the air backpressure to 1.7 bar can achieve an ever record peak power density of 610 mW cm^{-2} and a rated voltage power density of 410 mW cm^{-2} at 0.67 V. The exceptional MEA performance represents the best for PGM-free cathode (Figure 10f).[176] In addition to the high intrinsic activity of the catalyst,[64, 98] carefully controlling the

interfaces through the optimization of primary and secondary catalyst sizes in electrodes is imperative to achieving exceptional MEA performance. However, due to the insufficient density of active sites in Fe-N-C catalysts, the corresponding PGM-free cathodes suffer from severe mass transport limitations and generated insufficient power density, primarily due to a much thicker PGM-free electrode (100 μm *vs*. ~10 μm in PGM cathodes). Also, water flooding becomes more significant in PGM-free cathodes. Performance at an RH of 60% is higher in contrast with RH of 100%.[142] The reason behind this is that the dense and aggregated morphologies of catalysts cause non-uniform ionomer dispersion in the cathode, which blocks effective catalyst utilization. Therefore, further optimization of electrode structures is critical for ionomer dispersion improvement, mass transport promotion, and water flooding mitigation.

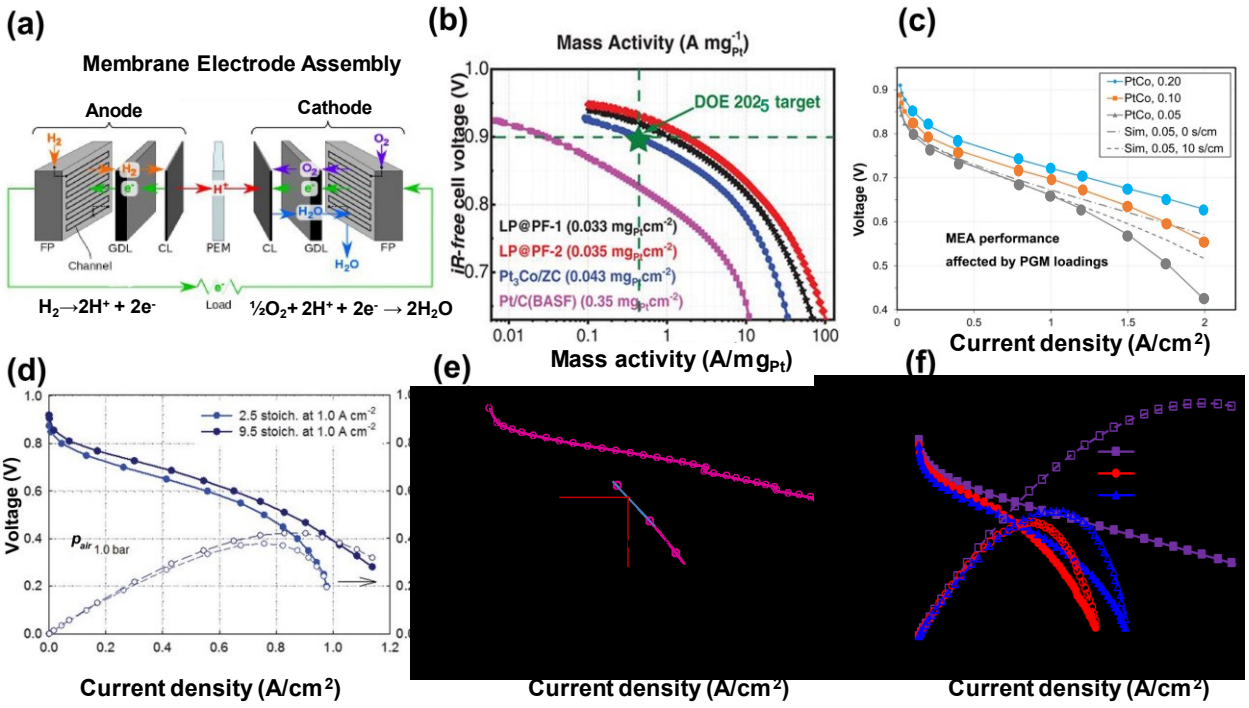

Figure 10. (a) A basic configuration of a single cell of PEMFC. Reproduced with permission.[141] Copyright 2019, the

Royal Society of Chemistry. **PGM catalysts**: (b) Cathodic MA Tafel plots derived from fuel cell measurement with the green star marked for US DOE 2025 target. Reproduced with permission.[138] Copyright 2018, AAAS. (c) Fuel cell polarization curves of PtCo cathodes at three Pt loadings (mg_{Pt} cm^{-2}). Operating conditions in the order of anode/cathode: H_2/air, 80ºC, 100/100% RH, 150/150 $kPa_{abs,\ outlet}$ · Single-cell, 5 cm^2 active area, and ≤25μm membrane thickness. Reproduced with permission.[174] Copyright 2016, American Chemical Society. **PGM-free catalysts**: (d) H_2-air fuel-cell polarization plots with (PAIN+CM)-Fe-C as the cathode catalyst at two different stoichs: 2.5 and 9.5, 100% relative humidity (RH), and 1.0 bar partial pressure. Reproduced with permission.[115] Copyright 2017, AAAS. (e) The polarization curves obtained under O_2 at 1.0 bar and (f) air at 1.7 bar for fuel cell performance of the atomically dispersed Fe-N-C catalysts. Reproduced with permission.[176] Copyright 2019, American Chemical Society.

Apart from the grand challenge of transferring catalyst activity into a high-performance MEA, understanding degradation mechanisms of PGM-free catalysts in MEAs is quite complicated, relating to both catalysts at the atomic scale and electrodes at the macro scale. Their degradation mechanisms during aqueous RDE or solid-state electrolyte MEA tests are likely different, due to significant differences in conditions such as temperature, pH value, local O_2 concentration, poisoning effects, and H_2O_2 production and lifetime. How to distinguish their contribution to the overall performance loss, however, is still unknown. In traditional RDE tests in an aqueous environment, we can elucidate the catalyst degradation process with a focus on active sites and carbon supports. Recently, we found that catalyst degradation in acids is dependent on the testing protocols associated with different mechanisms.[141] During rapid potential cycling between 0.60 and 1.0 V and even under O_2 environments in 0.5 M H_2SO_4 solution, carbon corrosion is negligible, and most of the atomically dispersed and nitrogen coordinated Fe sites remain intact, corresponding to less significant activity loss (Figure 11a-c).[141] However, holding at a constant potential of 0.85 V for 100 hours, the same Fe-N-C catalyst suffers from significant degradation, especially at relatively early on (around 20 hours). This degradation correlated to severe carbon

corrosion and the appearance of Fe clusters due to Fe-N bond breaking and Fe-Fe bond formation (Figure 11d-f).[141] The general understanding of degradation mechanisms suggests that strengthening M-N and C-N bonding in a robust and corrosion-resistant carbon host may improve catalyst stability. In particular, designing precursors with optimal M-N_4 complex, local hydrocarbons, and particle size (following appropriate thermal activation) are crucial for enhancing catalyst stability.

Besides the catalyst degradation caused by (1) M site dissolution, (2) doped N oxidation, and (3) carbon corrosion at the atomic level, possible micropore flooding and structure collapse in MEA electrodes may cause losses in proton and mass transfer, elements partially responsible for the MEA performance degradation (Figure 11g, h).[141] Currently, there are very few studies focused on the comprehensive diagnostics of MEA degradation for PGM-free cathodes. Similar to aqueous electrolytes, a rapid initial performance loss, along with a partial reversible performance recovery, was also observed in MEA tests, likely attributable to the catalyst degradation. However, MEA degradation, especially at kinetic ranges, is more rapid and dominant with a persistent declining trend. In addition to the possible demetallation and carbon corrosion in electrodes, the issue of H_2O_2 and membrane contamination by metals seems to be more serious. Traditional voltage cycles from 0.6 to 1.0 V in the N_2 atmosphere originally designed for PGM catalysts seem to cause no obvious changes in electrode structures. Therefore, the effective MEA stability accelerated stress test (AST) protocol is still under development by the U.S. DOE. Extensive *ex-situ* and operando electrochemical (CV and EIS at different RH%) and physical characterizations

(STEM, XAS, XPS) are crucial for providing insight into the alteration of electrodes during the durability tests. The performance loss is likely due to possible changes in ionomers, carbon structures, porosity, hydrophilicity/hydrophobicity, and catalyst/ionomer interfaces, which are responsible for the loss of charge transfer and mass transport. Recent reviews provided a detailed discussion of the possible degradation mechanisms.[177] In short, before PGM-free cathodes become viable in PEMFCs, the durability challenge must be overcome through the deciphering of the relevant degradation mechanisms to use this information to develop effective design strategies to enhance catalyst and electrode stability.

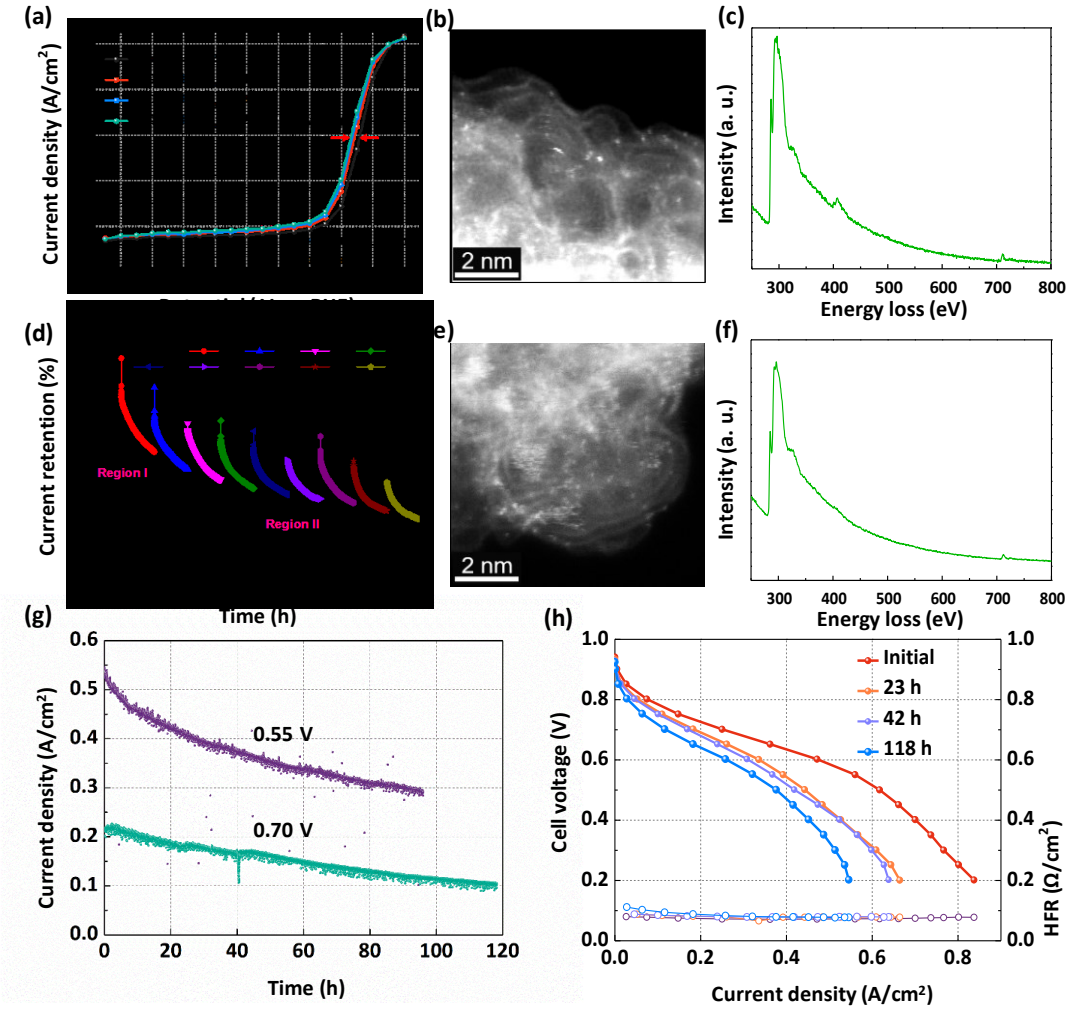

Figure 11. (a d) RDE stability tests of the best performing 1.5Fe-ZIF catalyst in O_2-saturated 0.5 M H_2SO_4 electrolyte using different test protocols. Structural changes by (b, e) STEM and (c f) EELS analysis. (a-c) Potential cycling between 0.60 and 1.0 V still showing significant atomically dispersed Fe sites coordinated by N. (d-f) Holding at a constant potential of 0.85 V for 100 hours, significant degradation especially at the initial stage accompanying with depicting appearance of Fe clusters and likely Fe-N bond breaking or weakening. (g) Fuel cell durability tests at a constant potential of 0.70 V and 0.55 V, respectively. (h) Fuel cell polarization plots recorded at different times during the 120-hour durability test at 0.70 V. Fuel cell cathode: catalyst loading 4.0 mg cm^{-2}; 100% RH; airflow at 200 sccm, 1.0 bar total partial pressure of gases. Anode: Pt/C, 0.20 mg_{Pt} cm^{-2}, 100% RH; H_2 flown at 200 sccm, 1.0 bar partial gas pressure. Membrane: Nafion® 212. Temperature: 80°C. MEA area: 5.0 cm^2. Reproduced with permission.[141] Copyright 2019, the Royal Society of Chemistry.

4. The NRR for Ammonia Electrosynthesis from N_2 and H_2O

Similar to the water cycle, utilizing earth-abundant nitrogen could realize a nitrogen cycle through ammonia electrosynthesis and electricity generation through using ammonia in a DAFC. Ammonia is essential to the global economy as a fertilizer feedstock and industrial chemical. Also, it is a promising hydrogen storage molecule and highly viable carbon-neutral fuel.[15, 106] Today, to supply NH_3 as a commodity chemical, industrial NH_3 synthesis is dependent on the Haber-Bosch process. This process requires high temperatures and pressures and, accounts for more than 2.0% of anthropogenic energy usage and releasing nearly 400 Mt/year of CO_2 emissions.[178] Aware of the enormous energy demands and negative environmental impact of the Haber-Bosch process, there is an increasingly urgent need for alternative technologies to replace the century-old process. Alternatively, electrosynthesis is promising for the generation of NH_3 from N_2 and H_2O through an electrocatalytic NRR process.[179] However, two significant factors dramatically limit the NRR for NH_3 electrosynthesis: low activity of catalysts to cleave N≡N triple bonds,[16, 180] and limited selectivity to compete with the HER process in aqueous electrolytes.

Alkaline media is desirable for the nitrogen cycle by using anion exchange membranes (AEMs)

for electrosynthesis of NH_3 and DAFCs.[38] NH_3 electrosynthesis also has been studied extensively in acidic media due to the availability of PEM, the ease to capture NH_3 in acids, and the high selectivity for NH_3 *vs*. N_2H_2.[181-184] However, the HER in acidic electrolytes is more dominant than in alkaline media, as proven by a current density that is two orders of magnitude higher.[183-185] Also, alkaline media allows the use of the PGM-free OER anode during the electrosynthesis of NH_3 by using H_2O rather than H_2 as the proton source. Employing H_2 during the electrosynthesis of NH_3 will introduce significant challenges related to H_2 production, transportation, and storage, which ironically contradicts the original purpose of utilizing NH_3 as the alternative H_2 carrier. Compared to H_2, H_2O is the more sustainable and economical proton source for the NRR. Thus, in this section, we mainly discuss the electrosynthesis of NH_3 in alkaline electrolytes via N_2 and H_2O. Table 5 summarizes the targeted standards set by the U.S. Advanced Research Projects Agency-energy (ARPA-e) Office in 2017 for making the ammonia electrosynthesis competitive to current Haber-Bosch processes.

Table 5. Targeted standards for electrosynthesis of ammonia technology.[a]

Specification	Electrosynthesis of ammonia	Units	Notes
Energy density	4.25	kWh L^{-1}	Liquified gas
Current density	>300	mA cm^{-2}	
Ammonia production rate	6×10^{-5}	mol $h^{-1}cm^{-2}$	Anion exchange membranes
Efficiency of fuel conversion	>50	%	
Electricity cost	7	MW metric ton^{-1}	
Cost	0.20	\$ kWh^{-1}	Estimated source to use energy (SUE), 55% efficiency

[a]Data source: 2017 U.S. advanced research projects agency-energy (ARPA-E) targets.[179, 186]

4.1 Understanding of NRR Mechanisms

The mechanism of the electrocatalytic NRR is complicated, and Greenlee and her co-workers have provided an essential in-depth discussion of catalyst categories and mechanisms.[15] Typically, the NRR proceeds via either associative or dissociative pathways at the surface of catalysts.[187] The main difference is the stage at which the breaking of N≡N triple bond occurs during the reduction processes. In the associative mechanism, the N≡N linkage remains intact during all of the hydrogenation steps. However, in the dissociative mechanism (Eq. 10), the N≡N linkage is broken before hydrogenation, leaving two adsorbed N-atoms at the catalyst surface. Based on a hypothesis that N_2 is adsorbed perpendicular to active sites, the associative NRR mechanism is divided into two ways including the distal (Eq. 11) and alternating pathway (Eq. 12) according to the hydrogenation sequence on the N atoms adsorbed at and away from the active site, respectively.[5, 179] These three possible reaction pathways are listed below:

Dissociative pathway:

$$N_2 + 2* \rightarrow 2*N + 2e^- + 2H^+ \rightarrow 2*NH + 2e^- + 2H^+ \rightarrow 2*NH_2 + 2e^- + 2H^+ \rightarrow 2NH_3 + 2* \quad (10)$$

Associative distal pathway:

$$N_2 + * \rightarrow *N_2 + e^- + H^+ \rightarrow *NNH + e^- + H^+ \rightarrow *NNH_2 + e^- + H^+ \rightarrow *N + NH_3 \rightarrow *N + e^- + H^+ \rightarrow *NH + e^- + H^+ \rightarrow *NH_2 + e^- + H^+ \rightarrow NH_3 + * \quad (11)$$

Associative alternating pathway:

$$N_2 + * \rightarrow *N_2 + e^- + H^+ \rightarrow *NNH + e^- + H^+ \rightarrow *NHNH + e^- + H^+ \rightarrow *NHNH_2 + e^- + H^+ \rightarrow *NH_2NH_2 + e^- + H^+ \rightarrow *NH_2 + e^- + H^+ \rightarrow NH_3 + * \quad (12)$$

4.2 Development of NRR Catalysts in Alkaline Electrolytes

Compared to reported works in acidic electrolytes, NRR catalysts in alkaline systems are relatively less studied.[188] Due to the recent development of AEM for alkaline fuel cells and electrolyzers, it would be a real opportunity to use AEM for the NRR by transferring OH^- to the anode to inhibit the HER at the cathode.[189] In this section, we mainly focus on reviewing experimental efforts of NRR catalysts studied in alkaline electrolytes to pave the way for the development of AEM-based electrolyzers for NH_3 synthesis.

Similar to ORR and OER catalysts, both PGM and PGM-free catalysts have been studied extensively for the NRR.[190-192] We highlight recent advances for both types of catalysts in the following section. A series of precious metals such as Rh, Au, Ru, and Pd,[193-194] nonprecious metals such as Fe, Mo, Zn,[195-197] and carbon-based metal-free materials[192] have been studied for the NRR in alkaline media (Table 6). Several effective strategies, such as strain and/or vacancy engineering, as well as heteroatom doping, have been explored to modify the electronic configuration of catalysts to enhance intrinsic NRR activity. Unfortunately, most of the NRR catalysts still suffer from low ammonia yields, high overpotential, and low Faradaic efficiency induced by the competing HER side reaction.[191] Therefore, a rigorous electrochemical NH_3 synthesis protocol was emphasized for future NRR studies[198] because it is insufficient to document the formation of NH_3 by only reporting NH_3 production rates without reliable confirmative control experiments.

Table 6. Summary of recently reported PGM and PGM-free NRR catalysts in alkaline media.

Catalysts	NH_3 yield rate	Faradaic efficiency (%)	Potential (V *vs.* RHE)	Electrolyte	Ref.
Au nanorod	1.648 μg $h^{-1}cm^{-2}$	4.0	–0.2	0.1 M KOH	[199]
Rh nanosheet	23.88 μg $h^{-1}mg^{-1}$	0.217	–0.2	0.1 M KOH	[200]
$Pd_{0.2}Cu_{0.8}$/RGO	2.8 μg $h^{-1}mg^{-1}$	<1.0	–0.2	0.1 M KOH	[201]
30% Fe_2O_3-CNT	0.65 μg $h^{-1}cm^{-2}$	0.164	–0.2 V *vs.* Ag/AgCl	0.5 M KOH	[202]
Fe_2O_{3-x}/CNT	0.46 μg $h^{-1}cm^{-2}$	6.0	–0.2 V *vs.* Ag/AgCl	0.1 M KOH	[195]
CoP	2.485 μg $h^{-1}mg^{-1}$	7.36	0.0	1.0 M KOH	[203]
Ni-N-C	85.0 μg $h^{-1}cm^{-2}$	11.0	-0.3	0.1 M KOH	[170]
Nano-Fe_2O_3	146.88 μg $h^{-}cm^{-2}$	35	1.2 (at 200ºC)	0.5:0.5 NaOH-KOH	[204]
C-ZIF-1100-1 h	57.8 μg $h^{-1}cm^{-2}$	10.21	-0.3	0.1 M KOH	[205]

4.2.1 PGM Catalysts for the NRR

Nearly all of the PGMs, including Pt, Ru, Au, Pd, and Rh, were studied for the NRR in virtue of their excellent conductivity, high-density of under-coordinated surface atoms, as well as appropriate adsorption of various reactants.[179, 206] They are further divided into three categories: individual metals, binary alloys, and single metal site catalysts.[206] The most popular metal, Pt, is not effective for the NRR due to its overwhelming affinity for the HER. Instead, the typical single metals active for the NRR are Ru, Au, and Pd,[182] and some of them are more active in alkaline media. As a typical example, the tetrahexahedral Au nanorods (Au THH NRs) were employed as a heterogeneous NRR catalyst and measured at room temperature and atmospheric pressure (Figure 12a).[199] Both NH_3 and N_2H_4 are products of the NRR detected by colorimetric methods (Figure 12b), which differs from previous reports.[207] DFT calculations predicted that an alternating hydrogenation mechanism is extremely likely for the NRR. Additionally, the effect of testing temperature on the electrochemical synthesis of NH_3 suggested that high temperature tends

to show a faster reaction rate (Figure 12c). Their thermodynamic calculations indicate that the activation energy of N_2 reduction to NH_3 is about 13.7 kJ mol^{-1} when using this Au THH NR catalyst (in contrast, the industrial Haber-Bosch process requires approximately 335 kJ mol^{-1}). These findings suggest that electrochemical reduction can significantly reduce the difficulty of NH_3 synthesis under ambient conditions. The temperature-dependence of electrosynthesis of NH_3 in an alkaline system further indicates that high-temperature molten hydroxide systems above 200°C seem to be favorable for the NRR.[204] it is significant to find an appropriate electrolyte that can effectively suppress the competing HER to boost the selectivity for the NRR. A recent work has reported a Pd/C NRR catalyst that was evaluated in three different electrolytes of 0.05 M H_2SO_4 (pH = 1.2), 0.1 M PBS (pH = 7.2), and 0.1 M NaOH (pH = 12.9).[208] As shown in Figure 12d, the NH_3 yield rate in PBS is 4.9 μg $mg^{-1}_{Pd}h^{-1}$, which is about two times of that in NaOH (2.1 μg $mg^{-1}_{Pd}h^{-1}$) and in H_2SO_4 (2.5 μg $mg^{-1}_{Pd}h^{-1}$). More strikingly, the FE in PBS (2.4%) is much higher than the others (both <0.1%), clearly indicating the effective suppression of the HER activity in PBS electrolyte. The maximum FE for NH_3 production in PBS reaches to 8.2% at 0.1 V *vs.* RHE, corresponding to a low overpotential of 56 mV. Theoretical calculations indicate the unique activity of Pd originates from its balanced hydrogen evolution activity and the Grotthuss-like hydride transfer mechanism on α-PdH that lowers the free energy barrier of N_2 hydrogenation to $*N_2H$, the rate-limiting step for NH_3 electrosynthesis (Figure 12e). Additionally, the activity and selectivity trends on different single metal catalysts (Pd/C > Au/C > Pt/C) were predicted by using the DFT-calculated free energies of hydrogenation of N_2 *vs.* hydrogen evolution across metal

surfaces (Au, Pt, and α-PdH).

Although engineering the shape and nanostructure of individual metals could alter the exposed facets of metal catalysts, alloying them with other metals could be more effective in modifying their electronic and geometric properties.[147] In particular, binary alloys often generate a synergy between the combined metals, modification of surface electronic states, and optimal coordination number at the surface, therefore yielding a balance between necessary proton supplies and the HER.[179] Bimetallic alloys include Ru-Pt, Pd-Cu, and Au-Ag, were reported as NRR catalysts in alkaline media.[206] As a typical example, the bimetallic PdRu tripod catalyst (PdRu TPs, Figure 12f) has been synthesized through a one-pot route, showing prominent NRR activity in a KOH electrolyte (Figure 12g). The superior NRR activity and stability of the PdRu TPs were mainly due to the unique tripod nano-architecture and bimetallic alloy structure, which could provide an abundance of exposed active sites with optimal adsorption/desorption energies for reactants, intermediates, and products. As a proof-of-concept experiment, PdCu amorphous nanoclusters anchoring on reduced graphene oxide (rGO), which were prepared via a co-reduction method using tannic acid and $NaBH_4$ mixed reductants, were studied as an NRR catalyst (Figure 12h).[201] The optimal $Pd_{0.2}Cu_{0.8}$/rGO composite exhibits a higher NRR activity than that of the monometallic counterparts (Figure 12i). According to an associative NRR mechanism on precious metals,[178, 199] Pd can be utilized as a catalyst for nitrogen fixation due to its relatively balanced hydrogen evolution activity and the Grotthuss-like hydride transfer pathway. However, there exists a stronger binding between Pd and hydrogen adatoms when compared with the nitrogen speices. Therefore,

the covered molecular hydrogen would poison Pd sites. Fortunately, the introduced Cu could accelerate hydrogen desorption from the Cu metal surface. Compared to the individual Pd or Cu, the $Pd_{0.2}Cu_{0.8}$/rGO boasts more facile hydrogen dissociation at Pd atom sites and weaker binding at Cu sites. Therefore, a synergy has been observed on the binary PdCu surface, showing an increased affinity towards the NRR (Figure 12i). Moreover, the addition of rGO supports also improves the dispersion of catalytic sites and facilitates the adsorption of N_2 molecules.

Beyond the metal nanoparticle catalysts mentioned above, single metal sites stabilized by nitrogen and defects in supports have recently emerged for a variety of electrocatalysis processes, including the NRR.[22, 209-210] In particular, different supports, including metal oxides, metals, carbons, and the graphitic nitride (g-C_3N_4), can stabilize single Pt, Au, and Ru sites.[206] Essentially, optimal supports can not only strongly bond single metal sites, but also donate/withdraw electrons to/from metal sites to subsequently modulate adsorption/desorption energies of intermediates during the NRR.[22] Only Ru sites encapsulated in N-doped porous carbon via a coordination-assisted strategy (*i.e.*, the modification by ZrO_2 in the catalyst design) enabled efficient NRR.[184] The Ru catalyst with control of coordinated ligands allows a very high NH_3 yield rate of 3.665 mg_{NH3} $mg^{-1}_{Ru}h^{-1}$ at –0.21 V *vs.* RHE and a maximum FE of 21% at a low overpotential of 170 mV in N_2-saturated 0.1 M HCl solution. Their results were further confirmed by the isotopic labeling measurements using $^{15}N_2$-enriched gas (98% $^{15}N{\equiv}^{15}N$) as the feeding gas. The single Ru sites with oxygen vacancies permit the stabilization of *NNH, destabilization of *H, and enhanced N_2 adsorption. More importantly, the O-vacancy sites in ZrO_2 promote the catalytic activity of single

atoms in the NH_3 production due to the suppression of H adsorption: ΔG (*H): –0.20 eV for $Ru@Zr_{32}O_{63}$, –0.42 eV for $Ru@NC_2$, and –0.47 eV for Ru(0001). Accordingly, the rational design of single-metal site catalysts opens a potentially alternative avenue for efficient NH_3 electrosynthesis.

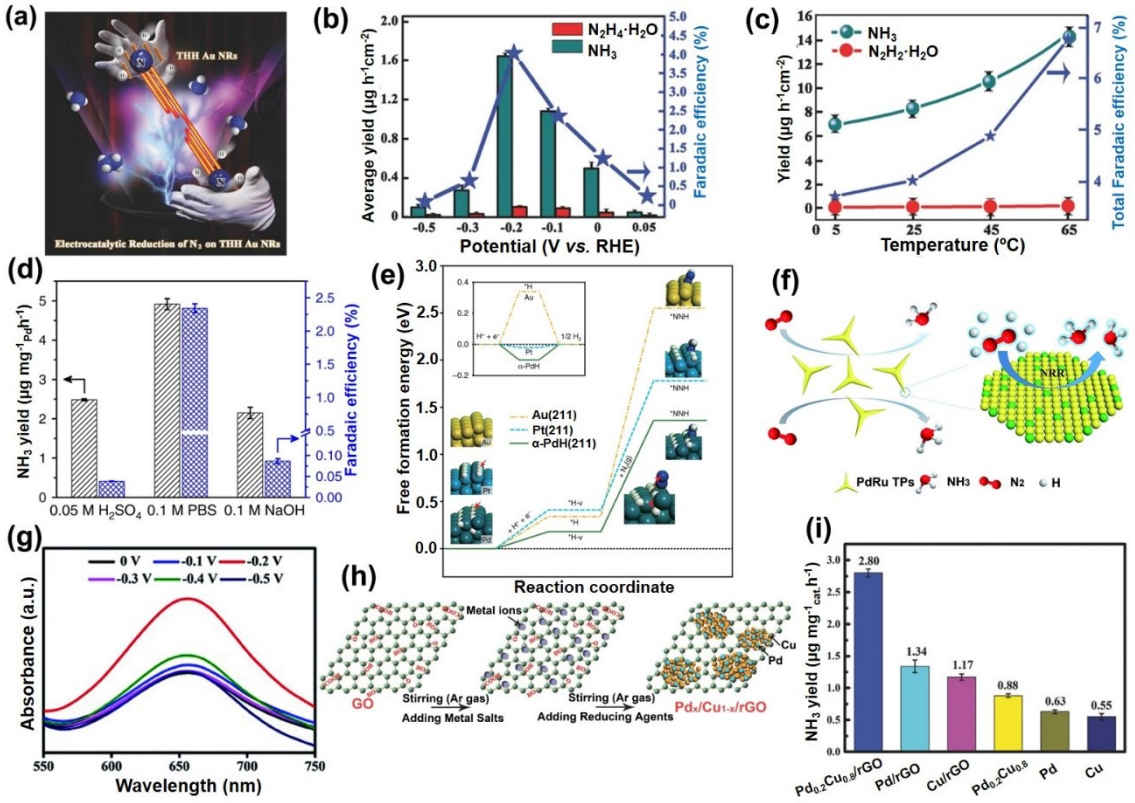

Figure 12. (a) Schematic illustration of Au THH NR used for electrocatalytic reduction of N_2 to NH_3, (b) yield rate of NH_3, $N_2H_4{\cdot}H_2O$ formation, and Faradic efficiency at each given potential, and (c) yield of NH_3, $N_2H_4{\cdot}H_2O$, and Faradic efficiency against catalytic temperature under atmospheric pressure at –0.2 V *vs.* RHE. Reproduced with permission.[199] Copyright 2016, Wiley-VCH. (d) NH_3 yield rates and FE in the three N_2-saturated electrolytes of the Pd/C catalyst on the carbon-paper support measured at –0.05 V *vs.* RHE. (e) DFT-calculated free energy pathways of HER (inset) and the critical steps of N_2RR on the (211) surfaces of Au, Pt, and α-PdH at the surface potential of 0 V *vs.* RHE under 298.15 K (atomic structures shown in the insets).[208] Reproduced with permission. Copyright 2018, The Royal Society of Chemistry. (f) Schematic diagram of the electrocatalytic NRR process on the PdRu TPs, and (g) UV-Vis absorption spectra of KOH electrolytes stained with indophenol indicators after charging for two hours. Reproduced with permission.[206] Copyright 2019, The Royal Society of Chemistry. (h) Schematic illustration of the preparation of Pd_xCu_{1-x}/rGO, and (i) electrocatalytic activities of the bimetallic $Pd_{0.2}Cu_{0.8}/rGO$ composites,

monometallic Pd/rGO and Cu/rGO counterparts, and Pd, Cu single metal for NRR at –0.2 V *vs.* RHE under room temperature and atmospheric pressure. Reproduced with permission.[201] Copyright 2018, Wiley-VCH.

4.2.2 PGM-Free Catalysts for the NRR

Further advancement and widespread utilization for the electrochemical synthesis of NH_3 calls for a significant cost reduction through the use of PGM-free NRR catalysts. Recently, some low-cost and abundant transition-metal oxides (TMOs) such as Cr_2O_3, Mn_3O_4, Fe_3O_4, and Co_3O_4, have been reported as NRR catalysts in acidic and neutral media. However, they are unstable and show a low NRR performance in alkaline media due to the difficulty in the adsorption of protons.[211-212] As considered that alkaline media can suppress the HER and enhance the FE of NRR, it is imperative to identify stable TMO-based catalysts in alkaline solution and develop new and effective methods to achieve a higher FE and NH_3 yield. A MOF-derived hollow C@NiO@Ni microtube is an efficient NRR catalyst in 0.1 M KOH solution, showing a high NH_3 yield of 43.15 μg $mg^{-1}_{cat.}h^{-1}$ and FE of 10.9% at –0.7 V *vs.* RHE (Figure 13a).[211] The main reason for this observed high NRR activity is attributed to the effective proton adsorption by the abundant NiO/Ni interfacial sites. In contrast, the C@Ni sites only contribute to a minimal NRR rate due to a negligible N_2 fixation ability of Ni^0. Besides the catalyst itself, the K^+ ions in the electrolyte can bind with nitrogen and enrich the stern layer interaction with the nitrogen molecules. Therefore, K^+ plays an additional role in increasing nitrogen concentration at the catalyst surface. Moreover, their cycling experiments for ten times at –0.7 V *vs.* RHE on the C@NiO@Ni catalyst show a stable NH_3 yield and FE (Figure 13b), certifying the excellent durability of this catalyst in an alkaline media.

Atomically dispersed single atom-based catalysts have shown tremendous achievements in

the fields of ORR, OER, and CO_2 reduction.[193] Recently, Mo atoms anchored to N-doped porous carbon (SA-Mo/NPC) exhibited reasonably good NRR activity.[213] Due to the optimized abundance of single active sites and 3D porous structure (Figure 13c, d), the SA-Mo/NPC catalyst shows a remarkable FE for NH_3 formation of up to 14.6 ± 1.6% (corresponding to an NH_3 yield rate of 34.0 ± 3.6 μg_{NH_3} h^{-1} $mg_{cat.}^{-1}$) at –0.3 V *vs.* RHE and room temperature (Figure 13e). This work experimentally demonstrated the feasibility of producing NH_3 at ambient conditions by using single Mo active sites in alkaline electrolyte. It can be regarded as a promising catalyst to alleviate the kinetic issues associated with activating the strong N≡N bond, due to the availability of *d*-orbital electrons for the π-back donation process.[182] Unfortunately, the NH_3 yield and FE of these transition metal-based catalysts are still lower, possibly due to unfavorable contact on the metal surfaces, the more preferred formation of metal-H bonds resulting in the adverse HER, and/or structural imperfections leading to low surface area and porosity.

Carbon-based NRR catalysts have also emerged as alternatives to metal-based ones.[192] Our group recently reported a MOF-derived N-doped nanoporous carbon as a metal-free NRR catalyst.[205] The moiety containing carbon vacancies and three pyridinic N atoms embedded into carbon planes (Figure 13f) could act as the active sites, and the adsorption of N_2 is likely the rate-determining step (Figure 13g). Also, the protonation process involved with releasing the second NH_3 molecule has reduced activation energy. These computational results are significant for us to understand the electrocatalytic mechanism of N-doped carbon materials for the NRR. With ample surface area, porous architecture, and abundant active N doping, the optimal C-ZIF-8-1100 catalyst

(Figure 13h) exhibits a respectable production rate of NH_3 with an FE of 10.2% at –0.3 V *vs.* RHE. Unlike conventional NRR catalysts, MOF-derived carbon materials with desirable N doping and carbon defects can provide new insight into the rational design of efficient catalysts for electrosynthesis of NH_3. Furthermore, we recently discovered a new class of atomically dispersed and nitrogen coordinated single NiN_x site catalyst derived from a Ni-doped ZIF-8 precursor.[170] Unlike the NRR inactive Ni cluster, the single Ni site catalyst is active for the NRR in alkaline, acidic, and neutral electrolytes with significantly reduced onset potential (~0 V *vs*. RHE in acids). The catalyst exhibited an optimal NH_3 yield of 115 μg cm^{-2} h^{-1} at –0.8 V vs. RHE under neutral conditions (0.5 M $LiClO_4$). High faradic efficiency achieved 21 ± 1.9% at -0.2 V under alkaline conditions, but the ammonia yield is low. DFT calculations predicted the favorable pathway of NRR using different possible configurations of Ni-N_x-C. They predicted that mixed pathways of both alternative and enzymatic on the Ni-N_3-C10 configuration are most favorable. However, the potential-determining step is hydrogenation. The external energy required is less than that on N-doped carbon that we had reported earlier.[205] This work further supports that single metal site catalysts with appropriate metal centers and nitrogen coordination are very promising for the NRR and indeed improve the scaling relationship of transition metals.

As mentioned before, the electrochemical synthesis of NH_3 could benefit from relatively high temperatures. Although it is more attractive to synthesize NH_3 at room temperature and atmospheric pressure electrochemically, the FE under this condition is far too low for industrial applications and not competitive with the Haber-Bosch process.[204] If moderate reaction

conditions at intermediate temperatures can achieve sufficient catalytic efficiency comparable to the Haber-Bosch process, it would be feasible to implement the electrochemical synthesis of NH_3 in the industry. In 2014, Licht and his coworkers successfully demonstrated the feasibility of NH_3 electrosynthesis *via* N_2 and H_2O by using a nano-Fe_2O_3 catalyst in a molten hydroxide suspension.[204] They first employed a water electrolyzer and achieved a 100% FE at 200ºC. After feeding N_2 into the cathode, the FE of the NH_3 production was very high, reaching up to 35% at 200ºC in a molten hydroxide electrolyte (NaOH: KOH = 1:1 at 1.0 atm) (Figure 13i). Encouraging results obtained from this work strongly suggests that electrochemical strategy will be a promising alternative for NH_3 synthesis in the future.

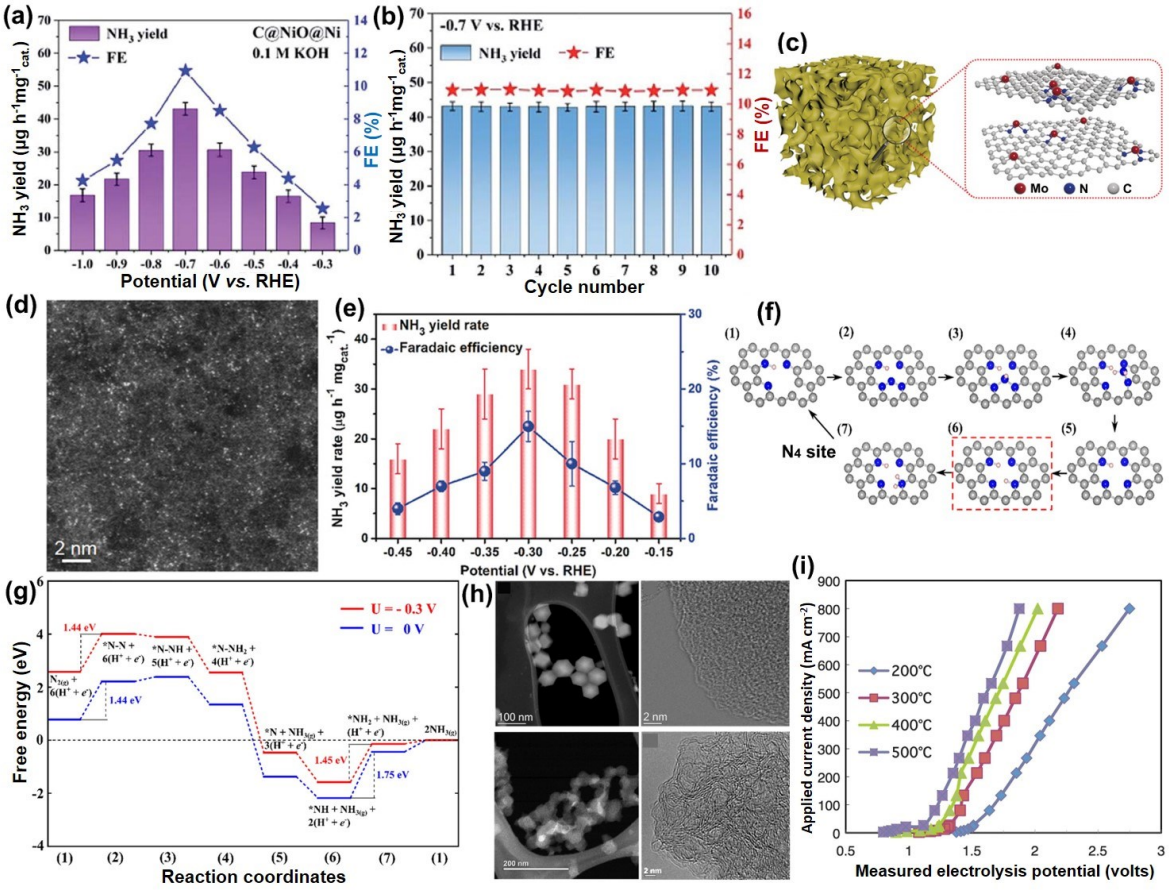

Figure 13. (a) NH_3 yields and Fes of C@NiO@Ni catalyst for NRR at various potentials in N_2-saturated 0.1 M KOH. (b) Durability test for ten times at –0.7 V *vs.* RHE. Reproduced with permission.[211] Copyright 2020, The Royal Society of Chemistry. (c) An illustration of SA-Mo/NPC and its corresponding atomic structure model, (d) atomic-resolution HAADF-STEM image, and (e) NH_3 yield rate and Faradic efficiency at each given potential in 0.1 M KOH. Reproduced with permission.[213] Copyright 2019, Wiley-VCH. (f) Atomic structure scheme presenting the reaction pathway of N_2 reduction on the N_3 sites, (g) predicted free energy evolution of N_2 reduction on N_3 sites in N-doped carbon under electrode potentials of 0 and –0.3 V, and (h) comparison of the morphology and microstructure between ZIF-8 nanocrystal precursors and the corresponding carbon catalysts generated through one-step thermal activation at 1100ºC under N_2 atmosphere for one hour. Reproduced with permission.[205] Copyright 2018, Elsevier. (i) The measured electrolysis potential at 200ºC of a molar molten mix of 0.5 NaOH/0.5 KOH at 1 atmosphere between two 2.5- by 1.5-cm planar nickel electrodes. Reproduced with permission.[204] Copyright 2014, AAAS.

An issue affecting these nitrogen-containing PGM-free catalysts is the uncertainty of the sources of measured NH_3 due to the likely loss of N from catalysts during the NRR. Also, NH_3 is

ubiquitous in the laboratory environment, being found as contaminations in chemicals and gases, finding general use in most labs, and even found naturally in the atmosphere in different areas and seasons. The challenge then is to provide sufficient proof that the NH_3 determined was produced from electrochemical NRR and not from other exogenous sources. The accuracy of the reported data in the literature is always questionable, which is a significant constraint in seeking highly active NRR catalysts. Ideally, control experiments by using ^{15}N-labelled gas to eliminate contaminant sources of NH_3 is imperative, helping to avoid some false-positive interferences from other N species. However, the proposed quantitative ^{15}N tests combined with NMR is high-priced and time-consuming, which is not easily accessible for most research groups. However, rigorous electrochemical NH_3 synthesis protocols are necessary to justify the catalyst activity, a key strategy used to demystify synthesis-structure-property relationships. Recent critical references by Ib Chorkendorff [198] and MacFarlane[178] provide reliable experimental protocols for NRR research in the field.

4.3 AEM-Based MEAs for NH_3 Electrosynthesis

Current AEM-based electrolyzers for NH_3 electrosynthesis operates at low- (< 100ºC) and intermediate-temperature (100–300ºC) systems. In general, the cathodic reaction in alkaline electrolyte directly combines N_2 with H_2O and electrons to form NH_3 ($N_2 + 3H_2O + 6e^- = 2NH_3 + 6OH^-$). The produced OH^- ions can pass through an AEM toward the anode side and oxidize to O_2 ($4OH^- - 4e^- = 2H_2O + O_2$) (Figure 14a). Catalyst coated gas diffusion layers (GDLs) act as electrodes and assemble with the AEM for fabricating MEAs. Currently, only a few works

introduced AEM electrolytes used for NH_3 electrosynthesis. In a typical example, an MEA is made from the γ-Fe_2O_3 layered on carbon paper as the cathode and IrO_2 layered on titanium paper substrates as the anode.[189] The gaseous NRR at the γ-Fe_2O_3 NP electrode could generate NH_3 at cell voltages higher than 1.5 V_{cell} (Figure 14b). However, the maximum FE of MEA (0.044%) is significantly lower than that tested in the alkaline electrolyte (1.96%). This difference can be rationally explained by the porous membrane electrode that vastly enlarges (up to 40 times) the HER current compared to the disk electrode and the eclipsing of the formation selectivity of NH_3. As above-mentioned in an RDE level, the electrosynthesis of NH_3 shows a temperature-dependent effect in alkaline media. A higher operating temperature favors the NRR process. A recent MEA level report further confirmed this phenomenon.[204] Further elevating the operating temperature (105–200ºC) in a molten hydroxide electrolyte cell with a nano-Fe_2O_3 NRR catalyst can realize a high FE of 35% (Figure 14c).[204] More importantly, promising stability, with 85% retention of the initial efficiency for NH_3 production, was achieved after a 6-hour stability test at 200ºC in a molten NaOH-KOH electrolyte. Better mixing and excess nitrogen and water vapor could significantly stabilize the rate, as can be demonstrated by the NH_3 production fell only 3% over the first six hours when the water-saturated nitrogen increased from 4 to 111 mL min^{-1}. Although there is no long-term stability test, this work provided a proof-of-concept that the AEM electrolyzer technology is promising for sustainable NH_3 production under ambient conditions as a replacement of the energy-intensive Haber-Bosch process.[189] In another work, Renner *et al*. developed a well-built AEM-based system,[189] which employed Fe, Ni, and Fe-Ni materials as the cathodic NRR

catalysts (Figure 14d). When the MEA operates at a moderate temperature of 50ºC and under atmospheric pressure, the initial FE is up to 41% by using a Fe catalyst, further highlighting the feasibility of using AEM technology for NH_3 electrosynthesis. However, the challenge is that this efficiency is short-lived, and decreases to single-digit FE in a matter of hours. Therefore, further material improvements, including AEMs and NRR catalysts along with the optimization of cell design, are desperately needed for advanced electrolyzers to produce NH_3 *via* H_2O and N_2 under ambient conditions.

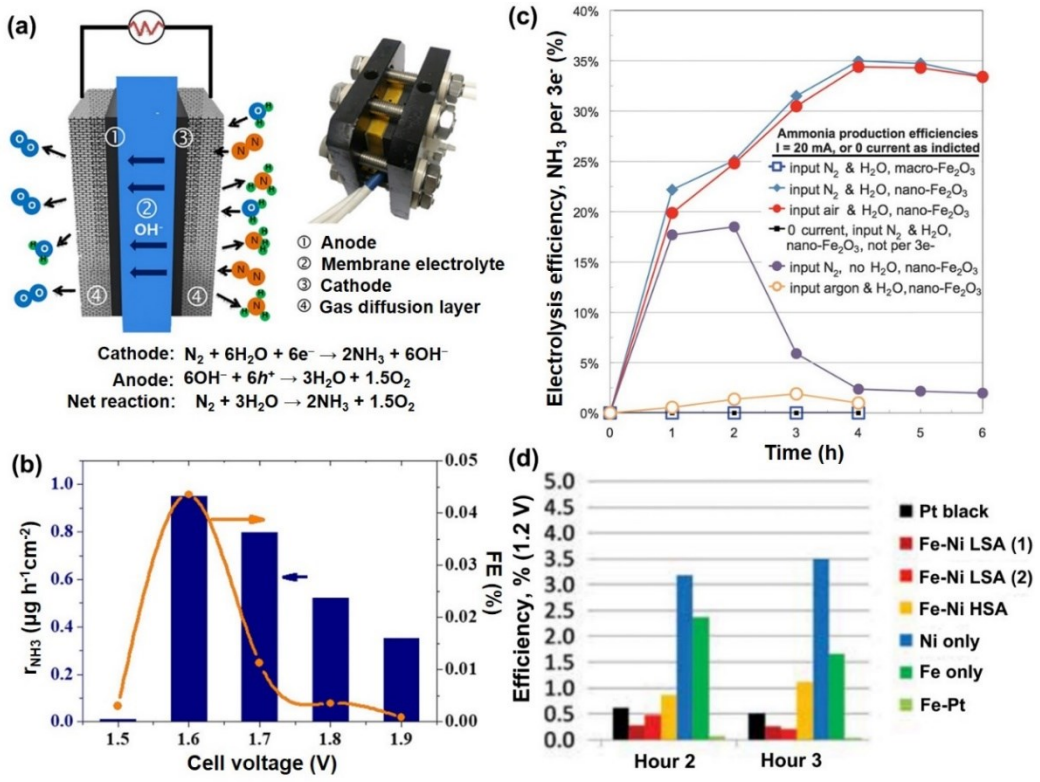

Figure 14. (a) Schematic of electrochemical synthesis of NH_3 in an AEM-based electrolyzer, and the corresponding photographic image of the actual device, and (b) NH_3 formation reaction rate and FE determined from the CA measurements of the device. Reproduced with permission.[202] Copyright 2017, American Chemical Society. (c) The efficiency of the current conversion of NH_3 product. Experimental quantification of NH_3 from air or N_2, either saturated with water or dry, by one-pot synthesis. Nano- or micron-sized Fe_2O_3 as the NRR catalysts tested at 200ºC.

Reproduced with permission.[204] Copyright 2014, AAAS. (d) Using different NRR catalysts for NH_3 synthesis and associated NH_3 production efficiency results from the AEM electrolyzer test cell. Reproduced with permission.[189] Copyright 2015, ECS.

5. The AOR for Direct Ammonia Fuel Cells

In addition to clean hydrogen, current fuel cells use a variety of hydrocarbon fuels in molten carbonate, solid oxide fuel cells (SOFCs, operating at 400–800ºC),[214-215] and direct methanol fuel cells (operating at 60–100ºC).[193] However, they often generate CO_2 as part of the oxidation of the carbon-containing fuel, which requires the overall fuel cell process to be CO_2-neutral.[216] In the quest for sustainable fuel alternatives, NH_3, with its low production cost,[217] high energy density, and high hydrogen storage capacity have recently attracted significant interest.[218] In principle, ammonia can be utilized to power fuel cells either by thermal decomposition to H_2 or directly using as the fuel in DAFCs.[219] The development of DAFCs was from the 1960s,[220] which produced a maximum current density of 40 mA cm^{-2} below 150ºC and 120-130 mA cm^{-2} above 200ºC at a cell voltage of 0.4 V.[220] Instead of acidic PEM, AEM is often employed in DAFCs to avoid NH_3 poisoning effects on the membrane electrolyte.[216, 221] DAFCs are capable of operating at both low temperature (< 100ºC)[222] and intermediate temperature (100ºC < T < 500ºC)[223] using molten hydroxide alkaline electrolytes. Table 7 summarizes the targeted standards for a DAFC, which aims to achieve a competitive performance to PEMFC and SOFC technologies. Besides, alkaline environments in DAFCs offer the opportunity to use PGM-free cathode catalysts. Despite these apparent advantages, the development of DAFCs in the past few decades has been slower than other FCs, mainly due to the absence of highly efficient and stable catalysts for the slow AOR

process.

Table 7. Targeted standards for a DAFC technology.[a]

Specification	DAFCs	Units	Notes
Current density	0.6	A cm^{-2}	Reference voltage: 0.6 V
Efficiency	>60	%	Fuel: anhydrous NH_3
Desired temperature	150–350	ºC	
Estimated fuel consumption	5.28	kWh kg^{-1}	
Fuel cost	0.25	\$ kg^{-1}	
Expected lifespan	10	years	
Capital expenditure	2M	\$ MW^{-1}	

[a]Data source: 2017 U.S. advanced research projects agency-energy (ARPA-E) project targets.[30, 224]

5.1 Understanding of AOR Mechanism

To elucidate the possible reaction pathway during the AOR from NH_3 to N_2, several groups have carried out computational calculations and simulations.[225-228] The most popular catalysts used for modeling are Pt and Pt-based alloys, and other systems are rare because they likely display insufficient activity towards the AOR. The AOR is a 6-electron reaction process ($2NH_3 + 6OH^- = N_2 + 6H_2O + 6e^-$, $E^0 = –0.77$ V *vs.* SHE) which produces N_2 and H_2O.[227] A dimerization step without electron transfer for the N≡N bond formation is the generally accepted scheme,

$$*NH_x + *NH_y = H_xN – *NH_y \quad (13)$$

where *x* and *y* could be 0, 1, and 2; * indicates an adsorbed reaction intermediate. All deprotonation steps before and after dimerization involve single electron transfer, i.e.,

$$*NH_x + OH^- = *NH_{x-1} + H_2O + e^- \quad (14)$$

or

$$*N_2H_{(x+y)} + OH^- = *N_2H_{(x+y-1)} + H_2O + e^-. \quad (15)$$

Therefore, the reaction pathways depend on the values of *x* and *y*. In the 1960s, Oswin and Salomon proposed a successive dehydrogenation mechanism, in which NH_3 consecutively dehydrogenates to adsorbed *N, and then through an *N–*N or N_2 dimerization pathway to form N_2.[226] Later in the 1970s, the $*NH_x + *NH_y$ (*x* and *y* = 1 or 2) dimerization pathways were suggested by Gerischer and Mauerer.[225]

The adsorption energies of possible reaction intermediates were calculated by Daramola and Botte[229-230] on the Pt(111) facet, generating a trend ($N_2 < H_2O < NH_3 < N_2H_2 < N_2H_4 < N_2H < N_2H_3 < OH < NH_2 < NH < N$). In 2015, a DFT study by Herron, Ferrin, and Mavrikakis examined the catalytic AOR at close-packed surfaces of other models, including Au, Ag, Cu, Pd, Pt, Ni, Ir, Co, Rh, Ru, Os, and Re.[227] According to Sabatier analysis, Gerischer-Mauerer's mechanism[225] is kinetically favorable at Pt and Ir surfaces, whereas other metal surfaces showed relatively lower activity.[227] It is important to note that the inactive intermediate of *N can poison the catalyst surface, following the conclusions reported by experiments.[21, 231-232] Another important study by Novell-Leruth and co-workers indicated that NH_3 and the intermediate $*NH_2$ were more stable on Pt(100) than on Pt(111), suggesting structure sensitivity for the AOR process at the Pt surface.[233] They also predicted that the most probable adsorption configurations are different for various intermediates such as top sites for NH_3, bridge sites for $*NH_2$, and hollow sites for *NH and *N on Rh, Pd, and Pt.[234] A recent study[235] by Estejab and Botte reported theoretical calculations for NH_3 oxidation on bimetallic Pt-Ir catalysts, suggesting that the kinetics of AOR on Pt occurs via

the N_2H_4 mechanism. At the same time, AOR on Ir follows the N_2 mechanism. The addition of Ir to Pt could modify the electronic effect of the catalyst and allow NH_3 oxidation to occur at a reduced overpotential. Due to the intrinsic complexity of solid-electrolyte interfaces, the rapid deactivation of Pt nano-catalyst for the AOR remains largely unexplained. Recently, Xin et al., predicted that the dehydrogenation of $*NH_2$ is the potential determining step on Pt(100). The *OH species, thermodynamically stable at >0.5 V, plays a significant role in boosting kinetics via preferential stabilization of *NH through hydrogen bonding.[236] At the high operation potentials (>0.63 V *vs.* RHE), when the *NH dehydrogenation to *N becomes thermodynamically favorable, surface deactivation occurs. However, the dimerization of *N with *N or *NH is kinetically facile, implying that the adsorbed *N is only the precursor to poisoning species (*e.g.*, *NO) on Pt(100) surface. The mechanistic insights provided by this work are different from previous reports, offering new strategies for the rational design and synthesis of active, selective, and robust electrocatalysts for the AOR. Although mechanisms have been studied to provide fundamental understandings on AOR process, experimental development of binary and ternary metallic AOR catalysts with enhanced activity and stability is still in the early stage.

5.2 Development of AOR Catalysts in Alkaline Electrolytes

Besides theoretical understanding of AOR mechanisms, many experimental studies exploring effective catalysts have been reported in recent years,[232, 237] with the majority of studies so far being Pt-based, which showed promise to generate high current density at relatively low overpotential.[238-239] Nevertheless, high loadings of Pt are usually required to obtain acceptable

reaction rates for the sluggish AOR. Alternatively, searching for PGM-free catalysts is again highly desirable, some examples of which are metal oxides (e.g., $Ni/Ni(OH)_2$),[218] metal alloys (e.g., Ni-Cu),[240-241] and boron-doped diamond.[242] However, these PGM-free materials suffer from extremely high overpotentials (typically > 1.0 V), much larger than those measured with PGM-based ones (~0.3-0.5 V),[243] and low current densities, not to mention elusive reaction mechanisms.[30, 244] Therefore, the most promising AOR catalysts for DAFCs are still PGM-based ones. Typical PGM catalysts include single, bi-, and tri-metallic alloys, which are summarized in Table 8 to compare their intrinsic activity (onset potential) and reaction rates (peak current density). In this section, we highlight the most promising PGM-based catalysts for DAFCs.

Table 8. AOR activity comparison of single, bimetallic, and trimetallic PGM catalysts.

Samples	Onset potential (V *vs.* RHE)	Current density (A g^{-1}) at 0.5 V *vs.* RHE	Peak current density (A g^{-1})	Ref.
CeO_2-modified Pt	~0.50	–	–	[232]
Pt/SiO_2-CNT	4.84	–	77.3	[245]
Pt-decorated Ni particles	~0.50	–	75.3	[246]
Pt_5Ir_5/SiO_2-CNT	0.369	22.9	66.3	[245]
PtIr/CNT (Pt:Ir = 4:1)	~0.38	–	–	[247]
PtIr/N-rGO (Pt:Ir = 1:3)	~0.37	–	–	[248]
PtRh/C (Pt:Rh = 9:1)	~0.44	9.0	93.8	[239]
$PtIrNi_1$/CeO_2-CNT (Pt:Ir = 9:1)	0.465	5.4	34.0	[245]
PtIrZn (Pt:Ir = 8:2)	~0.30	–	–	[249]
$PtIrNi_1$/SiO_2-CNT (Pt:Ir = 9:1)	0.399	13.2	124.0	[245]
CuPtRu (Pt:Ru = 7:1)	~0.49	10.0	180.0	[250]
$PtIrNi_1$/XC-72 (Pt:Ir = 9:1)	0.428	8.6	46.7	[245]

5.2.1 Pt Catalysts for the AOR

Effective tactics to enhance activity on Pt are crystal face regulation, surface optimization, and oxophilic metal oxide modification.[232, 251-252] The AOR is a structure-sensitive process as illuminated in Figure 15a, which has shown a well-defined single oxidation peak on Pt(100) and negligible oxidation peaks on Pt(110) and Pt(111).[251] The Pt(100) basal plane can exhibit the highest intrinsic activity. Still, this surface configuration is unstable between the hydrogen evolution and the oxide formation regions, resulting in unsuitability for long-term utilization.[237] It would be ideal for designing a catalytic surface with high activity and resistance to restructuring over a wide range of potentials. The electrochemically roughened Pt electrode (P_R, Figure 15b) developed by MacFarlane's group[252] showed enhanced AOR activity relative to the polycrystalline Pt surface (Pt_{PC}) and electrodeposited Pt black surface (Pt_B) (Figure 15c). Regarding the poisoning effect, they did not provide an in-depth investigation but anticipated that the increased proportion of the stable phase on Pt_R surfaces could mitigate the poisoning issue.[37]

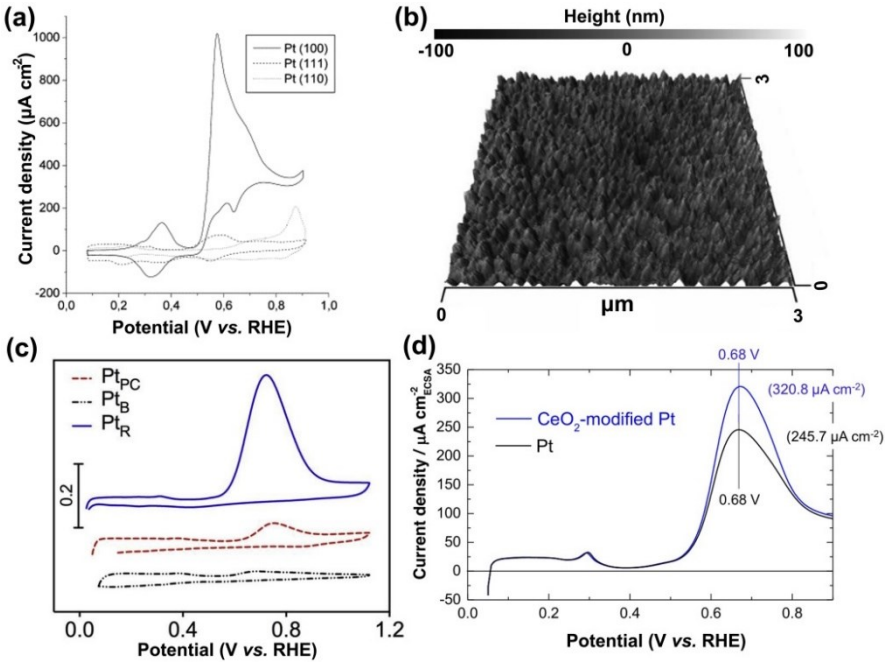

Figure 15. (a) CVs of Pt(100), Pt(111) and Pt(110) electrodes in 0.1 M NaOH + 10^{-3} M NH_3, scan rate 50 mV s^{-1}. Reproduced with permission.[251] Copyright 2003, Elsevier. (b, c) AFM image of Pt_R surface at 3 μm scale and CVs for Pt_R, $Pt_{PC,}$ and Pt_B in the presence of 20 mM NH_3 in 0.1 M KOH electrolyte solution at a scan rate of 10 mV s^{-1}. Reproduced with permission.[252] Copyright 2019, Elsevier. (d) LSVs of Pt disk and CeO_2-modified Pt disk electrodes in 1.0 M KOH + 0.1 M NH_3 with a scan rate of 20 mV s^{-1}, including peak current value in parentheses. Reproduced with permission.[237] Copyright 2016, American Chemical Society.

A variety of Pt nanostructures such as dendritic-, flower- and sheet-like structures demonstrated enhanced mass activities of the AOR relative to smooth spherical Pt nanoparticles due to increased electroactive surface areas.[253-255] In principle, promoting selective adsorption of the *OH species is responsible for the enhanced AOR activity, because the *OH species near a catalytic site participate in the reaction and facilitate the AOR.[256] Based on mechanistic understanding, the addition of oxophilic oxide of CeO_2 in Pt catalysts can supply *OH to the active metal surface to facilitate the AOR and other oxidation.[232, 257] Experimentally, the current density on the CeO_2-modified Pt electrode is increased compared to Pt catalysts (Figure 15d). Other metal oxides, such as Y_2O_3, LaO_3, $Sm_2O_{3,}$ and NiO, play a similar role in promoting the AOR activity of

Pt.[256, 258] Overall, facet control and addition of oxides for Pt catalysts possess great promise in enhancing AOR activity, further reducing overpotentials and mitigating poisoning on Pt catalysts.

5.2.2 PtM Alloy Catalysts for the AOR

Insufficient catalytic activity and the high cost of Pt motivates researchers to search for new ways to design advanced AOR catalysts. PtM alloys are currently the most effective AOR catalysts and have exhibited promising performance.[238] Alloying Pt with other metals also generates significant benefits for improving the AOR,[249, 259-260] due to electronic structure change (increase in Pt *d*-electron vacancies), geometric transformation (decrease in the Pt-Pt bond distance), and mitigating surface segregation. Currently, a variety of bimetallic PtM alloys includes Pt-Ir,[21, 231] Pt-Ru,[261] Pt-Pd,[262] Pt-Rh,[239] Pt-Ni,[263] Pt-Cu[264] and Pt-Au,[265] as well as ternary Pt alloys such as Pt-Ir-Rh,[111] Pt-Ir-Zn,[249] Pt-Pd-Rh[266], Pt-Ir-Ni,[245] and Pt-Cu-Ru.[267]

Among these secondary or third metals alloying with Pt, Ir was first identified experimentally as being active, due to its capability to bind NH_3 strongly and lower AOR onset potentials.[268] Pt-Ir alloy catalysts are the benchmark for AOR catalysis.[21] Similar to Pt, the intrinsic AOR activity of bimetallic Pt catalysts are mainly dependent on structures, compositions, and supports (Figure 16). For example, PtIr nanocubes (Figure 16b) show better AOR activity than dendrite-like PtIr NPs (Figure 16a), further suggesting that AOR is a structure-dependent reaction (Figure 16c). Also, the temperature-dependence of the AOR has been reported based on the Pt, Ir, and Pt-Ir alloy catalysts.[21] An increase in temperatures from 25 to 60ºC leads to a dramatic reduction of the onset potential of AOR and a noticeable rise in the peak current density (Figure 16d). These results

indicate that, when operating at high temperatures, DAFC with PtIr catalysts can significantly reduce anodic AOR overpotential and generate high energy efficiency. Besides operating temperature, AOR activities increased with the increasing NH_3 concentration, as demonstrated by our recent study[245] on both $PtIrNi_1/SiO_2$-CNTs and commercial PtIr/C catalysts (Figure 16e). Besides, the interfaces between active metal sites and advanced support are essential for enhanced electrocatalytic activity. With a rational catalyst design, a ternary PtIrNi alloy deposited on SiO_2-CNT composite support was prepared via a facile sonochemical-assisted synthesis method. The interfaces between SiO_2 and PtIrNi are proportional to the AOR activity. More extensive interfaces in the catalyst generate a better AOR activity. Because AOR reaction sites are the interfaces of SiO_2 and PtIrNi (Figure 16f), in which supplies OH^- from SiO_2 to the metals. Additionally, the interfaces between PtIrNi and CNTs are the main contributors to electron transfer. More significantly, we found that with the addition of Ni to the PtIr surface and/or subsurface, the group *d*-orbital of the density of states shifts up in energy, strengthening the adsorption of *NH intermediates and subsequently enhancing AOR activity. Beyond Pt-Ir alloys, other PtM alloys (*e.g.*, M = Ru, Rh, and Pd)[269-270] also exhibited increased AOR activity compared to Pt, but the relevant mechanisms are not yet precise. For the AOR, an ideal half-reaction in alkaline solution would result in $3e^-$ per N atom and produce only N_2.[271] However, this reaction actually involves various intermediates (or N species), and generally provides many different products such as N_2, NO, and N_2O, and even NH_3.[272] Therefore, the selective oxidation of NH_3 to pure N_2 via active AOR catalysts remains a challenge. Advanced *in-situ*/*ex-situ* characterization to determine

structures and compositions of PtM alloys (*e.g.*, HADD-STEM and XANES) and reaction intermediates could provide ideal model systems for DFT calculations, which is extremely useful in obtaining knowledge for AOR catalysis.

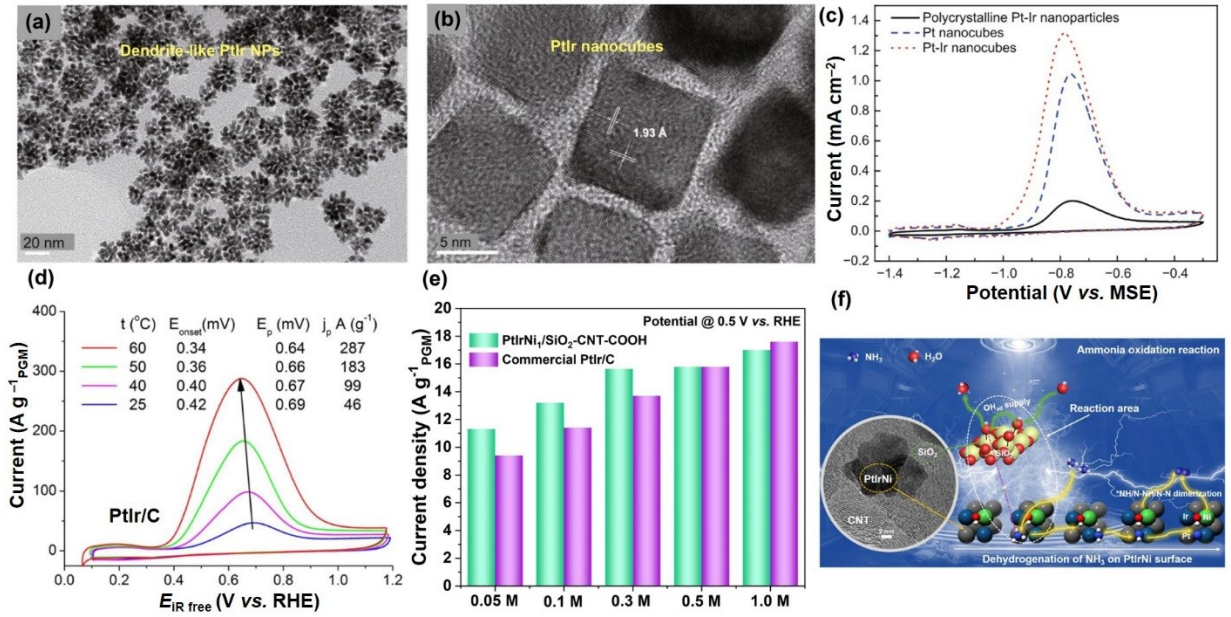

Figure 16. TEM images of dendrite-like PtIr NPs (a) and PtIr nanocubes (b), CVs of Pt-Ir nanocubes, polycrystalline Pt-Ir NPs, and Pt nanocubes, respectively, in 1.0 M KOH + 0.1 M NH_3 solution at 10 mV s^{-1} (c). Reproduced with permission,[237] Copyright 2014, Science China Press, and Springer-Verlag Berlin Heidelberg. CV curves for PtIr/C in Ar-NH_3-vapor-saturated 1.0 M KOH at 20 mV s^{-1}. The last potential cycle taken at each temperature measured with temperature elevated from 25 to 60ºC (d). Reproduced with permission.[21] Copyright 2018, ECS. (e) AOR activity comparison for $PtIrNi_1/SiO_2$-CNT-COOH and commercial PtIr/C in the presence of different NH_3 concentrations at 0.5 V *vs.* RHE, and (d) the key role of interfaces between SiO_2 and PtIrNi for the dehydrogenation of NH_3. Reproduced with permission,[245] Copyright 2020, American Chemical Society.

5.3 MEA performance of Pt-based AOR Catalyst in DAFCs

An economic analysis by carbon-neutral pathways certifies that NH_3 delivers the lowest source-to-tank energy cost by a significant margin among carbon-neutral fuels produced from renewable electricity. Currently, only a few works have studied AOR catalysts at an MEA level for possible

DAFC applications.[223, 273-274] In a typical DAFC (Figure 17a), NH_3 reacts with OH^- and is oxidized at the anode to provide electrons and generate N_2 ($2NH_3 + 6OH^- = N_2 + 6H_2O + 6e^-$, E^0 = –0.77 V *vs.* SHE). At the cathode, O_2 is reduced to consume electrons and generate OH^- ($O_2 + 2H_2O + 4e^- = 4OH^-$, E^0=0.401 V *vs*. SHE). The full reaction generates a theoretical open cell voltage of 1.17 V. However, the overall performance of current DAFCs is still weak. Low power density primarily due to NH_3 crossover, insufficient AOR anodes, and the poisoning of PGM cathodes all holding DAFCs back from being viable. Current DAFCs can use a low-temperature polymer-based AEM electrolyte (< 100ºC) that leads to a low reaction rate and challenging water and heat management. Alternatively, a high-temperature solid oxide electrolyte (>750ºC)-based DAFC usually yields high energy efficiency but imposes a longer starting time and severe thermal material degradation.[275] Nevertheless, the alkaline-based DAFCs can operate at intermediate temperatures (*e.g.*, < 500ºC) by using single or mixed molten hydroxide (*e.g.*, KOH, LiOH, and NaOH) to replace liquid bases. A typical DAFC setup system designed by Ganley uses porous Ni as both the anodic and cathodic catalyst[223] and a KOH-NaOH eutectic mixture as the electrolyte. A maximum power density of approximately 40 mW cm^{-2} at 450ºC (Figure 17b) was obtained when feeding pure NH_3 to the anode and compressed air to the cathode. Recently Eguchi's group at Kyoto University contributed significantly to cell-level studies for DAFC devices.[273] A low-temperature (operating at 50ºC) AEM-based DAFC system evaluated different AOR catalysts. As shown in Figure 17c, voltages of the DAFC with a Pt/C anode drop very rapidly from 1.0 to 0.4 V only after 5 min of operation, which has been ascribed in part to the NH_3 crossover from anode to

the cathode side through the AEM.[273] Another study on DAFCs at an intermediate temperature of 200-220ºC used Pt as both the anode and cathode in a molten KOH-NaOH electrolyte.[274] This DAFC can increase the peak power density from 10.5 to 16 mW cm^{-2} when the operating temperature was increased slightly from 200 to 220ºC (Figure 17d), further verifying the temperature-dependence of AOR in DAFCs.

In addition to the AOR catalysts, the challenging ammonia crossover in DAFCs is inevitable for ionic exchange membrane fuel cells and causes a drop in cell efficiency and power. The Pt/C ORR catalyst at the cathode often is poisoned by the chemisorbed AOR intermediates. Yan and his coworker at the University of Delaware achieved a critically important milestone in DAFC development to mitigate this issue.[222] They developed a high-temperature-stable PAP membrane as a capable AEM that enables operation at 80ºC. Also, the ammonia-tolerant catalyst of Acta 4020 (3.5 wt% transition metal on carbon support) is the cathode catalyst. The benchmark AOR catalyst is commercially available PtIr/C (Pt-Ir = 1:1, 40 wt%) as the anode catalyst. They achieved a record peak power density of 135 mW cm^{-2} at 80ºC in 3.0 M KOH at a current density of 500 mA cm^{-2} (Figure 17e). Several essential strategies for the improvement of DAFC performance are suggested, including water management by controlling water flow, improving AEM to minimize the crossover of ammonia while maintaining OH^- conductivity, and optimization of MEA structures.

Overall, current DAFC performance is still much lower than hydrogen PEMFCs. However, recent successes to fabricate DAFCs by leveraging newly developed AEM electrolytes along with

PtIr/C catalysts and PGM-free ORR cathodes provide an excellent opportunity to use NH_3 directly as a carbon-free fuel to generate power for energy applications.[273-274, 276-277] Many issues of DAFCs, such as the NH_3 crossover effect, poor electrolyte/electrode interfaces, and lack of highly active and stable AOR catalysts, still need to be addressed more thoroughly in the future, which can pave the way for the development of this attractive, clean energy technology.

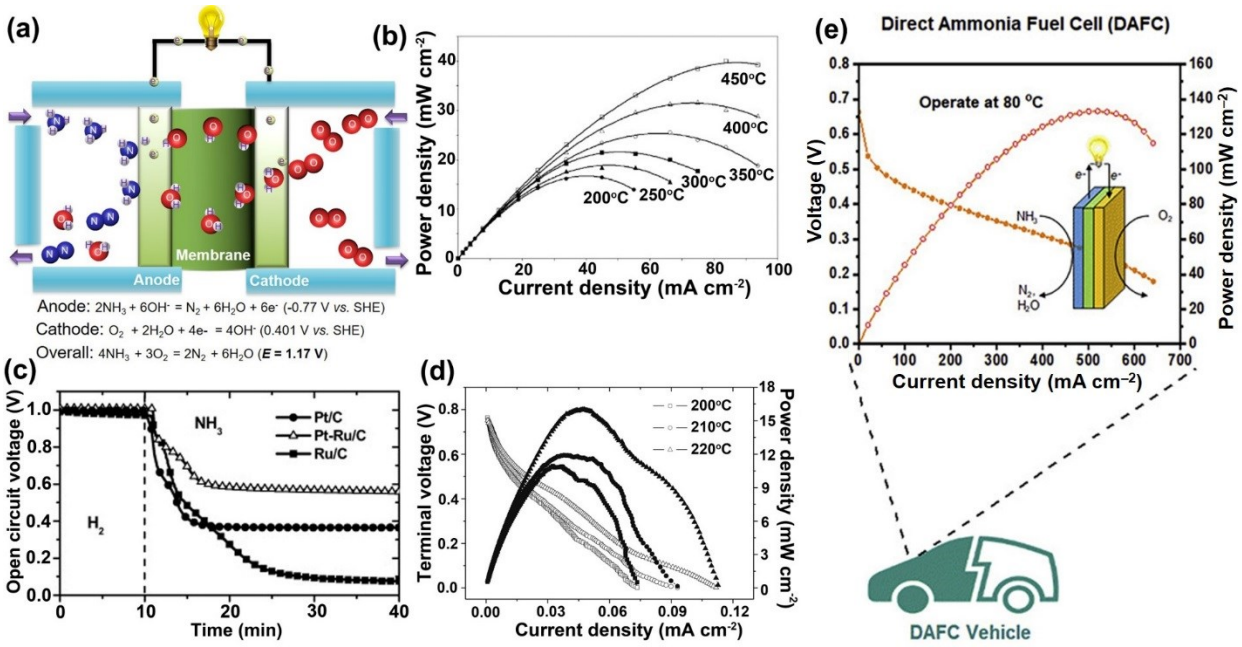

Figure 17. (a) Scheme of a DAFC. (b) power production of performance of a molten hydroxide-based DAFC operating at different temperatures. Reproduced with permission.[223] Copyright 2008, Elsevier. (c) Time course of OCV for AEM-DAFC using different Pt-based AOR catalysts as the anodes. Operating temperature: 50ºC; anode gas: H_2 or NH_3 (humidified at 50ºC); cathode gas: O_2-N_2 (humidified at 50ºC). Reproduced with permission.[273] Copyright 2012, Elsevier. (d) Cell voltage (hollow) and power density (solid) as a function of current density for DAFC using Pt as the anodic and cathodic catalysts, molten KOH-NaOH as the electrolyte, and O_2 (97%)-H_2O (3%) to supply the cathode. Reproduced with permission.[274] Copyright 2014, Elsevier. (e) Polarization and power density curves of DAFCs with Acta 4020 catalyzed cathode and PtIr/C anode. Hydroxide exchange membrane: PAP-TP (10 mm thickness). Test conditions: cell temperature of 80ºC, 3.0 M NH_3 in 3.0 M KOH solution (4.0 mL min^{-1}), O_2 (200 mL min^{-1}) at ambient pressure. Reproduced with permission.[222] Copyright 2019, Cell Press.

6. Summary and Perspective

In this review, we summarized recent advances in developing innovative electrocatalysis for clean energy conversion via electrochemical reactions associated with the water (*i.e.*, OER, and ORR) and nitrogen (*i.e.*, NRR and AOR) cycles. As illuminated in **Figure 18,** pursuing sustainable clean energy technologies via earth-abundant water and nitrogen is feasible and very promising as the complete solution for addressing energy and environmental issues. Due to the success of proton exchange membranes, we highlighted OER and ORR catalysts in acidic electrolytes for their applications in acidic PEM electrolyzers and fuel cells, respectively. The perspectives of NRR and AOR catalyst development in more desirable alkaline electrolytes hold great promise for potential applications in the electrosynthesis of ammonia and the subsequent ammonia utilization in DAFCs for energy generation. We present the inherent connections between these electrocatalysis-related renewable energy technologies to provide a cradle-to-gate assessment of water and nitrogen cycles.

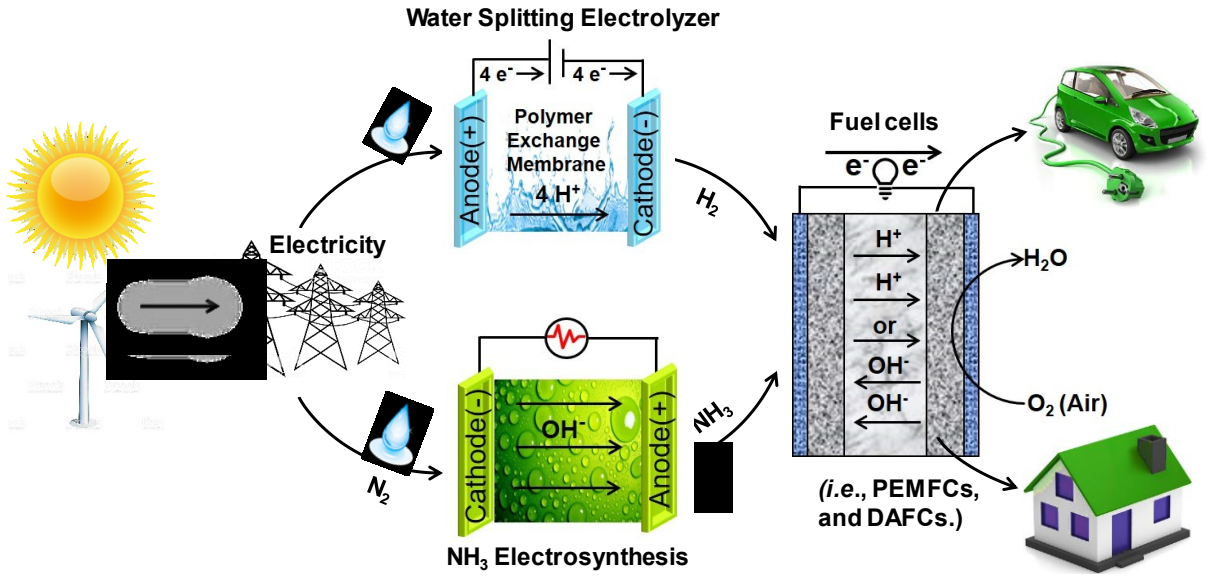

Figure 18. Schematic illumination of integrated water and nitrogen reactions for energy and environmental sustainability: the electrolytic splitting of water and electrochemical NH_3 synthesis using renewable electricity to

generate hydrogen and ammonia for sustainable energy applications via advanced fuel cell technologies.

Catalysts for each reaction are at the heart of the corresponding electrochemical energy technologies. In the water cycle, when using PEM electrolyzers for water splitting to generate hydrogen, the OER anode is still the main limiting factor because it consumes most of the electrical energy and requires a large number of precious metals. In PEM fuel cells that generate electricity by using hydrogen, performance is mostly dependent on the ORR at the cathode due to sluggish kinetics and stability challenges. As for the carbon-free nitrogen cycle, highly active and selective NRR catalysts are the critical component for the electrosynthesis of ammonia with sufficient production rates and FE. To overcome the hydrogen storage and transportation challenges, direct using ammonia in DAFCs for electricity generation is desirable, but is limited mainly by the sluggish AOR at the anode. These electrochemical reactions share a similar feature, *i.e.*, sluggish kinetics, which is primarily due to challenging O=O or N≡N bond breaking/formation associated with multiple electron transfer and a variety of intermediates during these reactions. Advanced catalysts are crucial for facilitating reaction activity, selectivity, and stability in terms of PGM and PGM-free categories. In this review, we provide a comprehensive overview of these key electrocatalysis processes from the theoretical understanding of reaction mechanisms, catalyst design and synthesis, and device performance.

Rational design principles and synthetic techniques are crucial for developing advanced electrocatalysts, including the PGM and PGM-free catalysts, to improve performance and reduce cost, as outlined in Figure 19.

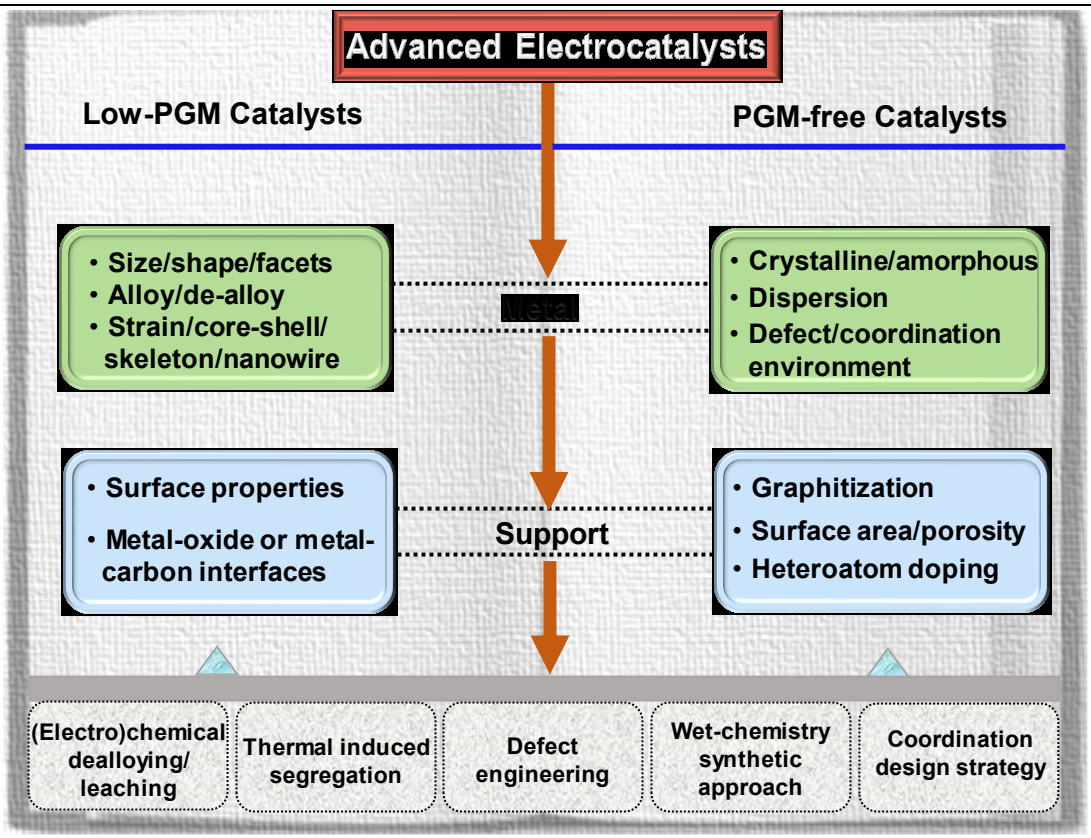

Figure 19. Schematic overview of strategies to design advanced heterogeneous electrocatalysts, including low-PGM and PGM-free materials for clean energy conversion.

Overall, PGM catalysts represent the state-of-the-art for their respective applications, but the scarcity and high price of PGMs significantly limit their large-scale implementation. PGM-free catalysts are highly desirable for sustainability but often suffer from insufficient activity and stability, which represents a high-risk, but high-reward research direction. As for OER catalysts in acidic media for PEM electrolyzers, RuO_2 is the most active, while IrO_2 is stable. There are no currently promising PGM-free catalysts due to the grand stability challenge, but amorphous transition metal phosphides and oxides might be within a respectable striking distance.[50, 278] The ORR for PEMFCs has been studied extensively in past decades with significant progress in mechanistic understanding, catalyst synthesis, and performance improvement. The corresponding

PEMFCs have already entered the early stages of commercialization for transportation, but the current challenges for further commercialization are high-cost, unsatisfactory durability, and insufficient power density. Compared to studied PtM alloy catalysts, highly ordered PtCo intermetallic nanoparticles exhibited remarkably enhanced activity and stability in MEA tests, which surpassed DOE targets. The atomically dispersed M-N-C catalysts are the most promising PGM-free formulation in challenging acidic media, which already demonstrated encouraging activity and reasonable stability in MEAs but are still far from the requirements for viable applications.

Electrosynthesis of ammonia via the NRR, especially from H_2O and N_2, has attracted substantial attention recently, as a result of the new Renewable Energy to Fuels Through Utilization of Energy-Dense Liquids (REFUEL) program launched in 2016 by the U.S. DOE. However, the production of ammonia with a sufficient rate and Faradaic efficiency is more challenging than expected due to the lack of highly active and selective NRR catalysts, compatible electrolytes, and electrolyzer systems. The progress in developing highly active catalysts in past years somewhat is disappointing. Commercializing this technology is challenging in the predictable future. However, researchers around the world remain great enthusiasm in exploring NRR catalysts, mainly focusing on (i) atomically dispersed single metal sites, (ii) metallic alloys, and (iii) carbon-based catalysts with optimal dopants/defects. Integrating active catalysts with optimal electrolytes is crucial for balancing the proton supplies to the NRR and the inhibition of the competitive HER. Among studied electrolytes, ionic liquids hold great promise in promoting the NRR, but their high cost is

an issue. Compared to acidic media, neutral and alkaline electrolytes often boost the NRR with enhanced production rates and FE.[50, 55] The sufficient NRR activity for potential commercialization by 2050 aims to achieve target production rates of 10^{-3} mol $h^{-1}cm^{-2}$ and >50% FE.

Compared to other fuel cells, the DAFC is more challenging and less studied due to a sluggish AOR anodic reaction, NH_3 crossover, and poisoning effects on the PGM cathode. However, the urgent demand to utilize NH_3 as a carbon-free liquid fuel motivates researchers to re-visit AOR catalysis and its integration with AEM membranes. Currently, the premier AOR catalyst is a PtIr binary alloy catalyst. AOR activity specifically can be further enhanced by controlling facet orientation, engineering nanostructures, introducing third metals into PtIr systems, and selecting optimal supports. PGM-free catalysts cannot significantly reduce the overpotential yet and generate reasonable current density, therefore showing no feasibility for the DAFCs in the foreseeable future. Unlike other electrochemical reactions, AOR activity is greatly temperature-dependent, with elevated temperatures leading to significant activity enhancement. Therefore, DAFCs are more favorable in high- and intermediate- temperature systems, which requires the development of appropriately compatible electrolytes.

As for efficient energy technologies, MEA-level studies for electrocatalysis are more valuable in terms of performance improvement and durability, which principally rely on the optimization in the design and engineering interfaces of catalysts and electrolytes within 3D porous electrodes. This task is more challenging but more meaningful, which often requires a holistic effort to address

these issues related to charge-transfer and mass transport under real operation conditions. Eventually, these clean and sustainable energy technologies with sufficient performance and durability would address current issues humanity is facing to combat climate change and fossil energy dependence.

Acknowledgments

We acknowledge the financial supports from the U.S. Department of Energy, Office of Energy Efficiency and Renewable Energy (EERE), Fuel Cell Technology Office along the Advanced Research Projects Agency-Energy (ARPA-E) office's REFUEL program. P. Xu thanks the support from the National Natural Science Foundation of China (21671047, 21871065). G. Wu is also grateful for the supports from the National Science Foundation (CBET-1604392, 1804326).

Received: ((will be filled in by the editorial staff))
Revised: ((will be filled in by the editorial staff))
Published online: ((will be filled in by the editorial staff))

References

[1] C. Rozain, E. Mayousse, N. Guillet, P. Millet, *Appl. Catal. B Environ.* **2016**, 182, 153.

[2] D. Banham, J. Y. Choi, T. Kishimoto, S. Ye, *Adv. Mater.* **2019**, 31, 1804846.

[3] S. K. Singh, K. Takeyasu, J. Nakamura, *Adv. Mater.* **2019**, 31, 1804297.

[4] S. Ghosh, R. N. Basu, *Nanoscale* **2018**, 10, 11241.

[5] K. Ithisuphalap, H. Zhang, L. Guo, Q. Yang, H. Yang, G. Wu, *Small Methods* **2019**, 3, 1800352.

[6] M. Tahir, L. Pan, F. Idrees, X. Zhang, L. Wang, J.-J. Zou, Z. L. Wang, *Nano Energy* **2017**,

37, 136.

[7] P. Peng, L. Shi, F. Huo, S. Zhang, C. Mi, Y. Cheng, Z. Xiang, *ACS Nano* **2019**, 13, 878.

[8] H. Osgood, S. V. Devaguptapu, H. Xu, J. Cho, G. Wu, *Nano Today* **2016**, 11, 601.

[9] S. Gupta, W. Kellogg, H. Xu, X. Liu, J. Cho, G. Wu, *Chem. Asian. J.* **2016**, 11, 10.

[10] X. X. Wang, V. Prabhakaran, Y. He, Y. Shao, G. Wu, *Adv. Mater.* **2019**, 31, 1805126.

[11] Y. Xiong, Y. Yang, F. J. DiSalvo, H. D. Abruna, *J. Am. Chem. Soc.* **2018**, 140, 7248.

[12] G. Wu, K. L. More, C. M. Johnston, P. Zelenay, *Science* **2011**, 332, 443.

[13] G. Wu, A. Santandreu, W. Kellogg, S. Gupta, O. Ogoke, H. Zhang, H.-L. Wang, L. Dai, *Nano Energy* **2016**, 29, 83.

[14] Q. Li, R. Cao, J. Cho, G. Wu, *Adv. Energy Mater.* **2014**, 4, 1301415.

[15] S. L. Foster, S. I. P. Bakovic, R. D. Duda, S. Maheshwari, R. D. Milton, S. D. Minteer, M. J. Janik, J. N. Renner, L. F. Greenlee, *Nat. Catal.* **2018**, 1, 490.

[16] C. Liu, Q. Li, C. Wu, J. Zhang, Y. Jin, D. R. MacFarlane, C. Sun, *J. Am. Chem. Soc.* **2019**, 141, 2884.

[17] H. K. Lee, C. S. L. Koh, Y. H. Lee, C. Liu, I. Y. Phang, X. Han, C. K. Tsung, X. Y. Ling, *Sci. Adv.* **2018**, 4, eaar3208.

[18] F. Jiao, B. Xu, *Adv. Mater.* **2019**, 31, 1805173.

[19] A. Najafian, T. R. Cundari, *J. Phys. Chem. A* **2019**, 123, 7973.

[20] J. R. Barbosa, M. N. Leon, C. M. Fernandes, R. M. Antoniassi, O. C. Alves, E. A. Ponzio, J. C. M. Silva, *Appl. Catal. B Environ.* **2020**, 264, 118458.

[21] L. Song, Z. Liang, Z. Ma, Y. Zhang, J. Chen, R. R. Adzic, J. X. Wang, *J. Electrochem. Soc.* **2018**, 165, J3095.

[22] Y. Zhu, J. Sokolowski, X. Song, Y. He, Y. Mei, G. Wu, *Adv. Energy Mater.* **2019**, 10, 1902844.

[23] A. Wang, J. Li, T. Zhang, *Nat. Rev. Chem.* **2018**, 2, 65.

[24] S. Anantharaj, S. R. Ede, K. Sakthikumar, K. Karthick, S. Mishra, S. Kundu, *ACS Catal.* **2016**, 6, 8069.

[25] H. Kim, H. Park, D.-K. Kim, S. Oh, I. Choi, S.-K. Kim, *ACS Sustainable Chem. Eng.* **2019**, 7, 8265.

[26] Z. Kang, G. Yang, J. Mo, Y. Li, S. Yu, D. A. Cullen, S. T. Retterer, T. J. Toops, G. Bender, B. S. Pivovar, J. B. Green, F.-Y. Zhang, *Nano Energy* **2018**, 47, 434.

[27] J. Jiang, W. Ding, W. Li, Z. Wei, *Chem* **2019**, 6, 1.

[28] X. Zhao, S. Chen, Z. Fang, J. Ding, W. Sang, Y. Wang, J. Zhao, Z. Peng, J. Zeng, *J. Am. Chem. Soc.* **2015**, 137, 2804.

[29] Z. W. Gao, J. Y. Liu, X. M. Chen, X. L. Zheng, J. Mao, H. Liu, T. Ma, L. Li, W. C. Wang, X. W. Du, *Adv. Mater.* **2019**, 31, 1804769.

[30] N. M. Adli, H. Zhang, S. Mukherjee, G. Wu, *J. Electrochem. Soc.* **2018**, 165, J3130.

[31] Y. Shao, N. M. Markovic, *Nano Energy* **2016**, 29, 1.

[32] D. Opalka, C. Scheurer, K. Reuter, *ACS Catal.* **2019**, 9, 4944.

[33] H. Kim, J. Kim, S.-K. Kim, S. H. Ahn, *Appl. Catal. B Environ.* **2018**, 232, 93.

[34] A. Chitsaz, M. A. Haghghi, J. Hosseinpour, *Energy Convers. Manage.* **2019**, 186, 487.

[35] J. Suntivich, K. J. May, H. A. Gasteiger, J. B. Goodenough, Y. Shao-Horn, *Science* **2011**, 334, 1383.

[36] Q. Feng, Q. Wang, Z. Zhang, Y. Xiong, H. Li, Y. Yao, X.-Z. Yuan, M. C. Williams, M. Gu, H. Chen, H. Li, H. Wang, *Appl. Catal. B Environ.* **2019**, 244, 494.

[37] Q. Shi, C. Zhu, D. Du, Y. Lin, *Chem. Soc. Rev.* **2019**, 48, 3181.

[38] R. Abbasi, B. P. Setzler, S. Lin, J. Wang, Y. Zhao, H. Xu, B. Pivovar, B. Tian, X. Chen, G. Wu, Y. Yan, *Adv. Mater.* **2019**, 31, 1805876.

[39] M. Carmo, D. L. Fritz, J. Mergel, D. Stolten, *Int. J. Hydrogen Energy* **2013**, 38, 4901.

[40] S. Gupta, L. Qiao, S. Zhao, H. Xu, Y. Lin, S. V. Devaguptapu, X. Wang, M. T. Swihart, G. Wu, *Adv. Energy Mater.* **2016**, 6, 1601198.

[41] B. Zhang, X. Zheng, O. Voznyy, R. Comin, M. Bajdich, M. García-Melchor, L. Han, J. Xu, M. Liu, L. Zheng, F. P. García de Arquer, C. T. Dinh, F. Fan, M. Yuan, E. Yassitepe, N. Chen, T. Regier, P. Liu, Y. Li, P. D. Luna, A. Janmohamed, H. L. Xin, H. Yang, A. Vojvodic, E. H. Sargent, *Science* **2016**, 352, 333.

[42] Z. Huang, J. Song, Y. Du, S. Xi, S. Dou, J. M. V. Nsanzimana, C. Wang, Z. J. Xu, X. Wang, *Nat. Energy* **2019**, 4, 329.

[43] J. Gao, C. Q. Xu, S. F. Hung, W. Liu, W. Cai, Z. Zeng, C. Jia, H. M. Chen, H. Xiao, J. Li, Y. Huang, B. Liu, *J. Am. Chem. Soc.* **2019**, 141, 3014.

[44] S. Gupta, S. Zhao, X. X. Wang, S. Hwang, S. Karakalos, S. V. Devaguptapu, S. Mukherjee,

D. Su, H. Xu, G. Wu, *ACS Catal.* **2017**, 7, 8386.

[45] F. Lyu, Q. Wang, S. M. Choi, Y. Yin, *Small* **2019**, 15, 1804201.

[46] M. Chen, L. Wang, H. Yang, S. Zhao, H. Xu, G. Wu, *J. Power Sources* **2018**, 375, 277.

[47] L. Lv, Z. Yang, K. Chen, C. Wang, Y. Xiong, *Adv. Energy Mater.* **2019**, 9, 1803358.

[48] W. Li, C. Min, F. Tan, Z. Li, B. Zhang, R. Si, M. Xu, W. Liu, L. Zhou, Q. Wei, Y. Zhang, X. Yang, *ACS Nano* **2019**, 13, 3177.

[49] C. Lei, S. Lyu, J. Si, B. Yang, Z. Li, L. Lei, Z. Wen, G. Wu, Y. Hou, *ChemCatChem* **2019**, 11, 5855.

[50] T. Wang, H. Xie, M. Chen, A. D'Aloia, J. Cho, G. Wu, Q. Li, *Nano Energy* **2017**, 42, 69.

[51] Q. Shi, C. Zhu, D. Du, Y. Lin, *Chem. Soc. Rev.* **2019**, 48, 3181.

[52] D. Peterson, J. Vickers, D. DeSantis, **2020**, https://www.hydrogen.energy.gov/pdfs/19009_h2_production_cost_pem_electrolysis_2019.pdf.

[53] Y. Yao, X. K. Gu, D. He, Z. Li, W. Liu, Q. Xu, T. Yao, Y. Lin, H. J. Wang, C. Zhao, X. Wang, P. Yin, H. Li, X. Hong, S. Wei, W. X. Li, Y. Li, Y. Wu, *J. Am. Chem. Soc.* **2019**, 141, 19964.

[54] Z. W. Seh, J. Kibsgaard, C. F. Dickens, Ib Chorkendorff, J. K. Nørskov, T. F. Jaramillo, *Science* **2017**, 355, 1.

[55] G. Wu, N. Li, C. S. Dai, D. R. Zhou, *Mater. Chem. Phys.* **2004**, 83, 307.

[56] J. Rossmeisl, A. Logadottir, J. K. Nørskov, *Chem. Phys.* **2005**, 319, 178.

[57] Z. Xu, J. Rossmeisl, J. R. Kitchin, *J. Phys. Chem. C* **2015**, 119, 4827.

[58] L. C. Seitz, C. F. Dickens, K. Nishio, Y. Hikita, J. Montoya, A. Doyle, C. Kirk, A. Vojvodic, H. Y. Hwang, J. K. Norskov, T. F. Jaramillo, *Science* **2016**, 353, 1011.

[59] H. N. Nong, H. S. Oh, T. Reier, E. Willinger, M. G. Willinger, V. Petkov, D. Teschner, P. Strasser, *Angew. Chem. Int. Ed.* **2015**, 54, 2975.

[60] M. Huynh, D. K. Bediako, D. G. Nocera, *J. Am. Chem. Soc.* **2014**, 136, 6002.

[61] R. Frydendal, E. A. Paoli, I. Chorkendorff, J. Rossmeisl, I. E. L. Stephens, *Adv. Energy Mater.* **2015**, 5, 1500991.

[62] I. A. Moreno-Hernandez, C. A. MacFarland, C. G. Read, K. M. Papadantonakis, B. S. Brunschwig, N. S. Lewis, *Energy Environ. Sci.* **2017**, 10, 2103.

[63] J. S. Mondschein, J. F. Callejas, C. G. Read, J. Y. C. Chen, C. F. Holder, C. K. Badding, R. E. Schaak, *Chem. Mater.* **2017**, 29, 950.

[64] F. Hu, S. Zhu, S. Chen, Y. Li, L. Ma, T. Wu, Y. Zhang, C. Wang, C. Liu, X. Yang, L. Song, X. Yang, Y. Xiong, *Adv. Mater.* **2017**, 29, 1606570.

[65] M. Blasco-Ahicart, J. Soriano-Lopez, J. J. Carbo, J. M. Poblet, J. R. Galan-Mascaros, *Nat. Chem.* **2018**, 10, 24.

[66] C. Lei, H. Chen, J. Cao, J. Yang, M. Qiu, Y. Xia, C. Yuan, B. Yang, Z. Li, X. Zhang, L. Lei, J. Abbott, Y. Zhong, X. Xia, G. Wu, Q. He, Y. Hou, *Adv. Energy Mater.* **2018**, 8, 1801912.

[67] P. Lettenmeier, L. Wang, U. Golla-Schindler, P. Gazdzicki, N. A. Canas, M. Handl, R. Hiesgen, S. S. Hosseiny, A. S. Gago, K. A. Friedrich, *Angew. Chem. Int. Ed.* **2016**, 55, 742.

[68] L. Wang, V. A. Saveleva, S. Zafeiratos, E. R. Savinova, P. Lettenmeier, P. Gazdzicki, A. S. Gago, K. A. Friedrich, *Nano Energy* **2017**, 34, 385.

[69] Y. Yao, S. Hu, W. Chen, Z.-Q. Huang, W. Wei, T. Yao, R. Liu, K. Zang, X. Wang, G. Wu, W. Yuan, T. Yuan, B. Zhu, W. Liu, Z. Li, D. He, Z. Xue, Y. Wang, X. Zheng, J. Dong, C.-R. Chang, Y. Chen, X. Hong, J. Luo, S. Wei, W.-X. Li, P. Strasser, Y. Wu, Y. Li, *Nat. Catal.* **2019**, 2, 304.

[70] J. Shan, C. Guo, Y. Zhu, S. Chen, L. Song, M. Jaroniec, Y. Zheng, S.-Z. Qiao, *Chem* **2019**, 5, 445.

[71] J. Cheng, J. Yang, S. Kitano, G. Juhasz, M. Higashi, M. Sadakiyo, K. Kato, S. Yoshioka, T. Sugiyama, M. Yamauchi, N. Nakashima, *ACS Catal.* **2019**, 9, 6974.

[72] K. A. Stoerzinger, R. R. Rao, X. R. Wang, W. T. Hong, C. M. Rouleau, Y. Shao-Horn, *Chem* **2017**, 2, 668.

[73] X. Wang, Y. Zhu, A. Vasileff, Y. Jiao, S. Chen, L. Song, B. Zheng, Y. Zheng, S.-Z. Qiao, *ACS Energy Lett.* **2018**, 3, 1198.

[74] U. Martinez, S. Komini Babu, E. F. Holby, H. T. Chung, X. Yin, P. Zelenay, *Adv. Mater.* **2019**, 31, 1806545.

[75] R. F. Service, *Science* **2020**, 367, 1181.

[76] M. G. Chourashiya, A. Urakawa, *J. Mater. Chem. A* **2017**, 5, 4774.

[77] M. Faustini, M. Giraud, D. Jones, J. Rozière, M. Dupont, T. R. Porter, S. Nowak, M. Bahri, O. Ersen, C. Sanchez, C. Boissière, C. Tard, J. Peron, *Adv. Energy Mater.* **2019**, 9, 1802136.

[78] Ö. F. Selamet, F. Becerikli, M. D. Mat, Y. Kaplan, *Int. J. Hydrogen Energy* **2011**, 36, 11480.

[79] E. Rasten, G. Hagen, R. Tunold, *Electrochim. Acta* **2003**, 48, 3945.

[80] A. Marshall, B. Børresen, G. Hagen, M. Tsypkin, R. Tunold, *Electrochim. Acta* **2006**, 51, 3161.

[81] V. Baglio, R. Ornelas, F. Matteucci, F. Martina, G. Ciccarella, I. Zama, L. G. Arriaga, V. Antonucci, A. S. Aricò, *Fuel Cells* **2009**, 9, 247.

[82] V. Antonucci, A. Di Blasi, V. Baglio, R. Ornelas, F. Matteucci, J. Ledesma-Garcia, L. G. Arriaga, A. S. Aricò, *Electrochim. Acta* **2008**, 53, 7350.

[83] S. Siracusano, V. Baglio, N. Briguglio, G. Brunaccini, A. Di Blasi, A. Stassi, R. Ornelas, E. Trifoni, V. Antonucci, A. S. Aricò, *Int. J. Hydrogen Energy* **2012**, 37, 1939.

[84] W. Tong, M. Forster, F. Dionigi, S. Dresp, R. Sadeghi Erami, P. Strasser, A. J. Cowan, P. Farràs, *Nature Energy* **2020**, DOI: 10.1038/s41560-020-0550-8.

[85] M. Elimelech, W. A. Phillip, *Science* **2011**, 333, 712.

[86] Y. Kuang, M. J. Kenney, Y. Meng, W. H. Hung, Y. Liu, J. E. Huang, R. Prasanna, P. Li, Y. Li, L. Wang, M. C. Lin, M. D. McGehee, X. Sun, H. Dai, *Proc. Natl. Acad. Sci. U. S. A.* **2019**, 116, 6624.

[87] S. Dresp, F. Dionigi, M. Klingenhof, P. Strasser, *ACS Energy Lett.* **2019**, 4, 933.

[88] S. Fukuzumi, Y. M. Lee, W. Nam, *ChemSusChem* **2017**, 10, 4264.

[89] L. O. Williams, *Veziroğlu T.N. (eds) Hydrogen Energy.* **1975**, Springer, Boston, MA.

[90] G. Amikam, P. Nativ, Y. Gendel, *Int. J. Hydrogen Energy* **2018**, 43, 6504.

[91] V. Petrykin, K. Macounova, O. A. Shlyakhtin, P. Krtil, *Angew. Chem. Int. Ed.* **2010**, 49, 4813

[92] R. Balaji, B. S. Kannan, J. Lakshmi, N. Senthil, S. Vasudevan, G. Sozhan, A. K. Shukla, S. Ravichandran, *Electrochem. Commun.* **2009**, 11, 1700.

[93] R. Venkatkarthick, S. Elamathi, D. Sangeetha, R. Balaji, B. Suresh Kannan, S. Vasudevan, D. Jonas Davidson, G. Sozhan, S. Ravichandran, *J. Electroanal. Chem.* **2013**, 697, 1.

[94] J. G. Vos, T. A. Wezendonk, A. W. Jeremiasse, M. T. M. Koper, *J. Am. Chem. Soc.* **2018**, 140, 10270.

[95] H. Li, Q. Tang, B. He, P. Yang, *J. Mater. Chem. A* **2016**, 4, 6513.

[96] J. Zheng, Y. Zhao, H. Xi, C. Li, *RSC Adv.* **2018**, 8, 9423.

[97] A. Indra, T. Song, U. Paik, *Adv. Mater.* **2018**, 30, 1705146.

[98] G. Zhang, Y. Jia, C. Zhang, X. Xiong, K. Sun, R. Chen, W. Chen, Y. Kuang, L. Zheng, H. Tang, W. Liu, J. Liu, X. Sun, W.-F. Lin, H. Dai, *Energy Environ. Sci.* **2019**, 12, 1317.

[99] C. Zhu, H. Li, S. Fu, D. Du, Y. Lin, *Chem. Soc. Rev.* **2016**, 45, 517.

[100] Y.-J. Wang, B. Fang, D. Zhang, A. Li, D. P. Wilkinson, A. Ignaszak, L. Zhang, J. Zhang, *Electrochem. Energy Rev.* **2018**, 1, 1.

[101] M. K. Debe, *Nature* **2012**, 486, 43.

[102] D. Banham, S. Ye, *ACS Energy Lett.* **2017**, 2, 629.

[103] J. M. Andújar, F. Segura, *Renewable Sustainable Energy Rev.* **2009**, 13, 2309.

[104] M. S. Wilson, S. Gottesfeld, *J. Electrochem. Soc.* **1992**, 139, L28.

[105] R. Chattot, O. Le Bacq, V. Beermann, S. Kuhl, J. Herranz, S. Henning, L. Kuhn, T. Asset, L. Guetaz, G. Renou, J. Drnec, P. Bordet, A. Pasturel, A. Eychmuller, T. J. Schmidt, P. Strasser, L. Dubau, F. Maillard, *Nat. Mater.* **2018**, 17, 827.

[106] L. Yang, D. Cheng, H. Xu, X. Zeng, X. Wan, J. Shui, Z. Xiang, D. Cao, *Proc. Natl. Acad. Sci. U. S. A.* **2018**, 115, 6626.

[107] L. Guo, W.-J. Jiang, Y. Zhang, J.-S. Hu, Z.-D. Wei, L.-J. Wan, *ACS Catal.* **2015**, 5, 2903.

[108] S. Chen, N. Zhang, C. W. Narváez Villarrubia, X. Huang, L. Xie, X. Wang, X. Kong, H. Xu, G. Wu, J. Zeng, H.-L. Wang, *Nano Energy* **2019**, 66, 104164.

[109] A. Kulkarni, S. Siahrostami, A. Patel, J. K. Norskov, *Chem. Rev.* **2018**, 118, 2302.

[110] H. Mistry, A. S. Varela, S. Kühl, P. Strasser, B. R. Cuenya, *Nat. Rev. Mater.* **2016**, 1, 1.

[111] Y. Li, J. Yang, J. Huang, Y. Zhou, K. Xu, N. Zhao, X. Cheng, *Carbon* **2017**, 122, 237.

[112] X. X. Wang, M. T. Swihart, G. Wu, *Nat. Catal.* **2019**, 2, 578.

[113] *https://www.energy.gov/eere/fuelcells/doe-technical-targets-polymer-electrolyte-membrane-fuel-cell-components* **2020**.

[114] J. A. Keith, T. Jacob, *Angew. Chem. Int. Ed.* **2010**, 49, 9521.

[115] H. T. Chung, D. A. Cullen, D. Higgins, B. T. Sneed, E. F. Holby, K. L. More, P. Zelenay, *Sicence* **2017**, 357, 479.

[116] D. Guo, R. Shibuya, C. Akiba, S. Saji, T. Kondo, J. Nakamura, *Science* **2016**, 351, 361.

[117] Y. Nie, L. Li, Z. Wei, *Chem. Soc. Rev.* **2015**, 44, 2168.

[118] J. Hou, M. Yang, C. Ke, G. Wei, C. Priest, Z. Qiao, G. Wu, J. Zhang, *EnergyChem* **2020**, 2,

100023.

[119] X. X. Wang, J. Sokolowski, H. Liu, G. Wu, *Chin. J. Catal.* **2020**, 41, 739.

[120] X. Wang, Z. Li, Y. Qu, T. Yuan, W. Wang, Y. Wu, Y. Li, *Chem* **2019**, 5, 1.

[121] S. T. Thompson, A. R. Wilson, P. Zelenay, D. J. Myers, K. L. More, K. C. Neyerlin, D. Papageorgopoulos, *Solid State Ionics* **2018**, 319, 68.

[122] X. X. Wang, D. A. Cullen, Y. T. Pan, S. Hwang, M. Wang, Z. Feng, J. Wang, M. H. Engelhard, H. Zhang, Y. He, Y. Shao, D. Su, K. L. More, J. S. Spendelow, G. Wu, *Adv. Mater.* **2018**, 30, 1706758.

[123] X. Zheng, J. Wu, X. Cao, J. Abbott, C. Jin, H. Wang, P. Strasser, R. Yang, X. Chen, G. Wu, *Appl. Catal. B Environ.* **2019**, 241, 442.

[124] Y. He, Q. Tan, L. Lu, J. Sokolowski, G. Wu, *Electrochem. Energy Rev.* **2019**, 2, 231.

[125] Y. Li, H. Wen, J. Yang, Y. Zhou, X. Cheng, *Carbon* **2019**, 142, 1.

[126] Z. Zhang, M. Dou, J. Ji, F. Wang, *Nano Energy* **2017**, 34, 338.

[127] Y. Zhao, J. Wan, H. Yao, L. Zhang, K. Lin, L. Wang, N. Yang, D. Liu, L. Song, J. Zhu, L. Gu, L. Liu, H. Zhao, Y. Li, D. Wang, *Nat. Chem.* **2018**, 10, 924.

[128] H. Zhang, S. Hwang, M. Wang, Z. Feng, S. Karakalos, L. Luo, Z. Qiao, X. Xie, C. Wang, D. Su, Y. Shao, G. Wu, *J. Am. Chem. Soc.* **2017**, 139, 14143.

[129] S. Gupta, S. Zhao, O. Ogoke, Y. Lin, H. Xu, G. Wu, *ChemSusChem* **2017**, 10, 774.

[130] G. Wu, *Front. Energy* **2017**, 11, 286.

[131] H. Zhang, J. Li, Q. Tan, L. Lu, Z. Wang, G. Wu, *Chem. Euro. J.* **2018**, 24, 18137.

[132] H. Zhang, H. Osgood, X. Xie, Y. Shao, G. Wu, *Nano Energy* **2017**, 31, 331.

[133] X. Wang, H. Zhang, H. Lin, S. Gupta, C. Wang, Z. Tao, H. Fu, T. Wang, J. Zheng, G. Wu, X. Li, *Nano Energy* **2016**, 25, 110.

[134] W. Xia, A. Mahmood, R. Zou, Q. Xu, *Energy Environ. Sci.* **2015**, 8, 1837.

[135] T. Qiu, Z. Liang, W. Guo, H. Tabassum, S. Gao, R. Zou, *ACS Energy Lett.* **2020**, 5, 520.

[136] M. Li, Z. Zhao, T. Cheng, A. Fortunelli, C.-Y. Chen, R. Yu, Q. Zhang, L. Gu, B. V. Merinov, Z. Lin, E. Zhu, T. Yu, Q. Jia, J. Guo, L. Zhang, W. A. Goddard III, Y. Huang, X. Duan, *Science* **2016**, 354, 1414.

[137] Z. Qiao, S. Hwang, X. Li, C. Wang, W. Samarakoon, S. Karakalos, D. Li, M. Chen, Y. He, M. Wang, Z. Liu, G. Wang, H. Zhou, Z. Feng, D. Su, J. S. Spendelow, G. Wu, *Energy Environ. Sci.* **2019**, 12, 2830.

[138] L. Chong, H. Barkholtz, W. Ding, J. Wen, J. Kubal, F. G. Sen, J. Zou, D. Liu, *Science* **2018**, 362, 1276.

[139] X. X. Wang, S. Hwang, Y. T. Pan, K. Chen, Y. He, S. Karakalos, H. Zhang, J. S. Spendelow, D. Su, G. Wu, *Nano Lett.* **2018**, 18, 4163.

[140] J. Li, S. Sharma, X. Liu, Y.-T. Pan, J. S. Spendelow, M. Chi, Y. Jia, P. Zhang, D. A. Cullen, Z. Xi, H. Lin, Z. Yin, B. Shen, M. Muzzio, C. Yu, Y. S. Kim, A. A. Peterson, K. L. More, H. Zhu, S. Sun, *Joule* **2019**, 3, 124.

[141] H. Zhang, H. T. Chung, D. A. Cullen, S. Wagner, U. I. Kramm, K. L. More, P. Zelenay, G. Wu, *Energy Environ. Sci.* **2019**, 12, 2548.

[142] J. Li, H. Zhang, W. Samarakoon, W. Shan, D. A. Cullen, S. Karakalos, M. Chen, D. Gu, K. L. More, G. Wang, Z. Feng, Z. Wang, G. Wu, *Angew. Chem. Int. Ed.* **2019**, 58, 18971.

[143] Y. He, S. Hwang, D. A. Cullen, M. A. Uddin, L. Langhorst, B. Li, S. Karakalos, A. J. Kropf, E. C. Wegener, J. Sokolowski, M. Chen, D. Myers, D. Su, K. L. More, G. Wang, S. Litster, G. Wu, *Energy Environ. Sci.* **2019**, 12, 250.

[144] J. Li, M. Chen, D. A. Cullen, S. Hwang, M. Wang, B. Li, K. Liu, S. Karakalos, M. Lucero, H. Zhang, C. Lei, H. Xu, G. E. Sterbinsky, Z. Feng, D. Su, K. L. More, G. Wang, Z. Wang, G. Wu, *Nat. Catal.* **2018**, 1, 935.

[145] X. Ren, Q. Lv, L. Liu, B. Liu, Y. Wang, A. Liu, G. Wu, *Sustainable Energy Fuels* **2020**, 4, 15.

[146] M. Chen, S. Hwang, J. Li, S. Karakalos, K. Chen, Y. He, S. Mukherjee, D. Su, G. Wu, *Nanoscale* **2018**, 10, 17318.

[147] J. Liang, F. Ma, S. Hwang, X. Wang, J. Sokolowski, Q. Li, G. Wu, D. Su, *Joule* **2019**, 3, 956.

[148] L. Zhang, L. T. Roling, X. Wang, M. Vara, M. Chi, J. Liu, S. Choi, J. Park, J. A. Herron, Z. Xie, M. Mavrikakis, Y. Xia, *Science* **2015**, 349, 412.

[149] S. Mukerjee, S. Srinivasan, *J. Electroanal. Chem* **1993**, 357, 201.

[150] X. Huang, Z. Zhao, L. Cao, Y. Chen, E. Zhu, Z. Lin, M. Li, A. Yan, A. Zettl, Y. M. Wang, X. Duan, T. Mueller, Y. Huang, *Science* **2015**, 348, 1230.

[151] V. R. Stamenkovic, B. S. Mun, M. Arenz, K. J. Mayrhofer, C. A. Lucas, G. Wang, P. N.

Ross, N. M. Markovic, *Nat. Mater.* **2007**, 6, 241.

[152] Q. Li, L. Wu, G. Wu, D. Su, H. Lv, S. Zhang, W. Zhu, A. Casimir, H. Zhu, A. Mendoza-Garcia, S. Sun, *Nano Lett.* **2015**, 15, 2468.

[153] X. X. Wang, S. Hwang, Y. T. Pan, K. Chen, Y. He, S. Karakalos, H. Zhang, J. S. Spendelow, D. Su, G. Wu, *Nano. Lett.* **2018**, 18, 4163.

[154] G. Wu, Y.-S. Chen, B.-Q. Xu, *Electrochem. Commun.* **2005**, 7, 1237.

[155] Y. Li, J. Yang, K. Xu, *Key Eng. Mater.* **2017**, 727, 322.

[156] G. Wu, D. Li, C. Dai, D. Wang, N. Li, *Langmuir* **2008**, 24, 3566.

[157] G. Wu, C. Dai, D. Wang, D. Li, N. Li, *J. Mater. Chem. A* **2010**, 20, 3059.

[158] Q. Li, H. Pan, D. Higgins, R. Cao, G. Zhang, H. Lv, K. Wu, J. Cho, G. Wu, *Small* **2015**, 11, 1443.

[159] M. Luo, Y. Sun, X. Zhang, Y. Qin, M. Li, Y. Li, C. Li, Y. Yang, L. Wang, P. Gao, G. Lu, S. Guo, *Adv. Mater.* **2018**, 30, 1705515.

[160] G. Wu, P. Zelenay, *Acc. Chem. Res.* **2013**, 46, 1878.

[161] F. Jaouen, E. Proietti, M. Lefèvre, R. Chenitz, J.-P. Dodelet, G. Wu, H. T. Chung, C. M. Johnston, P. Zelenay, *Energy Environ. Sci.* **2011**, 4, 114.

[162] H. Zhang, S. Ding, S. Hwang, X. Zhao, D. Su, H. Xu, H. Yang, G. Wu, *J. Electrochem. Soc.* **2019**, 166, F3116.

[163] Q. Li, P. Xu, W. Gao, S. Ma, G. Zhang, R. Cao, J. Cho, H. L. Wang, G. Wu, *Adv. Mater.* **2014**, 26, 1378.

[164] Z. Qiao, H. Zhang, S. Karakalos, S. Hwang, J. Xue, M. Chen, D. Su, G. Wu, *Appl. Catal. B Environ.* **2017**, 219, 629.

[165] G. Wu, N. H. Mack, W. Gao, S. Ma, R. Zhong, J. Han, J. K. Baldwin, P. Zelenay, *ACS Nano* **2012**, 6, 9764.

[166] M. Xiao, H. Zhang, Y. Chen, J. Zhu, L. Gao, Z. Jin, J. Ge, Z. Jiang, S. Chen, C. Liu, W. Xing, *Nano Energy* **2018**, 46, 396.

[167] Y. Qu, Z. Li, W. Chen, Y. Lin, T. Yuan, Z. Yang, C. Zhao, J. Wang, C. Zhao, X. Wang, F. Zhou, Z. Zhuang, Y. Wu, Y. Li, *Nat. Catal.* **2018**, 1, 781.

[168] F. Pan, H. Zhang, Z. Liu, D. Cullen, K. Liu, K. More, G. Wu, G. Wang, Y. Li, *J. Mater. Chem. A* **2019**, 7, 26231.

[169] W. Zheng, C. Guo, J. Yang, F. He, B. Yang, Z. Li, L. Lei, J. Xiao, G. Wu, Y. Hou, *Carbon* **2019**, 150, 52.

[170] S. Mukherjee, X. Yang, W. Shan, W. Samarakoon, S. Karakalos, D. A. Cullen, K. More, M. Wang, Z. Feng, G. Wang, G. Wu, *Small Methods* **2020**, 4, 1900821.

[171] K. Liu, Z. Qiao, S. Hwang, Z. Liu, H. Zhang, D. Su, H. Xu, G. Wu, G. Wang, *Appl. Catal. B Environ.* **2019**, 243, 195.

[172] T. Asset, P. Atanassov, *Joule* **2020**, 4, 1.

[173] W. Wang, Q. Jia, S. Mukerjee, S. Chen, *ACS Catal.* **2019**, 9, 10126.

[174] A. Kongkanand, M. F. Mathias, *J. Phys. Chem. Lett.* **2016**, 7, 1127.

[175] M. K. Carpenter, T. E. Moylan, R. S. Kukreja, M. H. Atwan, M. M. Tessema, *J. Am. Chem.*

Soc. **2012**, 134, 8535.

[176] A. Uddin, L. Dunsmore, H. Zhang, L. Hu, G. Wu, S. Litster, *ACS Appl. Mater. Interfaces* **2020**, 12, 2216−2224.

[177] Y. Shao, J.-P. Dodelet, G. Wu, P. Zelenay, *Adv. Mater.* **2019**, 31, 1807615.

[178] B. H. R. Suryanto, H.-L. Du, D. Wang, J. Chen, A. N. Simonov, D. R. MacFarlane, *Nat. Catal.* **2019**, 2, 290.

[179] H. Xu, K. Ithisuphalap, Y. Li, S. Mukherjee, J. Lattimer, G. Soloveichik, G. Wu, *Nano Energy* **2020**, 69, 104469.

[180] X. Yang, J. Nash, J. Anibal, M. Dunwell, S. Kattel, E. Stavitski, K. Attenkofer, J. G. Chen, Y. Yan, B. Xu, *J. Am. Chem. Soc.* **2018**, 140, 13387.

[181] J. Deng, J. A. In˜ iguez, C. Liu, *Joule* **2018**, 2, 1.

[182] C. Guo, J. Ran, A. Vasileff, S.-Z. Qiao, *Energy Environ. Sci.* **2018**, 11, 45.

[183] L. Han, X. Liu, J. Chen, R. Lin, H. Liu, F. Lu, S. Bak, Z. Liang, S. Zhao, E. Stavitski, J. Luo, R. R. Adzic, H. L. Xin, *Angew. Chem. Int. Ed.* **2019**, 58, 2321.

[184] H. Tao, C. Choi, L.-X. Ding, Z. Jiang, Z. Han, M. Jia, Q. Fan, Y. Gao, H. Wang, A. W. Robertson, S. Hong, Y. Jung, S. Liu, Z. Sun, *Chem* **2019**, 5, 204.

[185] W. Sheng, Z. Zhuang, M. Gao, J. Zheng, J. G. Chen, Y. Yan, *Nat. Commun.* **2015**, 6, 5848.

[186] *https://arpa-e.energy.gov/?q=slick-sheet-project/anion-exchange-membrane-ammonia-production* **2017**.

[187] M. A. Shipman, M. D. Symes, *Catal. Today* **2017**, 286, 57.

[188] X. Cui, C. Tang, Q. Zhang, *Adv. Energy Mater.* **2018**, 8, 1800369.

[189] J. N. Renner, L. F. Greenlee, A. M. Herring, K. E. Ayers, *Electrochem. Soc. Interface* **2015**, 24, 51.

[190] C. J. van der Ham, M. T. Koper, D. G. Hetterscheid, *Chem. Soc. Rev.* **2014**, 43, 5183.

[191] N. Cao, G. Zheng, *Nano Res.* **2018**, 11, 2992.

[192] S. Zhao, X. Lu, L. Wang, J. Gale, R. Amal, *Adv. Mater.* **2019**, 31, 1805367.

[193] Q. Feng, S. Zhao, D. He, S. Tian, L. Gu, X. Wen, C. Chen, Q. Peng, D. Wang, Y. Li, *J. Am. Chem. Soc.* **2018**, 140, 2773.

[194] R. Manjunatha, A. Schechter, *Electrochem. Commun.* **2018**, 90, 96.

[195] X. Cui, C. Tang, X. M. Liu, C. Wang, W. Ma, Q. Zhang, *Chem. Eur. J.* **2018**, 24, 18494.

[196] N. Furuya, H. Yoshiba, *J. Electroanal. Chem.,* **1990**, 291, 269.

[197] R. J. Burford, M. D. Fryzuk, *Nat. Rev. Chem.* **2017**, 1, 0026.

[198] S. Z. Andersen, V. Čolić, S. Yang, J. A. Schwalbe, A. C. Nielander, J. M. McEnaney, K. Enemark-Rasmussen, J. G. Baker, A. R. Singh, B. A. Rohr, *Nature* **2019**, 570, 504.

[199] D. Bao, Q. Zhang, F. L. Meng, H. X. Zhong, M. M. Shi, Y. Zhang, J. M. Yan, Q. Jiang, X. B. Zhang, *Adv. Mater.* **2017**, 29, 1604799.

[200] H.-M. Liu, S.-H. Han, Y. Zhao, Y.-Y. Zhu, X.-L. Tian, J.-H. Zeng, J.-X. Jiang, B. Y. Xia, Y. Chen, *J. Mater. Chem. A* **2018**, 6, 3211.

[201] M.-M. Shi, D. Bao, S.-J. Li, B.-R. Wulan, J.-M. Yan, Q. Jiang, *Adv. Energy Mater.* **2018**, 8, 1800124.

[202] J. Kong, A. Lim, C. Yoon, J. H. Jang, H. C. Ham, J. Han, S. Nam, D. Kim, Y.-E. Sung, J. Choi, H. S. Park, *ACS Sustainable Chem. Eng.* **2017**, 5, 10986.

[203] W. Guo, Z. Liang, J. Zhao, B. Zhu, K. Cai, R. Zou, Q. Xu, *Small Methods* **2018**, 2, 1800204.

[204] S. Licht, B. Cui, B. Wang, F. F. Li, J. Lau, S. Liu, *Science* **2014**, 345, 637.

[205] S. Mukherjee, D. A. Cullen, S. Karakalos, K. Liu, H. Zhang, S. Zhao, H. Xu, K. L. More, G. Wang, G. Wu, *Nano Energy* **2018**, 48, 217.

[206] H. Wang, Y. Li, C. Li, K. Deng, Z. Wang, Y. Xu, X. Li, H. Xue, L. Wang, *J. Mater. Chem. A* **2019**, 7, 801.

[207] R. Lan, J. T. Irvine, S. Tao, *Sci. Rep.* **2013**, 3, 1145.

[208] J. Wang, L. Yu, L. Hu, G. Chen, H. Xin, X. Feng, *Nat. Commun.* **2018**, 9, 1795.

[209] Q. Shi, S. Hwang, H. Yang, F. Ismail, D. Su, D. Higgins, G. Wu, *Mater. Today* **2020**, doi:10.1016/j.mattod.2020.02.019.

[210] T. Wang, Q. Zhao, Y. Fu, C. Lei, B. Yang, Z. Li, L. Lei, G. Wu, Y. Hou, *Small Methods* **2019**, 3, 1900210.

[211] S. Luo, X. Li, W. Gao, H. Zhang, M. Luo, *Sustainable Energy Fuels* **2020**, 4, 164.

[212] S. Chen, S. Perathoner, C. Ampelli, C. Mebrahtu, D. Su, G. Centi, *ACS Sustainable Chem. Eng.* **2017**, 5, 7393.

[213] G. Zhang, Q. Ji, K. Zhang, Y. Chen, Z. Li, H. Liu, J. Li, J. Qu, *Nano Energy* **2019**, 59, 10.

[214] C. Duan, R. J. Kee, H. Zhu, C. Karakaya, Y. Chen, S. Ricote, A. Jarry, E. J. Crumlin, D. Hook, R. Braun, N. P. Sullivan, R. O'Hayre, *Nature* **2018**, 557, 217.

[215] C. Duan, J. Tong, M. Shang, S. Nikodemski, M. Sanders, S. Ricote, A. Almansoori, R. O'Hayre, *Science* **2015**, 349, 1321.

[216] N. V. Rees, R. G. Compton, *Energy Environ. Sci.* **2011**, 4, 1255.

[217] G. G. M. Fournier, I. W. Cumming, K. Hellgardt, *J. Power Sources* **2006**, 162, 198.

[218] K. Siddharth, Y. Chan, L. Wang, M. Shao, *Curr. Opin. Electrochem.* **2018**, 9, 151.

[219] S. Mukherjee, S. V. Devaguptapu, A. Sviripa, C. R. F. Lund, G. Wu, *Appl. Catal. B Environ.* **2018**, 226, 162.

[220] S. E. L. Cairns; E. J., Tevebaugh; A. D., *Nature* **1968**, 217, 780.

[221] O. Siddiqui, I. Dincer, *Therm. Sci. Eng. Prog.* **2018**, 5, 568.

[222] Y. Zhao, B. P. Setzler, J. Wang, J. Nash, T. Wang, B. Xu, Y. Yan, *Joule* **2019**, 3, 1.

[223] J. C. Ganley, *J. Power Sources* **2008**, 178, 44.

[224] *https://arpa-e.energy.gov/?q=slick-sheet-project/more-information-uds-project-coming-soon-0* **2017**.

[225] H. Gerischer, A. Mauerer, *J. Electroanal. Chem.* **1970**, 25, 421.

[226] H. G. Oswin, M. Salomon, *Can. J. Chem.* **1963**, 41, 1686.

[227] J. A. Herron, P. Ferrin, M. Mavrikakis, *J. Phys. Chem. C* **2015**, 119, 14692.

[228] A. Estejab, G. G. Botte, *Comput. Theor. Chem.* **2016**, 1091, 31.

[229] D. A. Daramola, G. G. Botte, *Comput. Theor. Chem.* **2012**, 989, 7.

[230] D. A. Daramola, G. G. Botte, *J. Colloid Interface Sci.* **2013**, 402, 204.

[231] N. Sacré, M. Duca, S. Garbarino, R. Imbeault, A. Wang, A. Hadj Youssef, J. Galipaud, G.

Hufnagel, A. Ruediger, L. Roué, D. Guay, *ACS Catal.* **2018**, 8, 2508.

[232] Y. Katayama, T. Okanishi, H. Muroyama, T. Matsui, K. Eguchi, *ACS Catal.* **2016**, 6, 2026.

[233] G. Novell-Leruth, A. Valca´rcel, A. Clotet, J. M. Ricart, J. Pe´rez-Ramı´rez, *J. Phys. Chem. B* **2005**, 109, 18061.

[234] G. Novell-Leruth, A. Valca´rcel, J. Pe´rez-Ramı´rez, J. M. Ricart, *J. Phys. Chem. C* **2007**, 111, 860.

[235] A. Estejab, G. G. Botte, *Mol. Catal.* **2018**, 445, 279.

[236] H. S. Pillai, H. Xin, *Ind. Eng. Chem. Res.* **2019**, 58, 10819.

[237] C. Zhong, J. Liu, Z. Ni, Y. Deng, B. Chen, W. Hu, *Sci. China Mater.* **2014**, 57, 13.

[238] C. Zhong, W. B. Hu, Y. F. Cheng, *J. Mater. Chem. A* **2013**, 1, 3216.

[239] M. H. M. T. Assumpção, R. M. Piasentin, P. Hammer, R. F. B. De Souza, G. S. Buzzo, M. C. Santos, E. V. Spinacé, A. O. Neto, J. C. M. Silva, *Appl. Catal. B Environ.* **2015**, 174-175, 136.

[240] A. Allagui, S. Sarfraz, E. A. Baranova, *Electrochim. Acta* **2013**, 110, 253.

[241] W. Xu, D. Du, R. Lan, J. Humphreys, D. N. Miller, M. Walker, Z. Wu, J. T. S. Irvine, S. Tao, *Appl. Catal. B Environ.* **2018**, 237, 1101.

[242] J. Jeong, C. Kim, J. Yoon, *Water Res.* **2009**, 43, 895.

[243] M. Sun, J. Liu, C. Song, Y. Ogata, H. Rao, X. Zhao, H. Xu, Y. Chen, *ACS Appl. Mater. Interfaces* **2019**, 11, 23102.

[244] A. Borcuch, M. Rutkowska, A. Marzec, A. Kowalczyk, M. Michalik, J. M. Moreno, U.

Díaz, L. Chmielarz, *Catal. Today* **2019**, DOI: 10.1016/j.cattod.2019.08.054.

[245] Y. Li, X. Li, H. Pillai, J. Lattimer, N. Mohd Adli, S. G. Karakalos, M. Chen, L. Guo, H. Xu, J. Yang, D. Su, H. Xin, G. Wu, *ACS Catal.* **2020**, 10, 3945.

[246] J. Liu, B. Chen, Y. Kou, Z. Liu, X. Chen, Y. Li, Y. Deng, X. Han, W. Hu, C. Zhong, *J. Mater. Chem. A* **2016**, 4, 11060.

[247] S. Morita, E. Kudo, R. Shirasaka, M. Yonekawa, K. Nagai, H. Ota, M. N.-Gamo, H. Shiroishi, *J. Electroanal. Chem.* **2016**, 762, 29.

[248] Y. Zhou, G. Zhang, M. Yu, J. Xu, S. Qiao, X. Cheng, F. Yang, *ChemistrySelect* **2018**, 3, 3433.

[249] J. Jiang, *Electrochem. Commun.* **2017**, 75, 52.

[250] R. H. Manso, L. Song, Z. Liang, J. X. Wang, J. Chen, *ECS Trans.* **2018**, 85, 177.

[251] F. J. Vidal-Iglesias, N. Garcia-Araez, V. Montiel, J. M. Feliu, A. Aldaz, *Electrochem. Commun.* **2003**, 5, 22.

[252] S. Johnston, B. H. R. Suryanto, D. R. MacFarlane, *Electrochim. Acta* **2019**, 297, 778.

[253] C. Zhong, W. B. Hu, Y. F. Cheng, *J. Power Sources* **2011**, 196, 8064.

[254] J. Liu, C. Zhong, Y. Yang, Y. T. Wu, A. K. Jiang, Y. D. Deng, Z. Zhang, W. B. Hu, *Int. J. Hydrogen Energy* **2012**, 37, 8981.

[255] J. Liu, W. Hu, C. Zhong, Y. F. Cheng, *J. Power Sources* **2013**, 223, 165.

[256] Y. Katayama, T. Okanishi, H. Muroyama, T. Matsui, K. Eguchi, *J. Phys. Chem. C* **2015**, 119, 9134.

[257] Q. Tan, C. Shu, J. Abbott, Q. Zhao, L. Liu, T. Qu, Y. Chen, H. Zhu, Y. Liu, G. Wu, *ACS Catal.* **2019**, 9, 6362.

[258] Y. Kang, W. Wang, J. Li, Q. Li, S. Liu, Z. Lei, *J. Electrochem. Soc.* **2017**, 164, F958.

[259] N. M. Markovic, P. N. Ross Jr., *Surf. Sci. Rep.* **2002**, 45, 117.

[260] T. Toda, H. Igarashi, H. Uchida, M. Watanabe, *J. Electroanal. Chem.* **1999**, 146, 3750.

[261] F. J. Vidal-Iglesias, J. Solla-Gullón, V. Montiel, J. M. Feliu, A. Aldaz, *J. Power Sources* **2007**, 171, 448.

[262] T. L. Lomocso, E. A. Baranova, *Electrochim. Acta* **2011**, 56, 8551.

[263] K. Yao, Y. F. Cheng, *J. Power Sources* **2007**, 173, 96.

[264] K. Endo, Y. Katayama, T. Miura, *Electrochim. Acta* **2004**, 49, 1635.

[265] J. C. M. Silva, S. G. da Silva, R. F. B. De Souza, G. S. Buzzo, E. V. Spinacé, A. O. Neto, M. H. M. T. Assumpção, *Appl. Catal. A Gen.* **2015**, 490, 133.

[266] C.-M. Hung, *Int. J. Hydrogen Energy* **2012**, 37, 13815.

[267] R. H. Manso, L. Song, Z. Liang, J. X. Wang, J. Chen, *ECS Trans.* **2018**, 85, 177.

[268] S. Le Vot, L. Roué, D. Bélanger, *J. Power Sources* **2013**, 223, 221.

[269] K. Vinodgopal, Y. He, M. Ashokkumar, F. Grieser, *J. Phys. Chem. B* **2006**, 110, 3849.

[270] Y. T. Chan, K. Siddharth, M. Shao, *Nano Res.* **2020**, DOI: 10.1007/s12274-020-2712-1.

[271] J. A. Herron, P. Ferrin, M. Mavrikakis, *J. Phys. Chem. C* **2015**, 119, 14692.

[272] D. A. Finkelstein, E. Bertin, S. Garbarino, D. Guay, *J. Phys. Chem. C* **2015**, 119, 9860.

[273] S. Suzuki, H. Muroyama, T. Matsui, K. Eguchi, *J. Power Sources* **2012**, 208, 257.

[274] H. M. J. Yang, T. Matsui, K. Eguchi, *J. Power Sources* **2014**, 245, 277.

[275] K. R. Lee, D. Song, S. B. Park, J.-i. Han, *RSC Adv.* **2014**, 4.

[276] M. H. M. T. Assumpção, S. G. da Silva, R. F. B. De Souza, G. S. Buzzo, E. V. Spinacé, M. C. Santos, A. O. Neto, J. C. M. Silva, *J. Power Sources* **2014**, 268, 129.

[277] O. Siddiqui, I. Dincer, *Energy* **2019**, 169, 914.

[278] Y. Yang, X. Su, L. Zhang, P. Kerns, L. Achola, V. Hayes, R. Quardokus, S. L. Suib, J. He, *ChemCatChem* **2019**, 11, 1689.

The review aims to highlight important but challenging electrocatalysis associated with sustainable water (oxygen evolution and reduction reactions) and nitrogen (nitrogen reduction and ammonia oxidation reactions) cycles. The efficient energy conversion processes rely on the development of the corresponding water electrolyzers, fuel cells, and ammonia electrosynthesis, and direct ammonia fuel cells. Herein, advanced catalysts, along with optimal electrolytes and electrode fabrication, are crucial for these clean energy technologies with significantly improved performance and durability.

Keywords: electrocatalysis, energy conversion, clean energy, oxygen reactions, nitrogen reactions

Yi Li[+], Huanhuan Wang[+], Cameron Priest, Siwei Li, Ping Xu, and Gang Wu**

Advanced Electrocatalysis for Energy and Environmental Sustainability via Water and Nitrogen Reactions

TOC figure

Yi Li is a visiting Ph.D. student at the University at Buffalo, the State University of New York (USA). He received his B.Sc. degree (2013) at Changzhou University and his M.Sc. degree (2016) at Jiangsu University. His current research interests are nanomaterials synthesis and electrocatalysis for electrochemical energy storage and conversion.

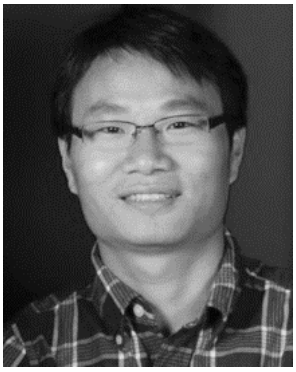

Dr. Ping Xu is a professor in the School of Chemistry and Chemical Engineering at the Harbin Institute of Technology (HIT). He received his BS degree in Applied Chemistry (2003) and Ph.D. degree in Chemical Engineering and Technology (2010) from HIT. He spent one year (2008–2009) as a visiting student and one and a half years (2012–2013) as a Director's Postdoctoral Fellow at Los Alamos National Laboratory (LANL). He started as an Assistant Professor at HIT in 2010 and was promoted to Associate professor in 2013 and Full professor in 2014. His current research interests include the design and synthesis of nanostructured materials and hybrid materials for applications in surface-enhanced Raman spectroscopy and surface plasmon assisted catalysis and advanced energy devices.

Dr. Gang Wu is a professor in the Department of Chemical and Biological Engineering at the University at Buffalo, The State University of New York (SUNY-Buffalo). He completed his Ph.D. studies at the Harbin Institute of Technology in 2004, followed by extensive postdoctoral training at Tsinghua University (2004-2006), the University of South Carolina (2006-2008), and Los Alamos National Laboratory (LANL) (2008-2010). Then, Dr. Wu became a staff scientist at LANL. He joined SUNY-Buffalo as a tenure-track assistant professor in 2014 and was early promoted to a tenured Associate professor in 2018 and a Full professor in 2020. His research focuses on functional materials and catalysts for electrochemical energy technologies. Dr. Wu has published more than 220 papers and received total citations >21,000 (h-index: 73). He was a Highly Cited Researcher selected by Thomson Reuters, Clarivate Analytics in 2018 and 2019.